

Doctoral Dissertation  
博士論文

Theory of surface states and transport  
phenomena in topological magnon systems  
(トポロジカルマグノン系における表面状  
態と輸送現象の理論)

A Dissertation Submitted for the Degree of Doctor of Philosophy

December 2021

令和3年12月博士（理学）申請

Department of Physics, Graduate School of Science,

The University of Tokyo

東京大学大学院理学系研究科物理学専攻

Hiroki Kondo

近藤 寛記



# ABSTRACT

In this thesis, we investigate the surface states appearing due to the nontrivial topology of the magnon wave functions and the transport phenomena related to the Berry curvature of magnons. In recent years, there has been much interest in the properties arising from the nontrivial topology of the band structure of particles in materials. Although many important concepts are proposed for electrons, topological properties have also been investigated for bosonic quasiparticles such as magnons, photons, phonons, and triplons. In particular, magnons carry spins over long distances in magnetic materials, and their topological properties are of interest from the viewpoint of realizing new transport phenomena in materials, since their fundamental properties themselves are different from those of electrons. So far, models of magnetic materials with chiral and helical edge states of magnons, which correspond to quantum Hall insulators and quantum spin Hall insulators in two dimensions, respectively, have been investigated. Among the topological materials, the realization of magnonic counterparts of three-dimensional topological insulators with Dirac surface states is expected to give rise to a variety of novel properties, as is the case of electrons. However, the Dirac surface states in three-dimensional topological insulators require the Kramers degeneracy due to time-reversal symmetry for fermions. On the other hand, since magnons are bosons, usual time-reversal symmetry does not give rise to the Kramers degeneracy. Therefore, a magnonic counterpart of three-dimensional topological insulators has not yet been constructed. Magnons flowing in the bulk of magnets also give rise to nontrivial transport phenomena associated with their Berry curvature. Through the spin Nernst effect of magnons, a pure spin current flows in the direction perpendicular to the temperature gradient. However, in the range of linear response to the temperature gradient, such spin currents require specific interactions such as the Dzyaloshinskii-Moriya interaction. The topological properties of magnons as a nonlinear response have not been explored yet.

The results of this thesis consist of the following three studies. In the first study, we propose a model of the magnon system corresponding to a three-dimensional topological insulator under an artificial setup by mimicking the fermionic time-reversal symmetry. The surface states of magnons realized are unprecedented states in magnetic systems. The corresponding topological numbers are defined, and the correspondence to the magnon Dirac surface state is discussed. However, the model is constructed as a spin system in which one lattice site has two localized spins and is difficult to be realized in materials. In addition, interactions between spins such as Heisenberg interaction, Dzyaloshinskii-Moriya interaction, and others have to be fine-tuned for the systems to have the fermionic

time-reversal symmetry.

In the second study, we construct models possessing Dirac surface states of magnons in a much more realistic setup, which are symmetric under the combination of time-reversal and half translation. This can be classified as a magnonic analog of topological crystalline insulators. We argue that the van der Waals magnet  $\text{CrI}_3$  is a candidate material to realize the proposed model. It is also found that the electric field response peculiar to the magnon system is realized due to the spin polarization of the Dirac surface states. The applied electric field gives rise to the Aharonov-Casher phase for magnons, and it causes the number of magnons on one and the other surfaces to increase and decrease, respectively. The magnon current in this process is evaluated by using linear response theory.

In the third study, we develop a theory of the nonlinear spin Nernst effect of magnons in antiferromagnets. In the previous studies, novel transport phenomena associated with the Berry curvature of magnons, such as the magnon thermal Hall and spin Nernst effect, have been studied. They result in the energy and spin current flowing in the direction perpendicular to the temperature gradient, respectively. However, these phenomena have been investigated only in the linear response regime. In these cases, the transverse magnon current requires the Dzyaloshinskii-Moriya interaction or noncollinear spin configurations. In this work, we develop a second-order response theory for the temperature gradient, and show that the magnon flow perpendicular to the temperature gradient can be described by physical quantities like the dipole moments of the Berry curvature. We consider honeycomb, square, and diamond lattice antiferromagnets that break the inversion and rotation symmetries, and show that the nonlinear spin Nernst effect can be realized without the Dzyaloshinskii-Moriya interaction in these systems.

In the surface states of magnons proposed in the first and second studies, many novel properties are expected, as is the case for electronic systems. For example, the surface states are expected to enable us to drive controlled spin currents on the surface since they exhibit spin-momentum locking, where the component of spins conveyed is locked by the direction of motion. In addition, the induction of the magnon current by an electric field, which is discussed in the second study, provides a novel way to manipulate magnons. Since the nonlinear spin Nernst effect of magnons, which is proposed in the third study, can occur in many magnetic materials even without the Dzyaloshinskii-Moriya interaction, it leads to the generation of strain-tunable spin current in magnets without heavy atoms.

# ACKNOWLEDGMENTS

I wish to express my greatest gratitude to my supervisor Prof. Hosho Katsura for his kind support, advice, and fruitful discussions all over my Ph.D. program. His helpful comments for the studies encouraged me a lot. From his advice, I learned many things about not only physics but also how I should behave as a scientist. I would also like to thank Dr. Yutaka Akagi extremely for his helpful collaborations, many interesting discussions, and for improving my skill in academic writing. In spite of his busy schedule, he spent much of his time discussing and correcting our papers. He helped me not only with my research but also with my personal matters such as career development. Without their painstaking guidance, the results of this thesis could not be fruitful. I would like to express my gratitude to the members of Katsura group and floormates for the cheerful encouragements and joyful conversations. Talking with them enabled me to enjoy my graduate student life. I acknowledge the referees of this thesis, Prof. Akira Shimizu, Prof. Shuichi Murakami, Prof. Takashi Oka, Prof. Eiji Saitoh, and Prof. Akito Sakai. I also thank the secretary of Katsura group, Ms. Yoshie Sayama, for her support. Finally, I express my gratitude to my family for caring about and supporting me in my daily life. My work is greatly supported by the financial support from the Japan Society for the Promotion of Science (JSPS) through the Program for Leading Graduate Schools (ALPS) and KAKENHI Grant No. JP20J12861.



# List of Publications

Published papers on which this thesis is based are as follows:

1. H. Kondo, Y. Akagi, and H. Katsura,  *$\mathbb{Z}_2$  topological invariant for magnon spin Hall systems*, Physical Review B **99**, 041110(R) (2019).
2. H. Kondo, Y. Akagi, and H. Katsura, *Three-dimensional topological magnon systems*, Physical Review B **100**, 144401 (2019).
3. H. Kondo, Y. Akagi, and H. Katsura, *Non-Hermiticity and topological invariants of magnon Bogoliubov-de Gennes systems*, Progress of Theoretical and Experimental Physics **2020**, 12A104 (2020).
4. H. Kondo and Y. Akagi, *Dirac surface states in magnonic analogs of topological crystalline insulators*, Physical Review Letters **127**, 177201 (2021).

This thesis also includes the results of the following preprint:

1. H. Kondo and Y. Akagi, *Nonlinear magnon spin Nernst effect in antiferromagnets and strain-tunable pure spin current*, arXiv:2109.09464 (Accepted in Physical Review Research).



# Contents

<b>1</b>	<b>Introduction</b>	<b>1</b>
1.1	Review of the topological properties of electrons . . . . .	1
1.1.1	Electronic properties related to nontrivial band topology . . . . .	1
1.1.2	Quantum Hall effect and Chern number . . . . .	2
1.1.3	Quantum spin Hall insulators . . . . .	3
1.1.4	Three-dimensional topological insulators . . . . .	7
1.1.5	Topological crystalline insulators . . . . .	11
1.1.6	Nonlinear Hall effect . . . . .	14
1.2	Brief introduction to studies on magnons related to our work . . . . .	16
1.3	Purpose and organization of this thesis . . . . .	17
<b>2</b>	<b>Topological properties of magnons: formalism and applications</b>	<b>19</b>
2.1	Basic properties of magnons . . . . .	19
2.2	Diagonalization of bosonic Bogoliubov-de Gennes Hamiltonians . . . . .	21
2.3	Dzyaloshinskii-Moriya interaction and the thermal Hall effect of magnons	23
2.4	Transverse current of magnons as a nonlinear response . . . . .	26
2.5	Spin Nernst effect of magnons . . . . .	27
2.6	Magnonic analogs of quantum spin Hall insulators . . . . .	30
<b>3</b>	<b>Three-dimensional topological magnon systems</b>	<b>37</b>
3.1	Model . . . . .	37
3.2	Topological invariants . . . . .	38
3.3	Simplified expressions for the topological invariants of the diamond lattice system . . . . .	39
3.4	Phase diagram and band structure . . . . .	42
<b>4</b>	<b>Dirac surface states in magnonic analogs of topological crystalline insulators</b>	<b>45</b>
4.1	Model . . . . .	45
4.2	Energy current induced by a homogeneous electric field . . . . .	48
4.3	Realization of Dirac surface states of magnons in $\text{CrI}_3$ . . . . .	51
4.4	Phase diagrams . . . . .	53

<b>5</b>	<b>Nonlinear spin Nernst effect of magnons</b>	<b>55</b>
5.1	Expression of the nonlinear spin Nernst current of magnons . . . . .	56
5.2	Honeycomb lattice antiferromagnet with strain . . . . .	59
5.3	Order estimation of the nonlinear spin Nernst effect . . . . .	62
5.4	Nonlinear spin Nernst effect of magnons in various antiferromagnets . . .	64
<b>6</b>	<b>Summary and future prospects</b>	<b>69</b>
	<b>Appendix</b>	<b>71</b>
	Appendix A : Proof of the statements in Sec. 2.2 . . . . .	71
	Appendix B : Derivation of magnon thermal Hall current . . . . .	73
	Appendix C : Kramers pairs of bosons described by Bogoliubov-de Gennes Hamiltonians . . . . .	74
	Appendix D : Details of the interactions in the Hamiltonian (3.1) . . . . .	75
	Appendix E : The analytical expressions of energy eigenvalues . . . . .	78
	Appendix F : Explicit expression of Hamiltonian matrix in Eq. (4.2) . . . . .	80
	Appendix G : The derivation of the effective Hamiltonian for the surface . . .	81
	Appendix H : Expression of energy current . . . . .	82
	Appendix I : Expression of perturbation term due to an electric field . . . . .	83
	Appendix J : Magnon Hamiltonian of CrI <sub>3</sub> . . . . .	85

# Chapter 1

## Introduction

In this thesis, we are particularly interested in phenomena in magnetic materials, which are brought about by the topological properties of magnons. The primary concepts of topological properties are proposed first in electronic systems, such as quantum Hall insulators and topological insulators. Before considering magnons, we discuss studies on topological properties in electronic systems in Sec. 1.1. After that, in Sec. 1.2, we briefly introduce the studies of magnons which are particularly related to our work. In Sec. 1.3, the purpose and the organization of this thesis are given.

### 1.1 Review of the topological properties of electrons

In this part, we review representative studies on the topological properties, focusing on electronic systems. We give a brief introduction to topological properties of electrons in Sec. 1.1.1. We discuss quantum Hall insulators, quantum spin Hall insulators, three-dimensional (3D) topological insulators, and topological crystalline insulators in turn in Sec. 1.1.2, Sec. 1.1.3, Sec. 1.1.4, and Sec. 1.1.5, respectively. In Sec. 1.1.6, we show the studies on the Hall effect as a nonlinear response.

#### 1.1.1 Electronic properties related to nontrivial band topology

Researchers recognized that the nontrivial topology of the electron wave functions in materials could be the origin of novel physical properties at the time when the quantum Hall effect was formulated [1]. The quantum Hall effect is a phenomenon in which the transverse conductivity is quantized in a magnetic field. The transverse conductivity is expressed by using the integral of the Berry curvature describing the topology of the wave function, which is an integer called Chern number. The Chern number corresponds to the number of edge states. These electron edge states contribute to the electric current propagating in the direction perpendicular to the electric field [1–8]. The proposal of quantum spin Hall insulators [9–15], which have helical edge states protected by time-reversal symmetry, first suggested the possibilities of topological properties that can emerge depending on the symmetries of the system.

An important study that follows this is the extension of quantum spin Hall insulators to three-dimensions [16]. Such 3D topological insulators exhibit a wide variety of nontrivial properties [16–26]. On the surface of 3D topological insulators, electrons with single Dirac cone appear, which is protected by time-reversal symmetry. This surface state exhibits spin-momentum locking, in which spin orientation and direction of motion are locked to each other [17, 18, 27]. In addition, 3D topological insulators are shown to exhibit nontrivial magnetoelectric effects, which are called topological magnetoelectric effects [28–31].

In recent years, one of the areas that has been developing is the topological crystalline insulators, a class of materials with surface states protected by various crystalline symmetries [32–38]. Transport properties associated with the Berry curvature are also being revisited from the perspective of nonlinear response. It has been shown that the Hall current proportional to the second-order of the electric field is described by the Berry curvature dipole, which is the dipole moment of the Berry curvature [39–53], and has been observed in layered  $\text{WTe}_2$  [54, 55]. The remarkable feature of the nonlinear Hall effect is that it is realized even in materials with time-reversal symmetry.

### 1.1.2 Quantum Hall effect and Chern number

In a strong magnetic field, electrons confined in two-dimensional (2D) materials are known to exhibit a quantized transverse conductivity. This is called the quantum Hall effect [1–8] and is directly related to the topology of the electron wave function. Thouless-Kohmoto-Nightingale-den Nijs (TKNN) formula [1], which describes such a Hall conductivity, is written as follows:

$$\sigma_{xy} = -\frac{e^2}{2\pi h} \sum_{n, (E_n \leq E_F)} \int_{\text{BZ}} dk_x dk_y \Omega_n(k_x, k_y), \quad (1.1)$$

where  $\Omega_n(k_x, k_y)$  is the Berry curvature of electrons. Here,  $e$  and  $h$  are the elementary charge and the Planck constant, respectively. By using the eigenstates  $|\psi_n(k_x, k_y)\rangle$  of the Hamiltonian with the band index  $n$ , it is defined as follows:

$$\Omega_n(k_x, k_y) = -2\text{Im}[\langle \partial_{k_x} \psi_n(k_x, k_y) | \partial_{k_y} \psi_n(k_x, k_y) \rangle]. \quad (1.2)$$

Here,  $E_n$  and  $E_F$  are the eigenenergy of  $|\psi_n(k_x, k_y)\rangle$  and the Fermi energy, respectively. In gapped systems, the following integral of the Berry curvature over the Brillouin zone (BZ) is quantized:

$$\text{Ch} = \frac{1}{2\pi} \sum_{n, (E_n \leq E_F)} \int_{\text{BZ}} dk_x dk_y \Omega_n(k_x, k_y), \quad (1.3)$$

The integer Ch is called Chern number and corresponds to the number of edge states which appear in the quantum Hall insulators with open boundary conditions. Figure 1.1 is the band structure of the Haldane model [8], known as an example of In the bulk band gap, we can see the edge state resulting from the nontrivial topology of electron wave

functions. The TKNN formula (1.1) implies that one edge states contribute to the Hall conductance by  $e^2/h$ .

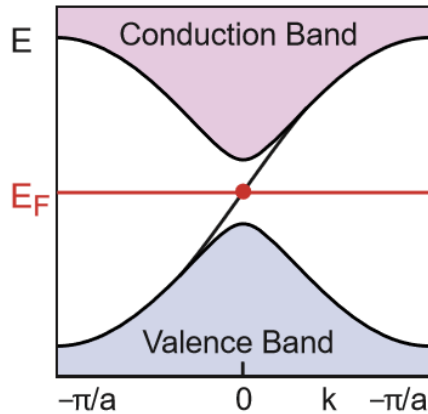


Fig. 1.1: The band structure of the Haldane model [8], with open boundary conditions. Between the conduction and valence bands, there is a chiral edge state, which contributes to the quantum Hall conductivity. This figure is taken from Ref. [17].

The phases of matters related to the band topology of electrons, such as quantum Hall insulators, is called topological phases [56–73]. The invariants that characterize them, such as the Chern number, are called the topological invariants [74–83]. So far, a huge variety of topological phases have been investigated, and the topological indices may take various expressions depending on the symmetries of the systems.

### 1.1.3 Quantum spin Hall insulators

In the case of quantum Hall insulators, what is important for making the electron band structure to be topologically-nontrivial is to break the time-reversal symmetry by, e.g., applying a magnetic field. For some time after the discovery of the quantum Hall effect, people have not particularly associated the topological properties of electrons with time reversal or any other symmetry. In fact, however, the topological phases exhibited by electrons in materials can be extremely diverse depending on the symmetries of the materials.

What made people aware of this possibility was the theoretical proposal of quantum spin Hall insulators with helical edge states protected by time-reversal symmetry [9, 10]. Pairs of electronic states, which possess opposite spins and are associated with each other by the time-reversal operator, appear at the edge of these materials. Since these electronic states flow in opposite directions to each other, the transverse current is not an electric current but a spin current. The first model for the quantum spin Hall insulators was constructed by combining the two copies of the Haldane model [8], to restore time-reversal symmetry. It is called the Kane-Mele model, which is described as a tight-binding

model on the honeycomb lattice. The Hamiltonian is written as follows:

$$H = \sum_{\langle i,j \rangle, \alpha} t c_{i\alpha}^\dagger c_{j\alpha} + \sum_{\langle\langle i,j \rangle\rangle, \alpha, \beta} it_2 c_{i\alpha}^\dagger [\mathbf{s} \cdot (\mathbf{d}_{ij}^1 \times \mathbf{d}_{ij}^2)]_{\alpha\beta} c_{j\beta}, \quad (1.4)$$

where the indices  $\alpha, \beta$  ( $=\uparrow, \downarrow$ ) correspond to the directions of spins of electrons. Here,  $c_{i\uparrow(\downarrow)}$  and  $c_{i\uparrow(\downarrow)}^\dagger$  are the annihilation and creation operators of electrons with up (down) spins at site  $i$ , respectively. The first and second terms are the nearest-neighbor hopping and the second nearest-neighbor spin-orbit interaction. The second nearest-neighbor sites  $i$  and  $j$  have one common nearest-neighbor sites, which we denote as  $k$ . The vectors pointing from  $k$  to  $i$  and  $j$  are written as  $\mathbf{d}_{ij}^1$  and  $\mathbf{d}_{ij}^2$ , respectively [see Fig. 1.2(a)]. The spin operator is given by  $\mathbf{s}$ . By using Pauli matrices  $\boldsymbol{\sigma} = (\sigma_x, \sigma_y, \sigma_z)$ , it is defined as  $\mathbf{s} = (\hbar/2)\boldsymbol{\sigma}$ .

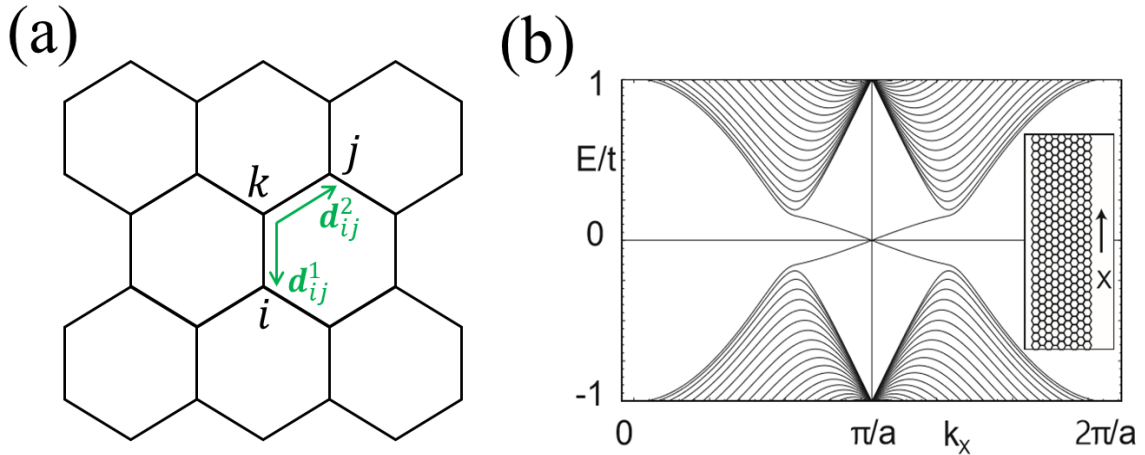


Fig. 1.2: (a) Honeycomb lattice and the vectors  $\mathbf{d}_{ij}^1$  and  $\mathbf{d}_{ij}^2$  which appear in Eq. (1.4). (b) Band structure of the Kane-Mele model [9]. The gapless helical edge states cross at  $k_x = \pi/a$ . Figure (b) is taken from Ref. [9].

The band structure of this model is shown in Fig. 1.2(b). A gapless helical edge state can be seen around  $k_x = \pi/a$ . This can be interpreted as just a pair of chiral edge states in a quantum Hall insulator with electronic states having opposite spins. In particular, in the case that the system conserves spin, electron states with opposite spins flowing in opposite directions lead to a unique transport phenomenon known as the pure spin current, which does not accompany an electric current. As shown in Fig. 1.3, when electrons flow in opposite directions, the electric currents carried by these electron states cancel out. On the other hand, since the spins of the pair of electrons in helical edge states are opposite, spin currents are conveyed in the same direction. Therefore, it remains uncanceled. Such a pure spin current is expected to have possible applications in spintronics [84], due to the ability to convey the information without Joule heating.

The quantum spin Hall insulator was first realized [11, 12] in HgTe/CdTe quantum well structures, in which HgTe is sandwiched between the layers of CdTe. The band inversion occurs at the thickness of the quantum well  $d = d_c = 6.3$ . The band structure of HgTe/CdTe quantum well structures is topologically nontrivial (trivial) when  $d > d_c$  ( $d < d_c$ ).

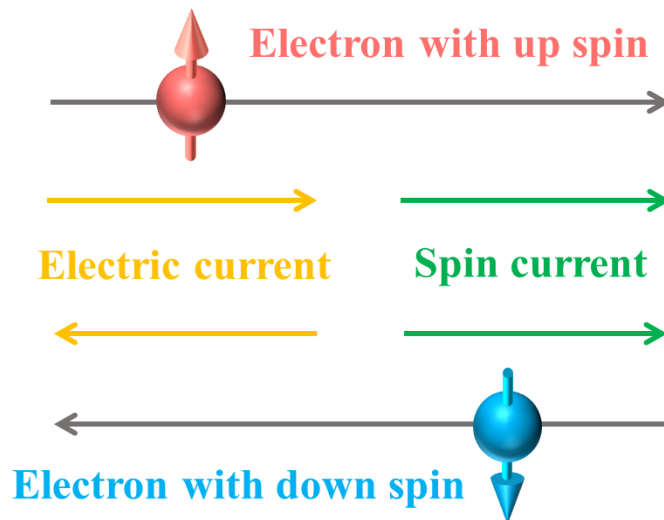


Fig. 1.3: Counter-propagating electron states which are realized in the quantum spin Hall insulators. Electrons with up spin moving to the right convey the electric and spin current to the right. On the other hand, electrons with down spin moving to the left convey the electric and spin current to the left and the right, respectively. As a result, the electric current cancels out, while the spin current does not.

The existence of the gapless helical edge state at  $k_x = \pi/a$  in Fig. 1.2 is closely related with the Kramers degeneracy in time-reversal-invariant systems. According to Kramers theorem, when fermionic systems are symmetric under time-reversal, each energy level is at least doubly degenerate at time-reversal-invariant momenta (TRIM) in BZ. Here, TRIM  $\mathbf{\Lambda}$  are defined as the momenta such that  $\mathbf{\Lambda}$  and  $-\mathbf{\Lambda}$  correspond to the same point in the Brillouin zone. Due to this, the gapless point of the band structures of the helical edge state, which appears as a Kramers pair, is protected in the presence of the time-reversal symmetry. This indicates the robustness of the helical edge states.

Topological phases of 2D topological insulators are characterized by  $\mathbb{Z}_2$  indices. Among the various expressions of  $\mathbb{Z}_2$  indices [74–83], we here introduce the one which is given by integrating the Berry connection and curvature in the effective Brillouin zone which

is one-half of BZ [13]. It is defined as follows:

$$D_n := \frac{1}{2\pi} \left[ \oint_{\partial\text{EBZ}} d\mathbf{k} \cdot \mathbf{A}_n(\mathbf{k}) - \int_{\text{EBZ}} d^2k \Omega_n^z(\mathbf{k}) \right] \text{ mod } 2, \quad (1.5)$$

where EBZ denotes the effective Brillouin, which is shown in Fig. 1.4. Here we denote the index for the bands as  $n$ . Due to the time-reversal symmetry, the  $n$ th band consists of two eigenstates  $|\psi_{n,1}(\mathbf{k})\rangle$  and  $|\psi_{n,2}(\mathbf{k})\rangle$ , which are related by the time-reversal operator  $\Theta$  as follows:

$$|\psi_{n,2}(\mathbf{k})\rangle = -\Theta |\psi_{n,1}(-\mathbf{k})\rangle. \quad (1.6)$$

When we write the corresponding Berry connection and curvature of  $|\psi_{n,l}(\mathbf{k})\rangle$  ( $l = 1, 2$ ) as

$$\mathbf{A}_{n,l}(\mathbf{k}) = i \langle \psi_{n,l}(\mathbf{k}) | \nabla_{\mathbf{k}} \psi_{n,l}(\mathbf{k}) \rangle, \quad (1.7)$$

$$\Omega_{n,l}^z(\mathbf{k}) = (\nabla_{\mathbf{k}} \times \mathbf{A}_{n,l}(\mathbf{k}))_z, \quad (1.8)$$

the total Berry connection and curvature in Eq. (1.5) are defined as the summations over  $l = 1, 2$ , i.e.,

$$\mathbf{A}_n(\mathbf{k}) = \sum_{l=1,2} \mathbf{A}_{n,l}(\mathbf{k}), \quad (1.9)$$

$$\Omega_n^z(\mathbf{k}) = \sum_{l=1,2} \Omega_{n,l}^z(\mathbf{k}). \quad (1.10)$$

Here, we note that due to the relation (1.6), the electron wave functions with wave vectors  $\mathbf{k}$  and  $-\mathbf{k}$  are not independent, as depicted in Fig. 1.4. Thus, the total Berry connection (1.9) and curvature (1.10) describe the topology of the wave functions with both the wave vector  $\mathbf{k}$  and  $-\mathbf{k}$ . Therefore, the topologically-nontrivial structure is accounted for without overlap by integrating them only in the EBZ part.

The number of gapless helical edge states which cross the Fermi surface corresponds to the topological index summed over the bands under the Fermi surface, i.e.,

$$D = \sum_{n, (E_n \leq E_F)} D_n \text{ mod } 2. \quad (1.11)$$

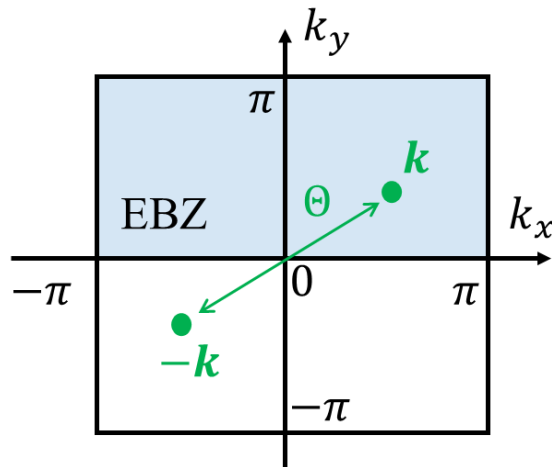


Fig. 1.4: 2D Brillouin zone of the square lattice. EBZ is shown by the blue region. Time-reversal operator  $\Theta$  relates the electron states with the wave vectors  $\mathbf{k}$  and  $-\mathbf{k}$  as in Eq. (1.6).

### 1.1.4 Three-dimensional topological insulators

After intense studies of quantum spin Hall insulators, it was theoretically suggested that materials with metallic boundary states protected by time-reversal symmetry could also exist in three dimensions [16, 20, 21]. These materials are called 3D topological insulators and exhibit electron surface states with Dirac dispersions. Unlike the case of quantum spin Hall insulators, there are two types of topologically nontrivial phases in 3D topological insulators, which are called strong and weak topological phases. The strong topological insulators are unique to 3D systems and exhibit more diverse properties than their 2D counterparts, i.e., quantum spin Hall insulators. On the other hand, the surface states in weak topological insulators are not robust against disorder. They can be regarded as a mere stacking of quantum spin Hall insulators, and whether the surface states appear or not depend on which direction the surface is cut.

The topological phases of 3D topological insulators can be classified according to the invariants defined as the winding numbers in EBZ of  $k_i = 0$  and  $\pi$  ( $i = x, y, z$ ). These are written as follows:

$$\nu_{i,0} := \sum_{n, (E_n \leq E_F)} \frac{1}{2\pi} \left[ \oint_{\partial \text{EBZ}_{i,0}} d\mathbf{k} \cdot [\mathbf{A}_n(\mathbf{k})]_{k_i=0} - \int_{\text{EBZ}_{i,0}} dk_j dk_k [\Omega_n^i(\mathbf{k})]_{k_i=0} \right] \text{ mod } 2, \quad (1.12)$$

$$\nu_{i,\pi} := \sum_{n, (E_n \leq E_F)} \frac{1}{2\pi} \left[ \oint_{\partial \text{EBZ}_{i,\pi}} d\mathbf{k} \cdot [\mathbf{A}_n(\mathbf{k})]_{k_i=\pi} - \int_{\text{EBZ}_{i,\pi}} dk_j dk_k [\Omega_n^i(\mathbf{k})]_{k_i=\pi} \right] \text{ mod } 2, \quad (1.13)$$

where  $i = x, y$  and  $z$ . The indices  $j$  and  $k$  represent two of  $x, y$  and  $z$  which are different from  $i$ . Here,  $n$ ,  $E_n$ , and  $E_F$  are the index for the bands, the energy of the  $n$ th band,

and the Fermi energy, respectively. The Berry connection in 3D systems is defined in the same way as Eq. (1.9). The Berry curvature in this case is given by

$$\mathbf{\Omega}_n(\mathbf{k}) = \nabla_{\mathbf{k}} \times \mathbf{A}_n(\mathbf{k}). \quad (1.14)$$

These are the winding numbers in the six EBZ in the 3D BZ. For example, a region denoted by  $\text{EBZ}_{x,0}$  is specified as  $k_x = 0, k_y \in [-\pi, \pi],$  and  $k_z \in [0, \pi],$  which is EBZ in the  $k_x = 0$  plane. We define the other five EBZ in similar ways (see Fig. 1.5). A loop in  $k$ -space  $\partial\text{EBZ}_{i,0(\pi)}$  is a boundary of  $\text{EBZ}_{i,0(\pi)}$ .

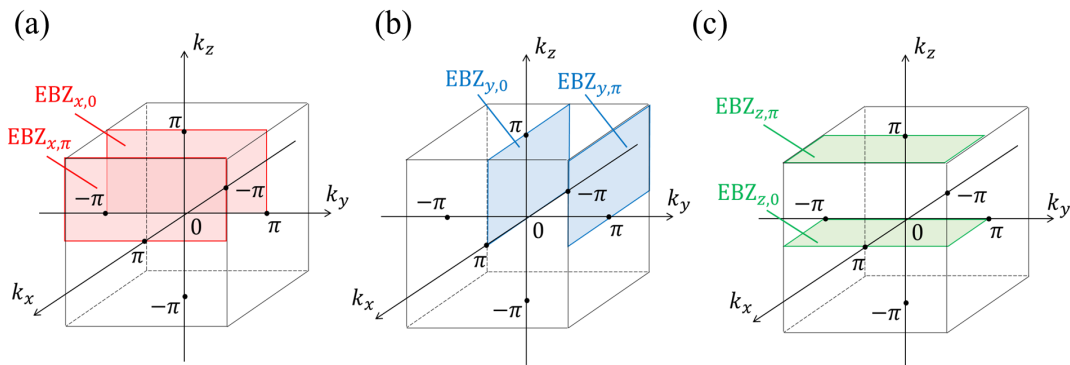


Fig. 1.5: Six EBZ in the 3D BZ of the cubic lattice. Those in (a) the  $k_x = 0$  ( $\pi$ ) plane, (b) the  $k_y = 0$  ( $\pi$ ) plane, and (c) the  $k_z = 0$  ( $\pi$ ) plane are written as  $\text{EBZ}_{x,0(\pi)}, \text{EBZ}_{y,0(\pi)},$  and  $\text{EBZ}_{z,0(\pi)},$  respectively.

These six topological invariants are not independent since they satisfy the following relation:

$$\nu_{x,0} + \nu_{x,\pi} = \nu_{y,0} + \nu_{y,\pi} = \nu_{z,0} + \nu_{z,\pi} \quad \text{mod } 2. \quad (1.15)$$

Thus, the topological phases of 3D topological insulators are characterized by a set of independent topological invariants  $(\nu_0; \nu_x, \nu_y, \nu_z),$  where

$$\nu_0 = \nu_{x,0} + \nu_{x,\pi} \quad \text{mod } 2, \quad (1.16)$$

$$\nu_i = \nu_{i,\pi} \quad (i = x, y, z). \quad (1.17)$$

The index  $\nu_0$  determines whether the total number of Dirac cones is even or odd. In the case of  $\nu_0 = 1,$  the system has an odd number of Dirac cones crossing Fermi surface in the band structure in total. These Dirac cones on the surface are protected by the time-reversal symmetry and robust against nonmagnetic disorder. When the four invariants  $(\nu_0; \nu_x, \nu_y, \nu_z)$  are all zero, the system is topologically trivial. In the other cases, i.e.,  $\nu_0 = 0$  and at least one of  $\nu_i$  ( $i = x, y, z$ ) is nonzero, the number of Dirac cone is even. The Dirac surface states, in this case, are not robust even against time-reversal invariant disorder.

As an explicit example of 3D topological insulators, let us introduce the first model proposed by Fu, Kane, and Mele [16]. The model is described by the tight-binding Hamiltonian on the diamond lattice as follows:

$$H = \sum_{\langle i,j \rangle} (t + \delta t_p) c_i^\dagger c_j + i(8\lambda_{SO}/a^2) \sum_{\langle\langle i,j \rangle\rangle} c_i^\dagger \mathbf{s} \cdot (\mathbf{d}_{ij}^1 \times \mathbf{d}_{ij}^2) c_j, \quad (1.18)$$

where the first and second terms are the nearest-neighbor hopping and the second nearest-neighbor spin-orbit interactions. Here,  $c_i$  contains two components of annihilation operators of electrons with up and down spins. The hopping amplitude is different between the four nearest-neighbor bonds on the diamond lattice. The difference is described by  $\delta t_p$  ( $p = 1, \dots, 4$ ). The vectors  $\mathbf{d}_{ij}^1$  and  $\mathbf{d}_{ij}^2$  are defined in a similar way as the Kane-Mele model (1.4). When we write one common nearest-neighbor sites between the second nearest-neighbor sites  $i$  and  $j$  as  $k$ ,  $\mathbf{d}_{ij}^1$  and  $\mathbf{d}_{ij}^2$  are defined as the vectors pointing from  $k$  to  $i$  and  $j$ .

Figure 1.6 shows the band structure of the Fu-Kane-Mele model (1.18). We can see the correspondence between the topological indices and the number of Dirac cones described above. When the strong index is  $\nu_0 = 0$ , as in the upper left and upper right panels, the number of surface states is even. In this case, whether or not a surface state appears depends on how the surface is cut. Weak topological insulators can be regarded as stacks of two-dimensional spin Hall insulators, and the weak index  $\nu_x, \nu_y, \nu_z$  corresponds to the stacking direction. In other words, when the set of weak indices and the direction of the cut surface coincide, as in the upper left panel, no surface state appears. On the other hand, when the strong index is  $\nu_0 = 1$ , as in the lower left and lower right panels, the number of surface states is odd, in which case the surface states appear on any surface.

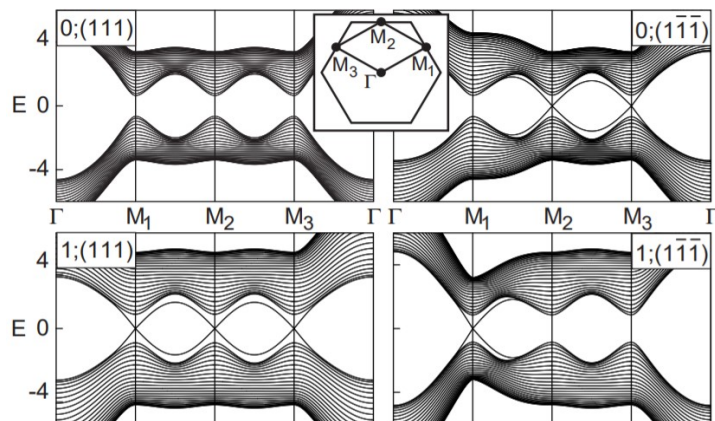


Fig. 1.6: Band structure of the model (1.18) with a (111) surface with the corresponding topological invariants. In this figure, a set of  $(\nu_0; \nu_x, \nu_y, \nu_z)$  is shown in the form as  $\nu_0; (\nu_x, \nu_y, \nu_z)$ . The weak index  $\bar{1}$  can be thought of as 0. There are odd (even) Dirac cones between the bulk band gap in the case of  $\nu_0 = 1(0)$ . The surface BZ is shown in the inset. This figure is taken from Ref. [16].

The realization of 3D topological insulators in real materials is first confirmed in  $\text{Bi}_{1-x}\text{Sb}_x$  [24], after the theoretical suggestion by Refs. [83,85]. By using an angle-resolved photoemission spectroscopy (ARPES), an odd number of Dirac cones in the band structure of  $\text{Bi}_{1-x}\text{Sb}_x$  is observed (see Fig. 1.7). In the band structure of  $\text{Bi}_{1-x}\text{Sb}_x$ , an odd number of Dirac cones appear in the case of  $0.07 \leq x \leq 0.22$ , while its band structure is complicated and the band gap is small. On the other hand, a single Dirac cone with a large bulk band gap is found in the band structure of  $\text{Bi}_2\text{Se}_3$ ,  $\text{Bi}_2\text{Te}_3$ , and  $\text{Sb}_2\text{Se}_3$ , which are called the second generation topological insulators [25, 26].

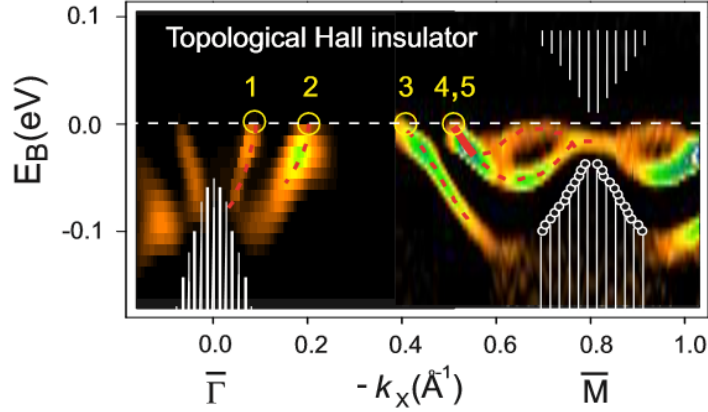


Fig. 1.7: ARPES measurement of the surface band structure of  $\text{Bi}_{0.9}\text{Sb}_{0.1}$ . The yellow circles denote Fermi crossings of the surface states. The number of them is related to the topological invariant. Since the surface band crosses Fermi surface five times between two time-reversal-invariant points  $\bar{\Gamma}$  and  $\bar{M}$ , there are an odd number of Dirac cones on the surface. This figure is taken from Ref. [24].

One of the interesting features of the surface state of 3D topological insulators is that the electric degree of freedom, or the degree of freedom corresponding to the orbital motion of electrons, is tied with the magnetic degree of freedom, or spins. Such a property is called the spin-momentum locking [17, 18, 27]. It can also be seen in helical edge states of 2D topological insulators. However, since edge states of 2D topological insulators can only move in one dimension, the result simply implies that electrons with up and down spins flow in opposite directions. On the other hand, since the surface state of 3D topological insulators flows in a 2D plane, the spin-momentum locking described above also has 2D degrees of freedom. Let us see the spin-momentum locking by considering the effective Hamiltonian for the surface of 3D topological insulators:

$$H(\mathbf{k}) = k_y \sigma_x - k_x \sigma_y. \quad (1.19)$$

The eigenvalues of the Hamiltonian are written as  $E_{\pm}(\mathbf{k}) = \pm \sqrt{k_x^2 + k_y^2}$ . We define the eigenvectors corresponding to  $E_{\pm}(\mathbf{k})$  as  $\psi_{\pm}(\mathbf{k})$ , which are written as

$$\psi_{\pm}(\mathbf{k}) = \frac{1}{\sqrt{2}} \begin{pmatrix} ik_x + k_y \\ \pm \sqrt{k_x^2 + k_y^2} \end{pmatrix}. \quad (1.20)$$

The spin direction of the eigenstates, which is given by  $(\hbar/2)\psi_{\pm}^{\dagger}(\mathbf{k})\boldsymbol{\sigma}\psi_{\pm}(\mathbf{k})$ , is described in Fig. 1.8. Since the velocity of the surface states has the same direction as  $\mathbf{k}$ , it can be seen that the direction of the electron spin is in a fixed direction perpendicular to the direction of electron motion. Due to this spin polarization, the component of the spin carried by the electron is determined by the direction of the velocity of the electron, and phenomena such as the Edelstein effect [86] can be expected. In addition, the association between the electric and magnetic degrees of freedom in the surface states in 3D topological insulators gives rise to a unique external field response, known as the topological magnetoelectric effect [28–31]. It is known that quantized orbital magnetization and electric polarization appear, which are proportional to the electric and magnetic fields, respectively.

Here, we emphasize that breaking the spin conservation is necessary to realize the strong topological insulators, as explained in the following. In the case with the conservation of spin  $i$ -component ( $i = x, y, z$ ), the electron eigenstates can be taken to have spins in the directions either  $+\mathbf{e}_i$  or  $-\mathbf{e}_i$ , where  $\mathbf{e}_i$  is the unit vector in the  $i$ -direction. While the Dirac electron states on the surface cut perpendicular to  $\mathbf{e}_i$  must have spins pointing in the surface, electron states with spins perpendicular to  $\mathbf{e}_i$  cannot be eigenstates in such a system. Thus, there cannot exist the Dirac electron states on this surface. As a result, a topological insulator conserving the spin  $i$ -component must be a weak topological insulator, and is regarded as a stacking of quantum spin Hall insulators in the  $i$ -direction.

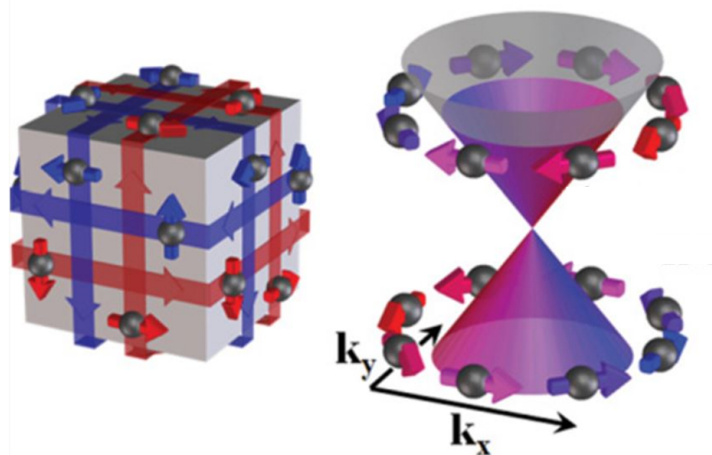


Fig. 1.8: Schematic picture of the spin directions of the electron surface states in 3D topological insulators in real and momentum spaces. They are always perpendicular to the directions of the velocity. This figure is taken from Ref. [27].

### 1.1.5 Topological crystalline insulators

As discussed in the previous section, topological insulators possess surface states protected by symmetry, which have attracted a great deal of attention. Although the first studies treated materials with time-reversal symmetry, many kinds of symmetries can be realized in materials, depending on their crystal and magnetic structures. Reflecting the mathematical structure of the wave function of electrons with such symmetries, a wide

variety of topological phases can exist. The first suggestion of the existence of materials with surface states protected by a symmetry other than time-reversal symmetry has been made by Mong, Essin, and Moore [38]. They studied combined symmetry of time-reversal and a half translation about the unit cell. The model is constructed by stacking the layers of anomalous quantum Hall insulators alternately so that their Chern numbers are opposite to each other [see Fig. 1.9]. The nearest-neighbor layers are antiferromagnetically coupled, and the systems are called antiferromagnetic topological insulators.

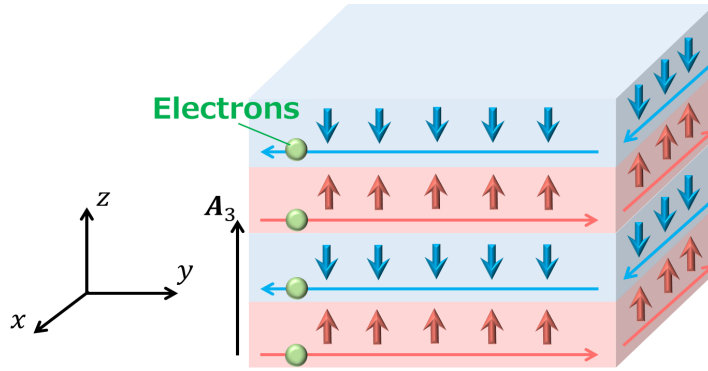


Fig. 1.9: Picture of antiferromagnetic topological insulators. Red and blue arrows are localized spins aligned upward and downward. Red and blue layers, which are anomalous quantum Hall insulators with opposite Chern numbers, are stacked alternately. In this case, the lattice vector  $\mathbf{A}_3$  is parallel to the  $z$ -axis.

As in the case of topological insulators with time-reversal symmetry, Kramers theorem plays an important role in the existence of surface states in antiferromagnetic topological insulators. When we define the combination of operators of time-reversal and translation in one-half of the lattice vector in  $\mathbf{A}_3$  direction as  $S_{1/2}(\mathbf{k})$ , it satisfies  $S_{1/2}(-\mathbf{k})S_{1/2}(\mathbf{k}) = -e^{ik_3}$ , where  $k_3 = \mathbf{k} \cdot \mathbf{A}_3$ . Unlike the time-reversal symmetry, this operator does not square to  $-1$  everywhere in the BZ. However, the square becomes  $-1$  in the  $k_3 = 0$  plane as  $S_{1/2}^2(k_3 = 0) = -1$ , which is sufficient for topological surface states to appear. The band structure of an antiferromagnetic topological insulator is shown in Fig. 1.10. A single Dirac cone, similar to that of topological insulators, appears at the point  $(0, 0)$ .

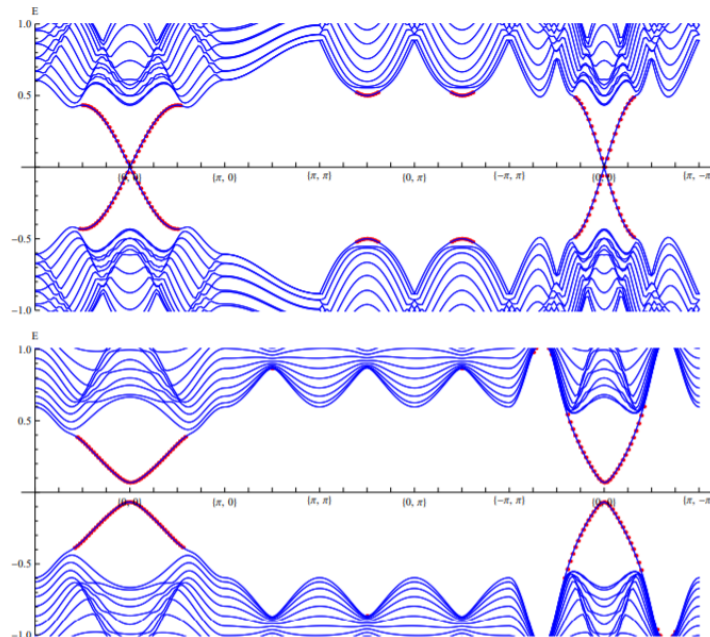


Fig. 1.10: Band structures of antiferromagnetic topological insulators considered in Ref. [38]. The top and bottom are calculated under the open boundary conditions with (100) and  $(\bar{1}\bar{1}1)$  surfaces, respectively. The Dirac cone appears only in the surface which is parallel to  $\mathbf{A}_3$ , i.e., (100) surface in this case. This figure is taken from Ref. [38].

We note that unlike the case of the topological insulators, whether the surface states appear or not depends on what direction the surface is cut. The surface states appear only when the surface is parallel to the lattice vector  $\mathbf{A}_3$ . The band structures of antiferromagnetic topological insulators under two types of open boundary conditions are shown in Fig. 1.10. The top and bottom panels in Fig. 1.10 is calculated when the system has the (100) surface which is parallel to  $\mathbf{A}_2$ ,  $\mathbf{A}_3$  and the  $(\bar{1}\bar{1}1)$  surface which is parallel to  $\mathbf{A}_1$ ,  $\mathbf{A}_2$ , respectively. Here,  $\mathbf{A}_1$  and  $\mathbf{A}_2$  are the lattice primitive vectors which are different from  $\mathbf{A}_3$ . We can see that a Dirac cone exists in the former case, while in the latter case the band gap is open.

So far, topological crystalline insulators [32, 33], which have gapless surface states protected by a wide variety of crystalline symmetries, are studied. The interesting feature is that, depending on which symmetry the surface states are protected by, the properties of the surface states are different. For example, the dispersion of the surface states in the topological crystalline insulators, which is symmetric under the combination of time-reversal and rotation, is quadratic.

The theoretical study [34] predicted that SnTe is a topological crystalline insulator with mirror symmetry. The symmetry-protected surface states in SnTe are observed in the ARPES experiment [35] [see Fig. 1.11]. Surface states protected by mirror symmetry is also observed in other several insulators such as  $\text{Pb}_{1-x}\text{Sn}_x\text{Se}$  ( $x = 0.23$ ) [36] and  $\text{Pb}_{1-x}\text{Sn}_x\text{Te}$  ( $x = 0.4$ ) [37].

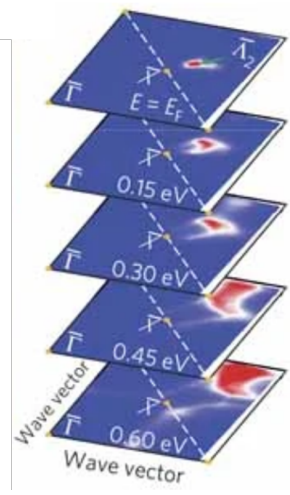


Fig. 1.11: ARPES intensity mappings for SnTe in the 2D BZ observed at various binding energies. We can see the shape of Dirac dispersion, which is shown by red. It is evidence of the topological crystalline insulator. This figure is taken from Ref. [35].

### 1.1.6 Nonlinear Hall effect

As we discussed in Secs. 1.1.2 and 1.1.3, the Berry curvature of electrons gives rise to interesting phenomena such as transverse quantized currents and spin currents. In the linear response regime, the transverse current of the Hall effect is represented by the integral of the Berry curvature over BZ. However, for this value to be finite, the time-reversal symmetry must be broken by a magnetic field or magnetization; i.e., the complex hopping term must be included in the Hamiltonian. On the other hand, it has become clear that in the nonlinear response regime, the Hall effect can appear even without breaking time-reversal symmetry or complex hopping term. The remarkable study is the nonlinear Hall effect [39–55]. In this section, the Dirac constant  $\hbar$  is taken to be unity.

Let us consider the current induced by applying an electric field of frequency  $\omega$  and amplitude  $\mathcal{E}_c$ :  $E_c(t) = \text{Re}[\mathcal{E}_c e^{i\omega t}]$ . The current is given by

$$j_a = -e \int_{\text{BZ}} d\mathbf{k} f(\epsilon(\mathbf{k})) v_a(\mathbf{k}), \quad (1.21)$$

$$v_a(\mathbf{k}) = \frac{\partial}{\partial k_a} \epsilon(\mathbf{k}) + \epsilon_{abc} \Omega_b(\mathbf{k}) \dot{k}_c, \quad (1.22)$$

where  $a, b$ , and  $c$  are indices for  $x, y$ , and  $z$ . Here,  $\mathbf{v}(\mathbf{k})$ ,  $\epsilon(\mathbf{k})$ ,  $\epsilon_{abc}$ , and  $\mathbf{\Omega}(\mathbf{k})$  are the velocity of electrons, the energy of electrons, the Levi-Civita symbol, and the Berry curvature, respectively. The nonequilibrium distribution function  $f(\epsilon(\mathbf{k}))$  can be calculated by using the Boltzmann equation with the relaxation time approximation:

$$-e\tau E_a \frac{\partial}{\partial k_a} f(\epsilon(\mathbf{k})) + \tau \frac{\partial}{\partial t} f(\epsilon(\mathbf{k})) = f_0(\epsilon(\mathbf{k})) - f(\epsilon(\mathbf{k})), \quad (1.23)$$

where  $f_0(\epsilon(\mathbf{k}))$  and  $\tau$  are the equilibrium distribution function in the case without the external field and the relaxation time, respectively. As a result, Hall current as a second-order response to the electric field can be written as follows:

$$j_a = \text{Re}[j_a^0 + j_a^{2\omega} e^{2i\omega t}]. \quad (1.24)$$

Here,  $j_a^0$  and  $j_a^{2\omega}$  are given by

$$j_a^0 = \frac{e^2}{2} \int_{\text{BZ}} d\mathbf{k} \epsilon_{abc} \Omega_b(\epsilon(\mathbf{k})) \mathcal{E}_c^* \frac{e\tau \mathcal{E}_a \frac{\partial}{\partial k_a} f_0(\epsilon(\mathbf{k}))}{1 + i\omega\tau}, \quad (1.25)$$

$$j_a^{2\omega} = \frac{e^2}{2} \int_{\text{BZ}} d\mathbf{k} \epsilon_{abc} \Omega_b(\epsilon(\mathbf{k})) \mathcal{E}_c \frac{e\tau \mathcal{E}_a \frac{\partial}{\partial k_a} f_0(\epsilon(\mathbf{k}))}{1 + i\omega\tau}. \quad (1.26)$$

They can be rewritten as

$$j_a^0 = -\frac{e^3\tau}{1 + i\omega\tau} \epsilon_{adc} \mathcal{E}_b \mathcal{E}_c^* \int_{\text{BZ}} d\mathbf{k} f_0(\epsilon(\mathbf{k})) \frac{\partial}{\partial k_b} \Omega_d(\mathbf{k}), \quad (1.27)$$

$$j_a^{2\omega} = -\frac{e^3\tau}{1 + i\omega\tau} \epsilon_{adc} \mathcal{E}_b \mathcal{E}_c \int_{\text{BZ}} d\mathbf{k} f_0(\epsilon(\mathbf{k})) \frac{\partial}{\partial k_b} \Omega_d(\mathbf{k}). \quad (1.28)$$

From these equations, we see that the nonlinear Hall current is described by the Berry curvature dipole:  $D_{ab} = \int_{\text{BZ}} d\mathbf{k} f_0(\epsilon(\mathbf{k})) (\partial/\partial k_a) \Omega_b(\mathbf{k})$ . Since  $\partial/\partial k_a$  and  $\Omega_b(\mathbf{k})$  are odd under time reversal, the Berry curvature dipole is even. Therefore, it can be nonzero even under time-reversal symmetry.

In addition, the Berry curvature dipole does not require any flux in the hopping terms, and often appears when the crystal breaks inversion and rotation symmetries. Thus, the nonlinear Hall effect is expected to occur in materials even without magnetization, spin-orbit interaction, or an applied magnetic field.

The nonlinear Hall effect has actually been observed in WTe<sub>2</sub> [54, 55]. The result of the observed transverse current corresponding to  $j_a^{2\omega}$  is shown in Fig. 1.12. Layered WTe<sub>2</sub> was chosen as a target of the observation of the nonlinear Hall effect since it breaks inversion and rotation symmetries but does not break time-reversal symmetry.

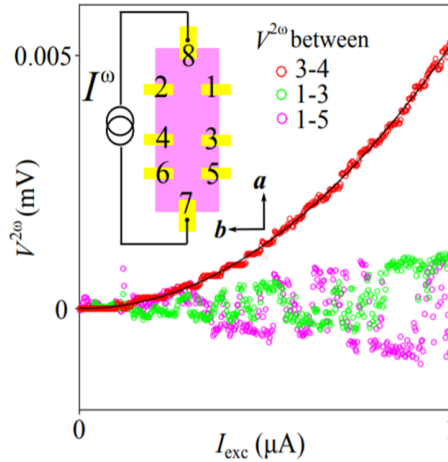


Fig. 1.12: Observed AC voltage versus the current in  $WTe_2$ . Red circles correspond to the transverse current, which is evidence for the nonlinear Hall effect. We can see that the transverse current is quadratic in the applied current  $I_{exc}$ , and is dominant over the longitudinal current shown by purple and green circles in relatively large  $I_{exc}$ . This figure is taken from Ref. [54].

## 1.2 Brief introduction to studies on magnons related to our work

Among particles in matters, magnons, which are quasiparticles of spin waves, have attracted much attention as an alternative transport carrier in matters to electrons because they can carry spin currents over long distances without Joule heating [84, 143]. In magnetically ordered systems, low-energy excitations are manifested in the form of precessional motion in the semi-classical description due to deviations from the ordered direction of the spins. They are represented by propagating spin waves. Since the spin angular momentum is quantized, this spin deviation is also discrete. Thus, spin waves can be described as quantum mechanical particles and are called magnons. It has been experimentally confirmed that magnons can propagate in magnetic materials such as yttrium iron garnet (YIG) over long distances of about 10 mm [87–92]. Spin currents carried by magnons are used instead of electric charges, for example, to design logic circuits [93–96].

In recent years, many nontrivial properties of magnons have been investigated by introducing the concept of topological properties, which have been rapidly developed in electronic systems. The magnon thermal Hall effect [97–119] and the spin Nernst effect [120–124], in which energy and spin currents flow in the direction perpendicular to both the temperature gradient and the magnetization, are unconventional properties associated with the topology of the magnon band structure in magnetic insulators. Magnons with linear dispersion such as Weyl [125–129] and Dirac [130–134] semimetals, which show many nontrivial properties, have also been studied. Many experimental observations of

nontrivial topological properties of magnons were conducted immediately after the theoretical proposal. The thermal Hall effect and the spin Nernst effect in magnons were observed in the pyrochlore ferromagnet  $\text{Lu}_2\text{V}_2\text{O}_7$  [99] and the honeycomb antiferromagnet  $\text{MnPS}_3$  [124], respectively, soon after the theoretical study [98, 120]. Magnon Dirac dispersion was also observed in the antiferromagnet  $\text{Cu}_3\text{TeO}_6$  by neutron scattering [134] just after it was suggested to exist by the magnon band calculation [133]. In particular, the thermal Hall effect and spin Nernst effect of magnons can be described in terms of the Berry curvature of magnons. In the topological properties of magnons, Dzyaloshinskii-Moriya (DM) interaction [135–137] plays an important role. It gives a complex hopping term to the Hamiltonian of magnons, similar to what the spin-orbit interaction does to electrons, which endows the Bloch wavefunction of magnons with the Berry curvature.

There are also cases that the magnon thermal Hall effect and spin Nernst effect are contributed by the boundary states, which result from the nontrivial topology of the magnon band structure. While magnons have no Fermi surface due to Bose statistics, edge states [138–142] crossing gaps between bulk bands appear corresponding to the Chern number [141] or  $\mathbb{Z}_2$  topological number [142] of the bulk band. While such magnon boundary states have not yet been observed, it is expected to be discovered in the future with improved measurement technology. In Chap. 2, we discuss the details of the description of magnons and the above topological properties.

### 1.3 Purpose and organization of this thesis

The purpose of this thesis is to extend the stage of topological properties of magnons to the realm of higher dimensions or the nonlinear response regime and to search for unconventional phenomena in magnetic materials. Magnons, which are quasiparticles in magnetic materials, are attracting attention in the field of spintronics as an alternative transport carrier in materials [84, 143]. Topological properties of magnons are expected to be a treasure trove of novel phenomena in magnets that have not been observed in either topological electronic or conventional magnonic systems. However, even a magnonic counterpart of 3D topological insulators, which is recognized as one of the most significant studies on electronic topological materials, has not been considered. As is the case in electronic systems, many nontrivial properties can be expected in 3D magnetic materials with Dirac surface states of magnons protected by symmetry. We will investigate symmetries in magnets and realize theoretically the surface states in the magnon systems. We also focus on the fact that most of the magnon topological transport phenomena have been investigated mostly in the range of linear response. It is expected that further new phenomena will be found by exploring the region including nonlinear ones.

The remaining part of this thesis is organized as follows. In Chap. 2, we discuss the formulation and basic properties of magnons as well as important studies on the topological properties of magnons. The results obtained in this thesis are shown in the following chapters. In Chap. 3, we propose a model for the magnonic analog of 3D topological insulators, i.e., a magnetic material which has symmetry-protected Dirac surface states of magnons [144]. The model is constructed based on the pseudo-time-reversal symmetry which is discussed in Sec. 2.6. However, the proposed model seems

difficult to be realized experimentally since the setup is quite artificial. On the other hand, magnonic analogs of topological crystalline insulators, which have the surface states protected by crystal symmetries, can be realized more naturally. In Chap. 4, we propose a model that realizes the magnon Dirac surface states in a much more realistic setup in a magnetic material with a combined symmetry of time-reversal and half-translation [145]. We discuss the realization of the model in the van der Waals magnet  $\text{CrI}_3$  [146–155]. We also propose a unique external field response that arises from the spin-momentum locking of the Dirac surface state. In the next study, we consider the transport phenomena related to the Berry curvature of magnons in the region beyond the linear response regime. The study of the nonlinear response of magnons so far include the nonlinear Hall effect [122], spin Seebeck effect [156], and optical response [157, 158]. In Chap. 5, by constructing a second-order response theory for magnons with respect to temperature gradients, we show that the nonlinear transverse current is associated with the extended Berry curvature dipole of magnons [159]. We show that such nonlinear spin Nernst current, originating from the extended Berry curvature dipole in antiferromagnets, can be widely realized in magnetic materials without the DM interaction. In particular, the spin current is generated in a simple honeycomb lattice antiferromagnet and can be redirected by the lattice distortion. We summarize our studies and discuss the future prospects in Chap. 6. The studies on the topologically nontrivial properties which are discussed in this thesis are listed in Tab 1.1. The results of this thesis are shown with asterisks.

Tab. 1.1: The summary of the topological properties which are particularly relevant to this thesis. The first column lists the name of topological materials and effects. The references, which proposed or experimentally observed in electronic systems and corresponding magnonic systems, are shown in the second and the third columns, respectively. Asterisks are added to the studies which are the results of this thesis.

Materials (Effect)	Electrons	Magnons
Quantum Hall insulators	[1], [2] (Sec. 1.1.2)	[98], [99] (Sec. 2.3)
Quantum spin Hall insulators	[9], [10], [11] (Sec. 1.1.3)	[121], [142] (Sec. 2.6)
3D topological insulators	[16], [24] (Sec. 1.1.4)	[144] (Chap. 3) *
Topological crystalline insulators	[32], [35] (Sec. 1.1.5)	[145] (Chap. 4) *
Nonlinear Hall (Nernst) effect	[39], [54] (Sec. 1.1.6)	[122] (Sec. 2.3)
Nonlinear spin Hall (Nernst) effect	N/A	[159] (Chap. 5) *

## Chapter 2

# Topological properties of magnons: formalism and applications

As seen in the previous chapter, studies on the transverse transport phenomena and edge (surface) states due to Berry curvature have led to significant results in electronic systems. An important question is whether they can be realized in other systems, and the answer is yes. Topological properties reminiscent of the Hall effect have been studied in bosonic systems such as those of magnons [97–134], photons [160–166], phonons [167–179], and triplons [180–184]. In particular, we are interested in the topological properties of magnons since they are responsible for the novel transport phenomena in magnets. In this chapter, after explaining the basic properties of magnons, we will discuss in detail some of the topological properties in magnon systems that are particularly relevant to our studies. The description and basic properties of magnons are discussed in Sec. 2.1. In Sec. 2.2, we show how to obtain the energy eigenvalues of magnons described by Bogoliubov-de Gennes (BdG) Hamiltonians. The DM interaction which plays an important role in topological properties of magnons, and the thermal Hall effect of magnons are explained in Sec. 2.3. In Sec. 2.4, we introduce a study of the magnon transverse current in the nonlinear response regime. In Secs. 2.5 and 2.6, we show the studies on the spin Nernst effect contributed by the bulk magnons and the magnon helical edge states in antiferromagnets, respectively.

## 2.1 Basic properties of magnons

Let us introduce the notation and the spin-wave approximation. To begin with, we assume the spin with magnitude  $S$  is located at each lattice site. Here, we define an operator of the spin operator at site  $i$  as  $\mathbf{S}_i = (S_i^x, S_i^y, S_i^z)$ . The spin operator satisfies the commutation relation  $[S_i^a, S_j^b] = i\delta_{ij}\epsilon_{abc}S_i^c$ , where the Dirac constant is taken to be  $\hbar = 1$ . Here,  $\epsilon_{abc}$  is the Levi-Civita symbol. We take the basis at site  $i$  as the eigenstates of  $S_i^z$ , i.e.,  $|m_i\rangle$  ( $m_i = -S, -S + 1, \dots, S - 1, S$ ). These states satisfy the following equations:

$$\mathbf{S}_i^2 |m_i\rangle = S(S + 1) |m_i\rangle, \quad (2.1)$$

$$S_i^z |m_i\rangle = m_i |m_i\rangle. \quad (2.2)$$

We define the spin raising and lowering operators as  $S_i^\pm = S_i^x \pm iS_i^y$ , respectively. The following commutation relations are satisfied:

$$[S_i^z, S_i^\pm] = \pm S_i^\pm, \quad (2.3)$$

$$[S_i^+, S_i^-] = 2S_i^z. \quad (2.4)$$

Thus, when acting on the state  $|m_i\rangle$ ,  $S_i^\pm$  changes the eigenvalues of  $S_i^z$  by  $\pm 1$ , which results in the following equation:

$$S_i^\pm |m_i\rangle = \sqrt{S(S+1) - m_i(m_i \pm 1)} |m_i \pm 1\rangle. \quad (2.5)$$

For example, when a magnetic field is applied in the  $z$ -direction, the ground state of each site is represented by  $|m_i = S\rangle$ . The first excited state  $|m_i = S - 1\rangle$  is a spin precession with a slight deviation from the  $z$ -direction, which is actually close to the picture of a magnon at site  $i$ .

In general, the eigenstate  $|m_i\rangle$  can be interpreted as a state in which the number of magnons is  $n_i = S - m_i$ . When we define the number operator of magnons as  $N_i = S - S_i^z$ , then the annihilation and creation operators  $b_i$  and  $b_i^\dagger$  of magnons such that  $N_i^{\text{op}} = b_i^\dagger b_i$  acts on the eigenstate  $|m_i\rangle$  of  $S_i^z$  as follows:

$$b_i^\dagger |m_i = S - n_i\rangle = \sqrt{n_i + 1} |m_i = S - (n_i + 1)\rangle, \quad (2.6)$$

$$b_i |m_i = S - n_i\rangle = \sqrt{n_i} |m_i = S - (n_i - 1)\rangle, \quad (2.7)$$

$$b_i^\dagger b_i |m_i = S - n_i\rangle = n_i |m_i = S - n_i\rangle. \quad (2.8)$$

Here, we note that  $b_i$  and  $b_i^\dagger$  satisfy  $[b_i, b_i^\dagger] = 1$ . By using Eqs. (2.6) to (2.8), the action of  $S_i^+$  to the states with the number of magnons  $n_i$  is reproduced when we redefine  $S_i^+$  as  $S_i^+ = \sqrt{2S - N_i^{\text{op}}} b_i$ . This can be confirmed by the following calculation:

$$\begin{aligned} S_i^+ |m_i = S - n_i\rangle &= \sqrt{S(S+1) - (S - n_i)(S - n_i + 1)} |m_i = S - n_i + 1\rangle \\ &= \sqrt{2S + 1 - (N_i^{\text{op}} + 1)} \sqrt{n_i} |m_i = S - n_i + 1\rangle \\ &= \sqrt{2S - N_i^{\text{op}}} b_i |m_i = S - n_i\rangle. \end{aligned} \quad (2.9)$$

Thus, we can take the following mapping from the spin operator to the magnon annihilation and creation operators:

$$S_i^z = S - N_i^{\text{op}}, \quad (2.10)$$

$$S_i^+ = \sqrt{2S - N_i^{\text{op}}} b_i, \quad (2.11)$$

$$S_i^- = b_i^\dagger \sqrt{2S - N_i^{\text{op}}}. \quad (2.12)$$

This is called Holstein-Primakoff transformation [185]. The commutation relations of the spin operators are directly related to those of magnons. In particular, when the temperature is low enough and the number of excited magnons is sufficiently small compared

to the magnitude of spins  $S$ , the Holstein-Primakoff transformation can be written in a simplified form:

$$S_i^z = S - N_i, \quad (2.13)$$

$$S_i^+ \simeq \sqrt{2S}b_i, \quad (2.14)$$

$$S_i^- \simeq \sqrt{2S}b_i^\dagger. \quad (2.15)$$

In a magnetic material where the spins are correlated with each other, the precessional motion from the spin configuration in the ground state propagates as a wave. Let us consider a Heisenberg ferromagnet with the Hamiltonian  $H = J \sum_{\langle i,j \rangle} \mathbf{S}_i \cdot \mathbf{S}_j$ , where the summation is taken over the nearest-neighbor sites. After applying the Holstein-Primakoff transformation, it can be diagonalized by the Fourier transformation  $b_k^\dagger = \sum_i e^{ikr_i} b_i^\dagger$  under periodic boundary conditions. In this case, the phase factor  $e^{ikr_i}$  corresponds to the azimuthal angle of the direction of the precessional motion of the spin. A schematic picture of spin waves propagating through a magnet is shown in Fig. 2.1.

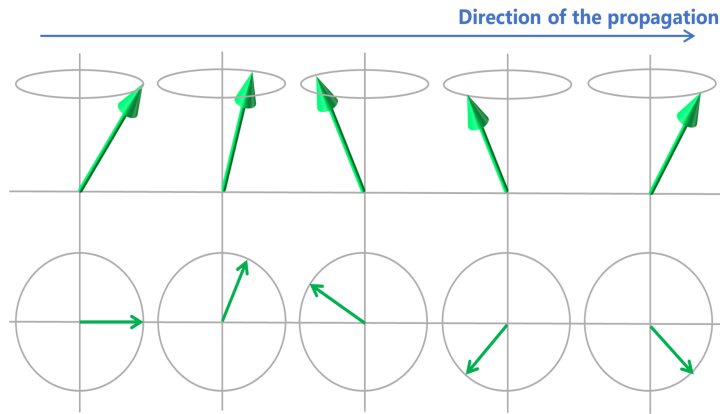


Fig. 2.1: Precession of the propagation of the spin waves. The low energy collective excitation in the ordered magnets can be described as the propagation of such a deviation from the ordered direction of the spins.

Here, a spin  $z$ -component of the one-magnon state  $|\mathbf{k}\rangle = b_k^\dagger |0\rangle$  one less than that of the ground state of the ferromagnetic Hamiltonian  $|0\rangle$ , i.e.,  $\langle \mathbf{k} | (S_i^z - S) | \mathbf{k} \rangle = -1$ . Thus, in the case where the spins are aligned in the  $+z$  direction in the ground state, the magnon carries a magnetic angular momentum of  $-\hbar$ . As the transport properties of magnons, two physical quantities, spin angular momentum and energy, are of interest.

## 2.2 Diagonalization of bosonic Bogoliubov-de Gennes Hamiltonians

In magnets with antiferromagnetic or non-collinear spin configurations, magnons are described by the bosonic BdG Hamiltonians [186,187]. In such cases, the number of magnons

no longer preserves. The intrinsic topological classifications of bosonic BdG Hamiltonians and their realization in magnon systems are reviewed in Ref. [188]. In this part, we explain the way to obtain the energy eigenvalues and eigenstates of the systems which are described by the bosonic BdG Hamiltonian. The discussion here is based on Ref. [186]. We also show the expression of the Berry connection and curvature of the system. Let us consider the bosonic BdG Hamiltonian in  $k$ -space as follows:

$$\mathcal{H} = \frac{1}{2} \sum_{\mathbf{k}} \phi^\dagger(\mathbf{k}) H(\mathbf{k}) \phi(\mathbf{k}), \quad (2.16)$$

$$\phi^\dagger(\mathbf{k}) = [\beta_1^\dagger(\mathbf{k}), \dots, \beta_{\mathcal{N}}^\dagger(\mathbf{k}), \beta_1(-\mathbf{k}), \dots, \beta_{\mathcal{N}}(-\mathbf{k})], \quad (2.17)$$

where  $\beta_i^\dagger(\mathbf{k})$  is the creation operator of bosons with the momentum  $\mathbf{k}$ . Here, the subscript  $\mathcal{N}$  is the number of internal degrees of freedom in a unit cell. The matrix  $H(\mathbf{k})$  is given by

$$H(\mathbf{k}) = \begin{pmatrix} h(\mathbf{k}) & \Delta(\mathbf{k}) \\ \Delta^*(-\mathbf{k}) & h^*(-\mathbf{k}) \end{pmatrix}. \quad (2.18)$$

When we consider the system without dissipation, the Hamiltonian is Hermitian, leading to  $h(\mathbf{k}) = h^\dagger(\mathbf{k})$  and  $\Delta^T(\mathbf{k}) = \Delta(-\mathbf{k})$ . The commutation relation satisfied by the components of the operator  $\phi(\mathbf{k})$  is written as  $[\phi_i(\mathbf{k}), \phi_j^\dagger(\mathbf{k}')] = (\Sigma_z)_{ij} \delta_{\mathbf{k}, \mathbf{k}'}$ . Here,  $\Sigma_z$  is defined as a tensor product  $\Sigma_z := \sigma_z \otimes 1_{\mathcal{N}}$ , where  $\sigma_a$  ( $a = x, y, z$ ) is the  $a$ -component of the Pauli matrix acting on the particle-hole space and  $1_{\mathcal{N}}$  is the  $\mathcal{N} \times \mathcal{N}$  identity matrix.

The linear combinations of bosons, which create eigenstates of bosonic BdG Hamiltonians, should be bosonic. Thus, the corresponding operator  $\psi_i(\mathbf{k})$  satisfies the commutation relations the same as  $\phi_i(\mathbf{k})$ , i.e.,  $[\psi_i(\mathbf{k}), \psi_j^\dagger(\mathbf{k}')] = (\Sigma_z)_{ij} \delta_{\mathbf{k}, \mathbf{k}'}$ . The operator  $\psi_i(\mathbf{k})$  is written as  $\psi_i(\mathbf{k}) = (T^{-1}(\mathbf{k})\phi(\mathbf{k}))_i$ , where  $T(\mathbf{k})$  is the matrix which diagonalizes the matrix  $H(\mathbf{k})$ . We here discuss under what conditions  $T(\mathbf{k})$  leaves the bosonic commutation relation unchanged. The commutator of  $\psi_i(\mathbf{k})$  is written as follows:

$$\begin{aligned} [\psi_i(\mathbf{k}), \psi_j^\dagger(\mathbf{k}')] &= [(T^{-1}(\mathbf{k}))_{ik} \phi_k(\mathbf{k}), (T^{-1}(\mathbf{k}'))_{j'l}^* \phi_l^\dagger(\mathbf{k}')] = (T^{-1}(\mathbf{k}))_{ik} (\Sigma_z)_{kl} (T^{-1}(\mathbf{k}'))_{jl}^* \\ &= (T^{-1}(\mathbf{k}) \Sigma_z (T^{-1}(\mathbf{k}'))^\dagger)_{ij}, \end{aligned} \quad (2.19)$$

where repeated indices are summed over. Thus, the commutation relation  $[\psi_i(\mathbf{k}), \psi_j^\dagger(\mathbf{k}')] = (\Sigma_z)_{ij} \delta_{\mathbf{k}, \mathbf{k}'}$  correspond to the following para-unitary condition:

$$T(\mathbf{k}) \Sigma_z T^\dagger(\mathbf{k}) = \Sigma_z. \quad (2.20)$$

The matrix  $T(\mathbf{k})$  satisfying the above para-unitarity is called para-unitary matrix. Thus, we must diagonalize the BdG Hamiltonian by using a matrix satisfying the above para-unitarity (2.20).

To obtain the energy eigenvalues of bosons and the para-unitary matrix  $T(\mathbf{k})$ , it is useful to note certain properties of  $\Sigma_z H(\mathbf{k})$ . When the matrix  $H(\mathbf{k})$  is positive definite, the following three statements hold:

- (i) The eigenvalues of the matrix  $\Sigma_z H(\mathbf{k})$  are real and nonzero.
- (ii) If  $\mathbf{v}(\mathbf{k})$  is an eigenvector of  $\Sigma_z H(\mathbf{k})$  with eigenvalue  $E(\mathbf{k})$ , then  $\Sigma_x \mathbf{v}^*(-\mathbf{k})$  is an eigenvector of  $\Sigma_z H(\mathbf{k})$  with eigenvalue  $-E(\mathbf{k})$ , where  $\Sigma_x := \sigma_x \otimes 1_{\mathcal{N}}$ .
- (iii) Eigenvectors can be taken to satisfy para-orthogonality  $\mathbf{v}_{n\sigma}^\dagger(\mathbf{k}) \Sigma_z \mathbf{v}_{m\rho}(\mathbf{k}) = \sigma \delta_{nm} \delta_{\sigma\rho}$ , where  $n = 1, \dots, \mathcal{N}$  and  $\sigma = \pm, 2\mathcal{N}$ .

The proof of these are shown in Appendix A. By using (i), (ii), and (iii), we can see that the para-unitarity Eq. (2.20) is satisfied by the following matrix  $T(\mathbf{k})$ :

$$T(\mathbf{k}) = (\mathbf{v}_{1+}(\mathbf{k}), \dots, \mathbf{v}_{\mathcal{N}+}(\mathbf{k}), \mathbf{v}_{1-}(\mathbf{k}), \dots, \mathbf{v}_{\mathcal{N}-}(\mathbf{k})), \quad (2.21)$$

where the eigenvectors  $\mathbf{v}_{n+}(\mathbf{k})$  and  $\mathbf{v}_{n-}(\mathbf{k})$  are related by  $\mathbf{v}_{n+}(\mathbf{k}) = \Sigma_x \mathbf{v}_{n-}^*(-\mathbf{k})$  ( $n = 1, \dots, \mathcal{N}$ ). The Hamiltonian is diagonalized by  $T(\mathbf{k})$  as follows:

$$T^\dagger(\mathbf{k}) H(\mathbf{k}) T(\mathbf{k}) = \text{diag}(E_1(\mathbf{k}), \dots, E_{\mathcal{N}}(\mathbf{k}), E_1(-\mathbf{k}), \dots, E_{\mathcal{N}}(-\mathbf{k})). \quad (2.22)$$

Therefore, solving the eigenvalue problem  $\Sigma_z H(\mathbf{k}) \mathbf{v}(\mathbf{k}) = E(\mathbf{k}) \mathbf{v}(\mathbf{k})$ , we obtain the eigenvalues and the para-unitary matrix automatically. Since the  $\Sigma_z H(\mathbf{k})$  is no longer Hermitian, the bosonic BdG systems should be understood in terms of non-Hermitian quantum systems. As in above (iii), as a result of the non-Hermiticity, the para-orthogonality is satisfied under the inner product different from that of Hermitian systems. Therefore, we introduce the inner product as follows:

$$\langle\langle \phi, \psi \rangle\rangle = \phi^\dagger \Sigma_z \psi, \quad (2.23)$$

where  $\phi$  and  $\psi$  are the  $2\mathcal{N}$ -dimensional vectors. Reflecting this, the Berry connection and curvature of the bosonic systems described by BdG Hamiltonian are written as

$$\mathbf{A}_{n\sigma}(\mathbf{k}) = i\sigma \langle\langle \mathbf{v}_{n\sigma}(\mathbf{k}), \mathbf{v}_{n\sigma}(\mathbf{k}) \rangle\rangle \quad (2.24)$$

$$\mathbf{\Omega}_{n\sigma}(\mathbf{k}) = \nabla_{\mathbf{k}} \times \mathbf{A}_{n\sigma}(\mathbf{k}). \quad (2.25)$$

The detailed derivation of these formulas is given in Ref. [103].

## 2.3 Dzyaloshinskii-Moriya interaction and the thermal Hall effect of magnons

The DM interaction [135–137], which is an effective interaction that appears between spins via the spin-orbit interaction, contributes to the realization of topologically nontrivial magnon states. The Hamiltonian of the DM interaction between the sites  $i$  and  $j$  is, in many cases, given by  $H_{ij}^{\text{DM}} = \mathbf{D}_{ij} \cdot (\mathbf{S}_i \times \mathbf{S}_j)$ , where  $\mathbf{D}_{ij}$  is a vector determined by the crystal structure. This interaction gives a complex hopping term to the magnon Hamiltonian in a similar way that the spin-orbit interaction does to electron Hamiltonians. As an example, let us consider a two-dimensional ferromagnet with magnetization in the  $+z$  direction. In many 2D magnetic materials,  $\mathbf{D}_{ij}$  points in the  $z$ -direction as

$\mathbf{D}_{ij} = D\mathbf{e}_z$ . By applying the Holstein-Primakoff transformation,  $H_{ij}^{\text{DM}}$  can be written as  $H_{ij}^{\text{DM}} = iDSb_i^\dagger b_j + \text{h.c.}$ .

Magnons in ferromagnets with DM interactions can be described in a similar way as quantum Hall insulators in electronic systems discussed in Sec. 1.1.2. Since magnons with no electric charge cannot be driven by an electric field, a temperature gradient is instead applied as a driving force. Magnons excited from spins aligned in the  $z$ -direction acquire complex phases through the DM interaction, which results in the Berry curvature of magnons. This contributes to the magnon current in a direction perpendicular to the temperature gradient, leading to a transverse thermal current. A schematic picture of the magnon thermal Hall effect is shown in Fig. 2.2. It was observed experimentally [99] soon after the theoretical proposal [98] and triggered a great deal of interest in the topological properties of magnons.

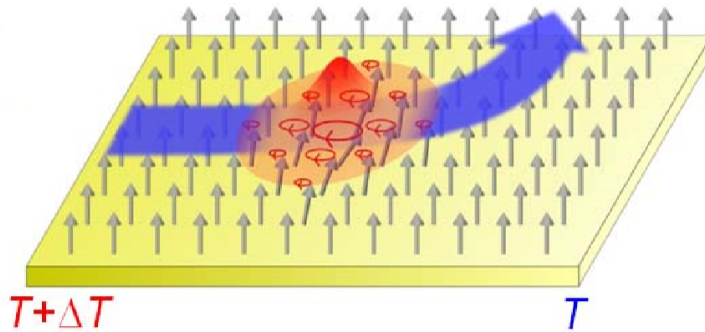


Fig. 2.2: Schematic picture of the magnon thermal Hall effect. Spins in a ferromagnet are aligned in the  $z$ -direction due to an applied magnetic field. Berry curvature of magnons arising from the DM interaction results in the current flowing in the direction perpendicular to both the magnetic field and the temperature gradient. This figure is taken from Ref. [99].

In the theoretical study [98], the kagome lattice ferromagnet with the fictitious fluxes shown in Fig. 2.3 (a), which would be induced by the DM interaction, is proposed as a model exhibiting the magnon thermal Hall effect. These fictitious fluxes open gaps between the three bulk bands of magnons. The Chern numbers of the lower, middle, and top bands are defined as  $\text{Ch}_n = \int_{\text{BZ}} d\mathbf{k} \Omega_n(\mathbf{k})$  ( $n = 1, 2, 3$ ), and are calculated as  $-1, 0$ , and  $1$ , respectively. Here,  $\Omega_n(\mathbf{k}) = -2\text{Im} \langle (\partial/\partial k_x)u_n(\mathbf{k}) | (\partial/\partial k_y)u_n(\mathbf{k}) \rangle$  is the Berry curvature of magnons with the  $n$ th eigenvector  $|u_n(\mathbf{k})\rangle$ . We note that the expression of the Berry curvature in this case is the same as that of electrons, since magnons in the ferromagnets are usually described not by the BdG Hamiltonian, but by the Hamiltonian without pairing terms. The bulk-edge correspondence similar to that of electrons can be confirmed as well for magnons [141]. In Fig. 2.3 (b), which is the result of the band calculation for a finite strip, we can see the chiral edge states of magnons between the three bulk bands.

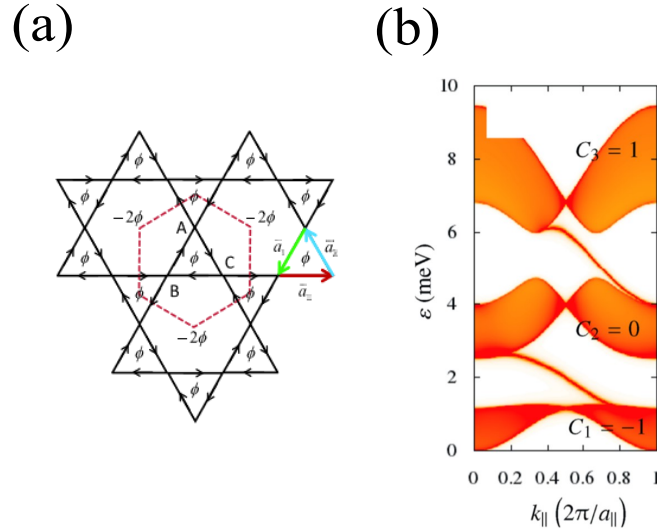


Fig. 2.3: (a) Kagome lattice system with fictitious fluxes. Magnons obtain the complex phase of  $\phi$ , when going around a triangle consisting of three lattice sites along the direction indicated by the arrows. These complex phases are the same as the ones that the DM interaction induces to magnons on the kagome layers within the pyrochlore lattice. (b) Magnon band structure of the kagome lattice ferromagnet with DM interaction. The Chern numbers of the three bands are 1, 0, and  $-1$ , respectively. Chiral edge states of magnons can be seen between the band gaps. Figures (a) and (b) are taken from Refs. [98] and [110], respectively.

The expression of the magnon thermal Hall coefficient originally derived in Ref. [98] should be modified by taking into account the orbital angular momentum of magnons. The correct formula was obtained in Ref. [101] and is eventually written as follows:

$$\kappa^{xy} = -\frac{k_B^2 T}{\hbar V} \sum_{n, \mathbf{k}} c_2(\rho_0(\epsilon_n(\mathbf{k}))) \Omega_n(\mathbf{k}), \quad (2.26)$$

where  $k_B$ ,  $T$ ,  $V$ ,  $\rho_0$ , and  $\epsilon_n(\mathbf{k})$  are the Boltzmann constant, temperature, the volume of the system, the Bose distribution function, and the energy of the  $n$ th band, respectively. By using the polylogarithm function  $\text{Li}_2(-\rho)$ , the function  $c_2(\rho)$  is defined as  $c_2(\rho) = (1 + \rho) \left( \log \frac{1+\rho}{\rho} \right)^2 - (\log \rho)^2 - 2\text{Li}_2(-\rho)$ . From a semi-classical description of magnons, the formula Eq. (2.26) is derived in Appendix B.

When magnons are described by a BdG Hamiltonian, the thermal Hall coefficient can be given in the same form as Eq. (2.26) with the replacement of the Berry curvature  $\Omega_n(\mathbf{k})$  by  $\Omega_{n+}(\mathbf{k})$  in Eq. (2.25). Although one-half of the eigenvalues of the matrix  $\Sigma_z H(\mathbf{k})$  are positive and the others are negative, the summation is taken only over the eigenstates with positive eigenvalues. As you can see from Eq. (2.26), the thermal Hall current is not directly related to the Chern numbers or is quantized. The reason for this is that magnons are bosons and do not have Fermi surfaces. Therefore, in magnon systems, the

Chern number should be understood simply as a quantity that counts the number of edge states.

The thermal Hall effect of magnons has been observed for the first time in a pyrochlore ferromagnet  $\text{Lu}_2\text{V}_2\text{O}_7$  [99], which is understood as a 3D stack of the proposed one [98]. In the experiment, the thermal Hall conductivity perpendicular to the temperature gradient was measured for different signs and magnitudes of the magnetic field, which is shown in Fig. 2.4. The possibility that the contribution is due to electrons or phonons is excluded by considering the dependence on the magnetic field and temperature. The thermal Hall effect of magnons in a kagome ferromagnet as is the first proposal was later experimentally observed in the magnet  $\text{Cu}(1-3, \text{ bdc})$  [113].

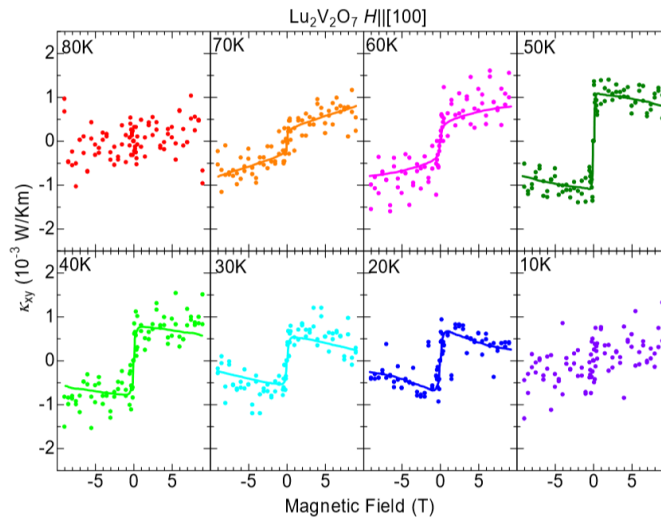


Fig. 2.4: The thermal Hall conductivity of  $\text{Lu}_2\text{V}_2\text{O}_7$  measured at various temperatures and applied magnetic fields, which is considered to be the contribution of magnons. The magnon thermal Hall effect is unclear at too low temperature and at high temperature since there are few excited magnons and since thermal fluctuation is large, respectively. We can see the magnetic field dependence of the thermal Hall coefficient most clearly at the temperature around 50 K. This figure is taken from Ref. [99].

## 2.4 Transverse current of magnons as a nonlinear response

While most of topological properties of magnons are studied in the linear response regime, the transverse current of magnons, i.e., magnon current perpendicular to the magnetic-field gradient, is studied in the nonlinear response regime [122]. Following the discussion of the nonlinear Hall effect of electrons in Ref. [39], the magnon current perpendicular to the magnetic-field gradient  $\nabla B_z$  is associated with the Berry curvature dipole of magnons. The magnetization current conveyed by magnons as a second-order response to  $\nabla B_z$  is

given by

$$J_{\text{NL},\alpha} = \chi_{\alpha\beta\gamma}(\partial_\beta B_z)(\partial_\gamma B_z), \quad (2.27)$$

where  $\chi_{\alpha\beta\gamma} = \epsilon_{\alpha\beta\gamma}(g\mu_B)^3\tau D_{\beta\delta}/\hbar^2$ . Here,  $g$ ,  $\mu_B$ , and  $\tau$ , are the  $g$ -factor of constituent spins, Bohr magneton, and the relaxation time of magnons, respectively. In the case that the spins are aligned in the  $+z$ -direction, the Berry curvature dipole tensor of magnons  $D_{\alpha\beta}$  is defined as follows:

$$D_{\alpha\beta} = \frac{1}{V} \sum_{n,\mathbf{k}} \frac{\partial \Omega_n^\beta(\mathbf{k})}{\partial k_\alpha} \rho_0(\epsilon_n(\mathbf{k})), \quad (2.28)$$

where  $V$  is the volume of the systems. As shown in Fig. 2.5, the Berry curvature dipole of magnons is calculated in the honeycomb lattice ferrimagnet, in which the spins on the two sublattices are ordered in the same direction but have the different magnitudes.

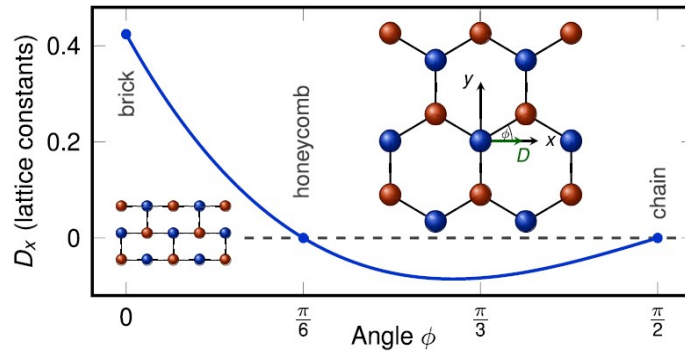


Fig. 2.5: The Berry curvature dipole  $D_x$  in the honeycomb lattice ferrimagnet. It is calculated as a function of the angle  $\phi$  between one of the nearest-neighbor bonds and the  $x$ -axis. This figure is taken from Ref. [122].

## 2.5 Spin Nernst effect of magnons

Similarly to the spin Hall effect for electrons, the spin Nernst effect of magnons is also realized by combining the magnon thermal Hall systems with spin dipole moments in opposite directions to each other. In the honeycomb lattice antiferromagnets with the DM interaction, it is shown that magnons flow perpendicular to the temperature gradient, and these directions are opposite between the magnon states with the magnetic moments upward and downward [120]. These transverse magnon currents result in a pure spin current without heat flow, which is the spin Nernst effect of magnons. The honeycomb lattice antiferromagnet exhibiting spin Nernst effect of magnons is shown in Fig. 2.6. The spins on the sublattices A and B are aligned upward and downward, respectively.

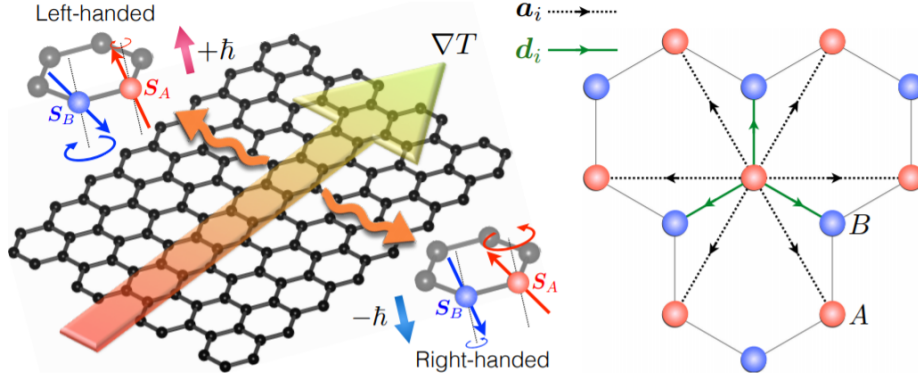


Fig. 2.6: The left panel shows the schematic picture of the magnon spin Nernst effect. Antiferromagnetic Heisenberg interaction between the nearest-neighbor spins results in the Néel order, in which spins on the sublattice A (B) point in the  $+z$  ( $-z$ )-direction. Due to the DM interaction, magnon states with the magnetic moments upward, i.e.,  $+\hbar$  (downward, i.e.,  $-\hbar$ ) flow leftward (rightward). As in the case of spin Hall effect of electrons, they result in the pure spin current. This figure is taken from Ref. [120]. The right panel shows the lattice vector  $\mathbf{a}_i$  and the vector between the nearest-neighbor sites  $\mathbf{d}_i$  ( $i = 1, 2, 3$ ).

The Hamiltonian of the model is written as follows:

$$H = J_1 \sum_{\langle ij \rangle} \mathbf{S}_i \cdot \mathbf{S}_j + D_2 \sum_{\langle\langle ij \rangle\rangle} \boldsymbol{\xi}_{ij} \cdot (\mathbf{S}_i \times \mathbf{S}_j) + \mathcal{K} \sum_i (S_i^z)^2, \quad (2.29)$$

where  $J_1$  and  $D_2$  are the coupling constant of the antiferromagnetic Heisenberg interaction ( $J_1 > 0$ ) and the DM interaction, respectively. The summations of the first and the second terms are taken over the nearest and the next nearest-neighbor couplings, respectively. The vector  $\boldsymbol{\xi}_{ij}$  is defined as  $\boldsymbol{\xi}_{ij} = 2\sqrt{3}\mathbf{d}_i \times \mathbf{d}_j$ , where  $\mathbf{d}_{i(j)}$  is a vector pointing from the lattice site between the sites  $i$  and  $j$  to the site  $i(j)$ . The third term is an easy-axis anisotropy and satisfies  $\mathcal{K} < 0$ .

By applying Holstein-Primakoff and Fourier transformations, we can obtain the BdG Hamiltonian of magnons as follows:

$$H = \sum_{\mathbf{k}} \boldsymbol{\psi}^\dagger(\mathbf{k}) H(\mathbf{k}) \boldsymbol{\psi}(\mathbf{k}), \quad (2.30)$$

where  $\boldsymbol{\psi}^\dagger(\mathbf{k}) = [a_{\mathbf{k}}^\dagger, b_{\mathbf{k}}^\dagger, a_{-\mathbf{k}}, b_{-\mathbf{k}}]$ . The operator  $a_{\mathbf{k}}$  ( $b_{\mathbf{k}}$ ) annihilates magnons with the wave vector  $\mathbf{k}$ , which are excited from spins on the sublattice A (B). The matrix  $H(\mathbf{k})$  is given by

$$H(\mathbf{k}) = S \begin{pmatrix} d + D_2 g(\mathbf{k}) & 0 & 0 & J_1 f(\mathbf{k}) \\ 0 & d - D_2 g(\mathbf{k}) & J_1 f^*(\mathbf{k}) & 0 \\ 0 & J_1 f(\mathbf{k}) & d - D_2 g(\mathbf{k}) & 0 \\ J_1 f^*(\mathbf{k}) & 0 & 0 & d + D_2 g(\mathbf{k}) \end{pmatrix}, \quad (2.31)$$

where  $d = 3J_1 - 2\mathcal{K}$ ,  $f(\mathbf{k}) = \sum_i e^{i\mathbf{k}\cdot\mathbf{d}_i}$ . The function  $g(\mathbf{k})$  is defined as

$$g(\mathbf{k}) = \sum_i 2 \sin(\mathbf{k} \cdot \mathbf{a}_i), \quad (2.32)$$

where  $\mathbf{a}_i$  ( $i = 1, 2$ ) are the lattice vectors (see Fig. 2.6). As in the present system, in collinear antiferromagnets that contain only the interactions such as Heisenberg and DM interactions, the  $z$ -component of the total spins  $S^z$  is conserved since they preserve the symmetry of the rotation around the  $z$ -axis. In such a case, the magnon eigenstates are separated into two parts which are magnon states with magnetic moment upward and downward. When we write the magnon vacuum as  $|0\rangle$ , magnon states with magnetic moment upward (downward) are described as linear superpositions of the states written as  $a_{\mathbf{k}}|0\rangle$  and  $b_{-\mathbf{k}}^\dagger|0\rangle$  ( $b_{\mathbf{k}}|0\rangle$  and  $a_{-\mathbf{k}}^\dagger|0\rangle$ ). This state can be thought of as an electron with an upward (downward) spin and a momentum  $\mathbf{k}$ .

The DM interaction gives the Berry curvature with opposite signs to magnons states having the magnetic moments upward and downward as the spin Hall effect does for electronic systems. The magnon spin Nernst current, which is carried by the magnon states with the magnetic moments upward and downward moving in opposite directions, is evaluated in linear response theory. It is written as follows:

$$J_y^S = \frac{\nabla T}{V} \int_{\text{BZ}} d^2k c_1(\rho_0(\epsilon(\mathbf{k}))) (\Omega_{\uparrow}(\mathbf{k}) - \Omega_{\downarrow}(\mathbf{k})). \quad (2.33)$$

Here,  $\Omega_{\uparrow(\downarrow)}(\mathbf{k})$  is the Berry curvature of magnons with the magnetic moment upward (downward), respectively. We assume that the temperature is written as  $T(\mathbf{r}) = T_0 + x\nabla T$ , where  $\nabla T$  is a constant for the temperature gradient. The function  $c_1(\rho_0)$  is defined as  $c_1(\rho_0) := (1 + \rho_0)\ln(1 + \rho_0) - \rho_0\ln\rho_0$ .

A spin current perpendicular to the temperature gradient, which is considered to be generated by a mechanism similar to the theoretical proposal, has been observed in an antiferromagnet MnPS<sub>3</sub> with a stacked honeycomb lattice [124]. Since couplings between the honeycomb layers of MnPS<sub>3</sub> is small, the system is regarded as a stacking of independent 2D magnets, and is close to the one proposed in the theoretical study. The spin current flowing in the direction perpendicular to the temperature gradient can be converted into an electric current due to the inverse spin Hall effect by injecting it into the Pt terminal [see Fig. 2.7].

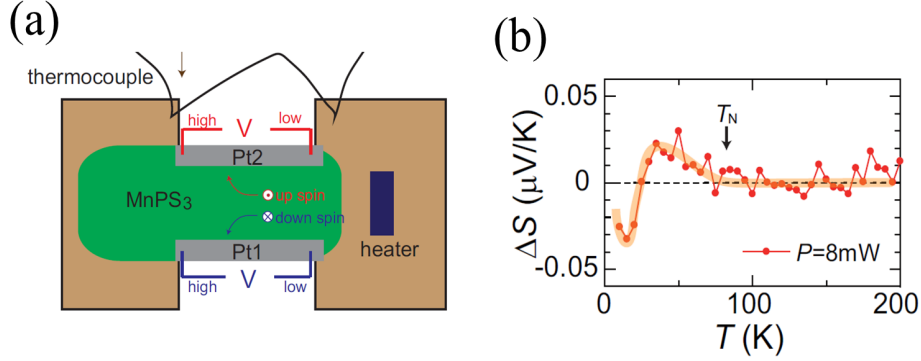


Fig. 2.7: (a) Experimental setups for observing the magnon spin Nernst effect in MnPS<sub>3</sub>. (b) Difference between the electric voltage of the two Pt terminals Pt1 and Pt2. As a signal of the spin current generated in the direction perpendicular to the temperature gradient, the difference is clearly observed at the temperature below  $T_N = 80$  K, which is the antiferromagnetic ordering temperature. These figures are taken from Ref. [124].

## 2.6 Magnonic analogs of quantum spin Hall insulators

Since the honeycomb lattice antiferromagnet in the previous section has only one magnon band, there is no helical edge state of magnons, and the spin Nernst effect of magnons is contributed by the magnons in the bulk.

On the other hand, magnonic systems having helical edge states, which are analogous to quantum spin Hall insulators of electrons discussed in Sec. 1.1.3, have also been proposed theoretically [121, 123]. The first model is constructed as an antiferromagnetically coupled two layers of the honeycomb lattice. The spin configuration of this model and the magnon band structure are shown in Fig. 2.8(a) and (b), respectively. A helical edge state can be seen in the bulk band gap.

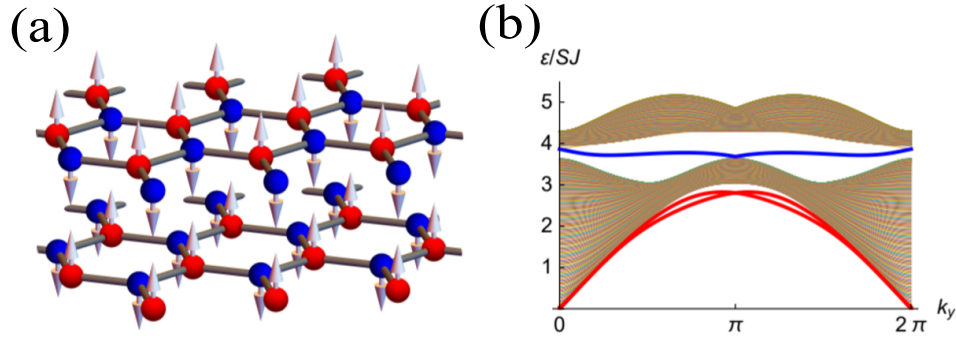


Fig. 2.8: (a) Bilayer honeycomb lattice antiferromagnet with a staggered magnetization. Spins on the nearest-neighbor sites and layers are aligned in the opposite directions to each other. (b) Magnon band structure. Helical edge states which are topologically nontrivial are shown in blue. The red lines are the edge states which are not related to the topology of the magnon bands. The figures are taken from Ref. [121].

The Hamiltonian of this model is given by

$$H = J_1 \sum_{\langle i,j \rangle, l} \mathbf{S}_i^{(l)} \cdot \mathbf{S}_j^{(l)} + D_2 \sum_{\langle\langle i,j \rangle\rangle, l} \boldsymbol{\xi}_{ij} \cdot (\mathbf{S}_i^{(l)} \times \mathbf{S}_j^{(l)}) + \mathcal{K} \sum_i (\mathbf{e}_z \cdot \mathbf{S}_i^{(l)})^2 + J' \sum_i \mathbf{S}_i^{(1)} \cdot \mathbf{S}_i^{(2)}, \quad (2.34)$$

where the index  $l = 1, 2$  denotes the first and second layers. Here,  $\mathbf{S}_i^{(l)}$  is the operator of the spin at site  $i$  on the  $l$ th layer. The first term is the intralayer antiferromagnetic Heisenberg interaction between the nearest-neighbor spins. The second term is the intralayer DM interaction between the next-nearest-neighbor spins. The remaining terms are the easy-axis anisotropy and the interlayer antiferromagnetic Heisenberg interaction, respectively. By applying Holstein-Primakoff and Fourier transformations, the Hamiltonian can be written as follows:

$$H = \sum_{\mathbf{k}} \boldsymbol{\psi}^\dagger(\mathbf{k}) H(\mathbf{k}) \boldsymbol{\psi}(\mathbf{k}), \quad (2.35)$$

where  $\boldsymbol{\psi}^\dagger = [a_1^\dagger(\mathbf{k}), b_2^\dagger(\mathbf{k}), a_2^\dagger(\mathbf{k}), b_1^\dagger(\mathbf{k}), a_1(-\mathbf{k}), b_2(-\mathbf{k}), a_2(-\mathbf{k}), b_1(-\mathbf{k})]$ . Here,  $a_{1(2)}(\mathbf{k})$  and  $b_{1(2)}(\mathbf{k})$  annihilate magnons with the wave vector  $\mathbf{k}$  which are excited from spins on the A and B sublattices on the first (second) layer. The matrix  $H(\mathbf{k})$  is given by

$$H(\mathbf{k}) = \begin{pmatrix} h_1(\mathbf{k}) & 0 & 0 & \Delta_1(\mathbf{k}) \\ 0 & h_1^*(-\mathbf{k}) & \Delta_1^*(-\mathbf{k}) & 0 \\ 0 & \Delta_1^*(-\mathbf{k}) & h_1^*(-\mathbf{k}) & 0 \\ \Delta_1(\mathbf{k}) & 0 & 0 & h_1(\mathbf{k}) \end{pmatrix}, \quad (2.36)$$

where

$$h_1(\mathbf{k}) = S \begin{pmatrix} 3J + J' - 2\mathcal{K} + D_2g(\mathbf{k}) & 0 \\ 0 & 3J + J' - 2\mathcal{K} - D_2g(\mathbf{k}) \end{pmatrix}, \quad (2.37)$$

$$\Delta_1(\mathbf{k}) = S \begin{pmatrix} J' & Jf(\mathbf{k}) \\ Jf^*(\mathbf{k}) & J' \end{pmatrix}. \quad (2.38)$$

Here, the function  $g(\mathbf{k})$  is defined in Eq. (2.32).

In electronic spin Hall insulators, the Kramers theorem plays an important role in the robustness of the helical edge states. Kramers theorem is applicable only when the time-reversal operator satisfies  $\Theta^2 = -1$  as in the case of electrons. However, since magnons are bosons, Kramers theorem is not directly applicable since the time-reversal operator satisfies  $\Theta^2 = +1$ . In the above system, the time-reversal operator is defined as  $\Theta = 1_2 \otimes \sigma_x \otimes 1_2K$  with  $\Theta^2 = +1$ , which exchanges magnons from spins upward and downward. Here,  $1_2$  and  $K$  are the  $2 \times 2$  unit matrix and the complex conjugate operator, respectively. With this  $\Theta$ , the Hamiltonian  $H(\mathbf{k})$  satisfies  $\Theta^{-1}H(\mathbf{k})\Theta = H(-\mathbf{k})$ . In the case where Kramers theorem does not hold, it is expected that the hybridization of the edge states occurs at the band crossing point, opening the gap and causing the helical edge state to disappear. Despite this, magnon helical edge states appear in the band structure in Fig. 2.8. This is due to the conservation of the  $z$ -component of spins in this model. In spin-conserving systems, the magnon states with upward and downward magnetic moments are separated from each other, so there is no hybridization at the band crossing point to open the gap. The fact that magnon states with upward and downward magnetic moments can exist as separated and degenerate states in systems with spin conservation suggests that it has a different symmetry other than  $\Theta$ . In fact, when a model satisfying the time-reversal symmetry conserves the  $z$ -component of spins, it simultaneously has a symmetry of the operator  $\Theta' = \sigma_z \otimes i\sigma_y \otimes 1_2K$  with  $\Theta'^2 = -1$  satisfies  $\Theta'^{-1}H(\mathbf{k})\Theta' = H(-\mathbf{k})$ . The operator  $\Theta'$  is called pseudo-time-reversal operator [142]. As shown in Appendix C, Kramers theorem can also be applied to the bosonic systems as long as they have pseudo-time-reversal symmetry. Thus, the symmetry of  $\Theta'$  leads to Kramers pairs of magnons.

The topological phases under the symmetry of  $\Theta'$  are studied in our paper Ref. [142] and summarized in our review [188]. Here, let us compare the form of a Hamiltonian with time-reversal symmetry and that of a Hamiltonian with pseudo-time-reversal symmetry. The generic Hamiltonian satisfying time-reversal symmetry  $\Theta^{-1}H(\mathbf{k})\Theta = H(-\mathbf{k})$  can be written as follows: Let us define the generic Hamiltonian  $H(\mathbf{k})$  satisfying time-reversal symmetry  $\Theta^{-1}H(\mathbf{k})\Theta = H(-\mathbf{k})$  as a  $4N \times 4N$  matrix, where  $N = 2$  for the case of Eq. (2.38). This is given in the following expression:

$$H(\mathbf{k}) = \begin{pmatrix} \bar{h}_1(\mathbf{k}) & \bar{h}_2(\mathbf{k}) & \bar{\Delta}_2(\mathbf{k}) & \bar{\Delta}_1(\mathbf{k}) \\ \bar{h}_2^\dagger(\mathbf{k}) & \bar{h}_1^*(-\mathbf{k}) & \bar{\Delta}_1^*(-\mathbf{k}) & \bar{\Delta}_2^\dagger(\mathbf{k}) \\ \bar{\Delta}_2^\dagger(\mathbf{k}) & \bar{\Delta}_1^*(-\mathbf{k}) & \bar{h}_1^*(-\mathbf{k}) & \bar{h}_2^*(-\mathbf{k}) \\ \bar{\Delta}_1(\mathbf{k}) & \bar{\Delta}_2(\mathbf{k}) & \bar{h}_2^T(-\mathbf{k}) & \bar{h}_1(\mathbf{k}) \end{pmatrix}, \quad (2.39)$$

where  $\bar{h}_i(\mathbf{k})$  and  $\bar{\Delta}_i(\mathbf{k})$  for  $i = 1, 2$  are  $N \times N$  matrices and satisfy  $\bar{h}_1^\dagger(\mathbf{k}) = \bar{h}_1(\mathbf{k})$ ,  $\bar{\Delta}_1^\dagger(\mathbf{k}) = \bar{\Delta}_1(\mathbf{k})$ ,  $\bar{h}_2^T(\mathbf{k}) = \bar{h}_2(-\mathbf{k})$ , and  $\bar{\Delta}_2^T(\mathbf{k}) = \bar{\Delta}_2(-\mathbf{k})$ . Here,  $N$  is the number of the degrees of freedom. On the other hand, the one satisfying pseudo-time-reversal symmetry  $\Theta'^{-1}H(\mathbf{k})\Theta' = H(-\mathbf{k})$  is given by

$$H(\mathbf{k}) = \begin{pmatrix} h_1(\mathbf{k}) & h_2(\mathbf{k}) & \Delta_2(\mathbf{k}) & \Delta_1(\mathbf{k}) \\ h_2^\dagger(\mathbf{k}) & h_1^*(-\mathbf{k}) & \Delta_1^*(-\mathbf{k}) & -\Delta_2^\dagger(\mathbf{k}) \\ \Delta_2^\dagger(\mathbf{k}) & \Delta_1^*(-\mathbf{k}) & h_1^*(-\mathbf{k}) & h_2^*(-\mathbf{k}) \\ \Delta_1(\mathbf{k}) & -\Delta_2(\mathbf{k}) & h_2^T(-\mathbf{k}) & h_1(\mathbf{k}) \end{pmatrix}, \quad (2.40)$$

where  $h_i(\mathbf{k})$  and  $\Delta_i(\mathbf{k})$  for  $i = 1, 2$  are  $N \times N$  matrices and satisfy  $h_1^\dagger(\mathbf{k}) = h_1(\mathbf{k})$ ,  $\Delta_1^\dagger(\mathbf{k}) = \Delta_1(\mathbf{k})$ ,  $h_2^T(\mathbf{k}) = -h_2(-\mathbf{k})$ , and  $\Delta_2^T(\mathbf{k}) = \Delta_2(-\mathbf{k})$ . We can see that these forms are the same when the system conserves spins, i.e.,  $h_2(\mathbf{k}) = \bar{h}_2(\mathbf{k}) = \Delta_2(\mathbf{k}) = \bar{\Delta}_2(\mathbf{k}) = 0$ .

When the system breaks the spin conservation, the time-reversal symmetry and the pseudo-time-reversal symmetry do not coincide, and the helical edge state cannot exist unless the latter is satisfied. The first model of a magnonic analog of quantum spin Hall insulators without spin conservation was proposed in Ref. [142]. The model includes the XYZ anisotropy, which breaks the spin conservation but does not break pseudo-time-reversal symmetry. The Hamiltonian for this system can be written as follows:

$$H_H = H_{\text{XYZ}}^{(1)} + H_{\text{XYZ}}^{(2)} + H_{\text{DM}}^{(1)} + H_{\text{DM}}^{(2)} + H^{(\text{inter})}, \quad (2.41)$$

$$H_{\text{XYZ}}^{(l)} = \sum_{\langle i,j \rangle} J_x^{(l)} S_{i,x}^{(l)} S_{j,x}^{(l)} + J_y^{(l)} S_{i,y}^{(l)} S_{j,y}^{(l)} + J_z^{(l)} S_{i,z}^{(l)} S_{j,z}^{(l)}, \quad (2.42)$$

$$H_{\text{DM}}^{(l)} = D \sum_{\langle\langle i,j \rangle\rangle} \xi_{ij} (\mathbf{S}_i^{(l)} \times \mathbf{S}_j^{(l)})_z, \quad (2.43)$$

$$H^{(\text{inter})} = J' \sum_i \mathbf{S}_i^{(1)} \cdot \mathbf{S}_i^{(2)}, \quad (2.44)$$

where  $S_{i,a}^{(l)}$  ( $a = x, y, z$ ) is the  $a$ -component of the spin at site  $i$  on the  $l$ th layer and  $J_z^{(1)} = J_z^{(2)}$ .

To make the pseudo-time-reversal symmetry satisfied,  $J_x^{(l)}$  and  $J_y^{(l)}$  in the top and bottom layers ( $l = 1$  and  $2$ ) should be tuned to be  $J_x^{(1)} = J_y^{(2)}$  and  $J_y^{(1)} = J_x^{(2)}$ .<sup>1</sup> The band structure of magnons is shown in Fig. 2.9. We can see that the helical edge state of magnons is not gapped out by the XYZ anisotropy as long as it respects the pseudo-time-reversal symmetry.

---

<sup>1</sup>As seen from this, models for the magnonic analogs of quantum spin Hall insulators which break spin conservation are artificial in many cases.

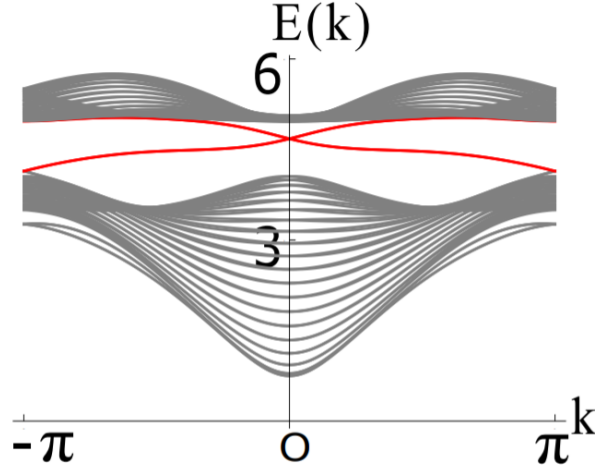


Fig. 2.9: Magnon band structure of the magnonic analog of quantum spin Hall insulators with the Hamiltonian in Eq. (2.41). The helical edge is shown in red. This figure is taken from Ref. [142].

In general,  $\mathbb{Z}_2$  topological invariant for magnonic analogs of quantum spin Hall insulators which are symmetric under  $\Theta'$  is defined in the following. Here we focus on the non-negative eigenvalues of  $\Sigma_z H(\mathbf{k})$ , and it is enough since the topological invariants are the same in the non-positive eigenvalues as discussed later. Since the systems satisfying  $\Theta'$ -symmetry are assumed to have the same number of spins pointing upward and downward, the number of degrees of freedom of magnons  $\mathcal{N}$  is even. As shown in Appendix C, there are always two different eigenstates  $\Psi_{n,1,+}(\mathbf{k})$  and  $\Psi_{n,2,+}(\mathbf{k})$  ( $n = 1, \dots, \mathcal{N}/2$ ) with the eigenvalues  $E_n(\mathbf{k})$  and  $E_n(-\mathbf{k})$ , respectively. They satisfy  $\Psi_{n,2,+}(\mathbf{k}) = -\Theta' \Psi_{n,1,+}(-\mathbf{k})$  and form the  $n$ th Kramers pair. Next, we consider the eigenvectors of  $\Sigma_z H(\mathbf{k})$  with the non-positive eigenvalues, i.e., hole bands. As discussed in Appendix A, the particle-hole conjugates  $\Psi_{n,l,-}(\mathbf{k}) = \Sigma_x K \Psi_{n,l,+}(-\mathbf{k})$ , ( $l = 1, 2$ ) are the eigenvectors of  $\Sigma_z H(\mathbf{k})$  with the eigenvalue  $-E_n((-1)^l \mathbf{k})$ . These eigenvectors satisfy the relations  $\langle\langle \Psi_{n,l,\sigma}(\mathbf{k}), \Psi_{m,l',\sigma'}(\mathbf{k}) \rangle\rangle = \sigma \delta_{n,m} \delta_{l,l'} \delta_{\sigma,\sigma'}$  ( $\sigma = \pm$ ) due to the para-unitarity of the matrix diagonalizing  $\Sigma_z H(\mathbf{k})$ , where the inner product is defined in Eq. (2.23).

The Berry connection and curvature of the eigenstates  $\Psi_{n,l,\sigma}(\mathbf{k})$  are defined as follows:

$$\mathbf{A}_{n,l,\sigma}(\mathbf{k}) = i \sigma \langle\langle \Psi_{n,l,\sigma}(\mathbf{k}), \nabla_{\mathbf{k}} \Psi_{n,l,\sigma}(\mathbf{k}) \rangle\rangle, \quad (2.45)$$

$$\mathbf{\Omega}_{n,l,\sigma}(\mathbf{k}) = \nabla_{\mathbf{k}} \times \mathbf{A}_{n,l,\sigma}(\mathbf{k}). \quad (2.46)$$

Let us take the summation over  $l = 1, 2$  and define the Berry connection and curvature of the  $n$ th Kramers pair as

$$\mathbf{A}_{n,\sigma}(\mathbf{k}) = \sum_{l=1,2} \mathbf{A}_{n,l,\sigma}(\mathbf{k}), \quad (2.47)$$

$$\mathbf{\Omega}_{n,\sigma}(\mathbf{k}) = \sum_{l=1,2} \mathbf{\Omega}_{n,l,\sigma}(\mathbf{k}). \quad (2.48)$$

Here,  $\Psi_{n,2,+}(\mathbf{k}) = -\Theta' \Psi_{n,1,+}(-\mathbf{k})$  and  $\Psi_{n,l,-}(\mathbf{k}) = \Sigma_x K \Psi_{n,l,+}(-\mathbf{k})$  result in the relations of the Berry connections written as  $\mathbf{A}_{n,1,+}(\mathbf{k}) = \mathbf{A}_{n,2,-}(\mathbf{k})$  and  $\mathbf{A}_{n,2,+}(\mathbf{k}) = \mathbf{A}_{n,1,-}(\mathbf{k})$ . They yield  $\mathbf{A}_{n,\sigma}(\mathbf{k}) = \mathbf{A}_{n,-\sigma}(\mathbf{k})$  and  $\Omega_{n,\sigma}(\mathbf{k}) = \Omega_{n,-\sigma}(\mathbf{k})$ .

By using the Berry connection and curvature of the  $n$ th Kramers pair,  $\mathbb{Z}_2$  topological invariant for magnonic analogs of quantum spin Hall insulators is defined as follows:

$$D_{n,\sigma} := \frac{1}{2\pi} \left[ \oint_{\partial\text{EBZ}} d\mathbf{k} \cdot \mathbf{A}_{n,\sigma}(\mathbf{k}) - \int_{\text{EBZ}} d^2k \Omega_{n,\sigma}^z(\mathbf{k}) \right] \text{ mod } 2, \quad (2.49)$$

where EBZ and  $\partial\text{EBZ}$  stand for the effective Brillouin zone and its boundary which are the same as those in Eq. (1.5), respectively. Due to  $\mathbf{A}_{n,\sigma}(\mathbf{k}) = \mathbf{A}_{n,-\sigma}(\mathbf{k})$  and  $\Omega_{n,\sigma}(\mathbf{k}) = \Omega_{n,-\sigma}(\mathbf{k})$ , the topological invariants of particles and holes are the same, i.e.,  $D_{n,\sigma} = D_{n,-\sigma}$ .



## Chapter 3

# Three-dimensional topological magnon systems

To extend magnonic analogs of quantum spin Hall insulators (2D topological insulators) to 3D, it is necessary to break the spin conservation. In realizing a  $\mathbb{Z}_2$  topological phase of magnons in such systems, pseudo-time-reversal symmetry discussed in Sec. 2.6 plays an important role. In this study, we propose for the first time a model for a magnonic analog of 3D topological insulators, which is discussed in Sec. 1.1.4 for electrons. The model is designed to satisfy pseudo-time-reversal symmetry. In these systems, the Dirac surface states of magnons protected by the pseudo-time-reversal symmetry appear. We explain the model on a diamond lattice in Sec. 3.1. The topological invariants and bulk-edge correspondence is discussed in Sec. 3.2. In Sec. 3.3, we show that the topological invariants can be much more simplified when the system has inversion symmetry. By using the simplified expressions of topological invariants, we construct a phase diagram of the proposed model in Sec. 3.4.

### 3.1 Model

Let us consider the first example of magnonic analogs of 3D topological insulators. We assume artificial spin systems in which two spins are localized at each site of the diamond lattice and pointing in the opposite directions to each other, as shown in Fig. 3.1. We consider the Hamiltonian of this system as follows:

$$H = H_{\text{DM}} + H_{J'} + H_J + H_{\text{XY}} + H_{\Gamma} + H_{\kappa}, \quad (3.1)$$

where the first term  $H_{\text{DM}}$  is the DM interaction acting between next-nearest-neighbor spins pointing in the same direction. In order to realize the spin configuration in which two spins on the same site are aligned in the opposite directions, we consider the second term  $H_{J'}$ , which is antiferromagnetic interaction between these two spins. The third term  $H_J$  is the bond-dependent ferromagnetic interaction between nearest-neighbor spins pointing in the same direction. The remaining term  $H_{\kappa}$  is the single-ion anisotropy. We note that in the magnon description, the Hamiltonian corresponding to the Fu-Kane-Mele model [16] is realized. After applying the Holstein-Primakoff transformation, the

interactions  $H_J$ ,  $H_{\text{DM}}$ ,  $H_{\Gamma}$ , and  $H_{\text{XY}}$  correspond to the hopping term  $t \sum_{\langle i,j \rangle} c_i^\dagger c_j$ , the  $z$ ,  $x$ , and  $y$ -components of the spin-orbit interaction  $i(8\lambda_{\text{SO}}/a^2) \sum_{\langle\langle i,j \rangle\rangle} c_i^\dagger \mathbf{s} \cdot (\mathbf{d}_{ij}^1 \times \mathbf{d}_{ij}^2) c_j$  in Eq. (1.18). The correspondence between the Hamiltonians of magnons considered here and those of electrons in Ref. [16] is summarized as follows:

$$H_J \leftrightarrow t \sum_{\langle i,j \rangle} c_i^\dagger c_j, \quad (3.2)$$

$$H_{\text{DM}} \leftrightarrow i(8\lambda_{\text{SO}}/a^2) \sum_{\langle\langle i,j \rangle\rangle} c_i^\dagger s_z (\mathbf{d}_{ij}^1 \times \mathbf{d}_{ij}^2)_z c_j, \quad (3.3)$$

$$H_{\Gamma} \leftrightarrow i(8\lambda_{\text{SO}}/a^2) \sum_{\langle\langle i,j \rangle\rangle} c_i^\dagger s_x (\mathbf{d}_{ij}^1 \times \mathbf{d}_{ij}^2)_x c_j, \quad (3.4)$$

$$H_{\text{XY}} \leftrightarrow i(8\lambda_{\text{SO}}/a^2) \sum_{\langle\langle i,j \rangle\rangle} c_i^\dagger s_y (\mathbf{d}_{ij}^1 \times \mathbf{d}_{ij}^2)_y c_j. \quad (3.5)$$

The remaining interactions  $H_{J'}$  and  $H_{\kappa}$  are considered to realize the spin configuration shown in Fig. 3.1 and do not have their counterparts in the Fu-Kane-Mele model [16]. It is confirmed that they do not change the topology of the band structure. The detailed expression of the Hamiltonian in terms of magnons obtained by applying the Holstein-Primakoff and Fourier transformations are discussed in Appendix D. In the absence of  $H_{\Gamma}$ , we can obtain the energy spectrum of the system analytically, which is discussed in Appendix E.

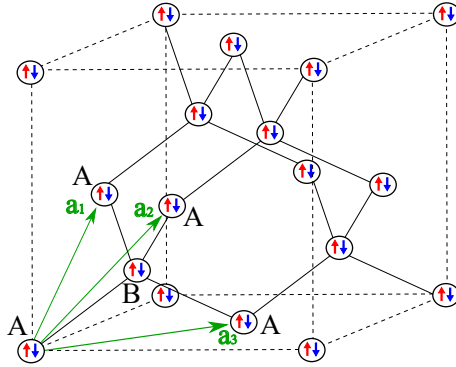


Fig. 3.1: Diamond lattice magnet having two spins at each site, which is proposed as the first model of magnonic analog of 3D topological insulators. We assume that the two spins at the same sites are aligned upward and downward. Two sublattices of the diamond lattice are denoted as A and B. The lattice prime vectors are shown by  $\mathbf{a}_i$  ( $i = 1, 2, 3$ ).

## 3.2 Topological invariants

By using the Berry connection Eq. (2.47) and curvature Eq. (2.48) for bosonic BdG systems, the topological invariants for 3D topological magnonic systems are defined as

follows:

$$\nu_{i,0}^{n\sigma} := \frac{1}{2\pi} \left[ \oint_{\partial\text{EBZ}_{i,0}} d\mathbf{k} \cdot [\mathbf{A}_{n\sigma}(\mathbf{k})]_{k_i=0} - \int_{\text{EBZ}_{i,0}} dk_j dk_k [\Omega_{n\sigma}^i(\mathbf{k})]_{k_i=0} \right] \text{ mod } 2, \quad (3.6)$$

$$\nu_{i,\pi}^{n\sigma} := \frac{1}{2\pi} \left[ \oint_{\partial\text{EBZ}_{i,\pi}} d\mathbf{k} \cdot [\mathbf{A}_{n\sigma}(\mathbf{k})]_{k_i=\pi} - \int_{\text{EBZ}_{i,\pi}} dk_j dk_k [\Omega_{n\sigma}^i(\mathbf{k})]_{k_i=\pi} \right] \text{ mod } 2. \quad (3.7)$$

Here,  $i$  ( $= x, y, z$ ) and  $n$  are the indices for the coordinates and the bands. The indices  $j$  and  $k$  represent two of  $x, y$ , and  $z$  which are different from  $i$ . The particle and hole space is designated by  $\sigma = +$  and  $\sigma = -$ , respectively. We define  $\text{EBZ}_{x,0}$  and others in the same way as the electronic systems in Eqs. (1.12) and (1.13). In this chapter, we calculated the topological invariants by using the numerical method of Ref. [19].

Since the values of the topological invariants of a particle and a hole are the same:  $\nu_{i,0}^{n+} = \nu_{i,0}^{n-}$ ,  $\nu_{i,\pi}^{n+} = \nu_{i,\pi}^{n-}$  as discussed in Sec. 2.6, we write  $\nu_{i,0(\pi)}^{n\pm} = \nu_{i,0(\pi)}^n$  in the following. To consider the bulk-boundary correspondence of magnons, we introduce the virtual ‘‘Fermi level’’  $\epsilon$ , and take the summation of topological invariants over the bands below  $\epsilon$ . This summation is confirmed to correspond to the number of the surface states, in the same way as that of electrons [16]. As we discussed for electron topological insulators in Sec. 1.1.4 four of the six topological indices  $\nu_{i,0(\pi)}$  are independent. Let us define a set of independent topological indices  $(\nu_0^n; \nu_x^n, \nu_y^n, \nu_z^n)$  as  $\nu_0^n = \nu_{x,0}^n + \nu_{x,\pi}^n$  and  $\nu_i^n = \nu_{i,\pi}^n$  ( $i = x, y, z$ ). We call the topological phase for  $\nu_0 = \sum_{n, (E_n(\mathbf{k}) \leq \epsilon)} \nu_0^n \pmod{2} = 1$  as the strong topological phase in the magnonic analogs of 3D topological insulators. On the other hand, the weak topological phase refers to that for  $\nu_0 = \sum_{n, (E_n(\mathbf{k}) \leq \epsilon)} \nu_0^n \pmod{2} = 0$  and at least one of  $\nu_i = \sum_{n, (E_n(\mathbf{k}) \leq \epsilon)} \nu_i^n \pmod{2}$  ( $i = x, y, z$ ) taking nonzero.

### 3.3 Simplified expressions for the topological invariants of the diamond lattice system

If a system has inversion symmetry, the expression of the topological invariants for topological insulators can be greatly simplified [83]. The same discussion can be applied to magnon systems. In this part, by using inversion symmetry, we analytically calculate the topological invariants for the diamond lattice system. The Hamiltonian (D.7) satisfies the following inversion symmetry:

$$R \Sigma_z H(\mathbf{k}) - \Sigma_z H(-\mathbf{k}) R = 0, \quad (3.8)$$

where  $R$  is an inversion operator defined as  $R := 1_2 \otimes 1_2 \otimes \sigma_x$ . Following the discussion in Ref. [83], topological invariants for 3D topological magnon systems with inversion symmetry can be written as

$$\begin{aligned} (-1)^{\nu_0} &= \prod_{n_1=0,1; n_2=0,1; n_3=0,1} \delta_{m=(n_1 n_2 n_3)}, \\ (-1)^{\nu_i} &= \prod_{n_i=1; n_{j \neq i}=0,1} \delta_{m=(n_1 n_2 n_3)}, \end{aligned} \quad (3.9)$$

where  $i = x, y$ , and  $z$ . Since  $\Sigma_z H(\mathbf{k})$  commutes with the inversion operator  $R$  at TRIM:  $\mathbf{\Gamma}_m = (\Gamma_m^x, \Gamma_m^y, \Gamma_m^z) = \pi(n_1, n_2, n_3)$ , an energy eigenvector  $\Psi_{n,1,+}(\mathbf{\Gamma}_m)$  can be chosen to be an eigenvector of  $R$ . Here, we write the eigenvalue of  $R$  as  $\xi_n(\mathbf{\Gamma}_m)$ . Then,  $\delta_{m=(n_1 n_2 n_3)}$  is defined as the product of  $\xi_n(\mathbf{\Gamma}_m)$  over the bands below the fictitious Fermi energy:

$$\delta_{m=(n_1 n_2 n_3)} = \prod_{n, E_n(\mathbf{k}) \leq \epsilon} \xi_n(\mathbf{\Gamma}_m) \quad (3.10)$$

Now, we assume that the fictitious Fermi energy lies between two bands in the particle space. In this case,  $\delta_{m=(n_1 n_2 n_3)}$  is an eigenvalue of  $R$  with eigenvector of the lower band  $\Psi_{2,1,+}(\mathbf{\Gamma}_m)$ . In the following, we obtain the expression of  $\Psi_{2,1,+}(\mathbf{\Gamma}_m)$ . The Hamiltonian of the diamond lattice system is written in the same form as Eq. (2.40) with  $N = 2$ . In particular, at the TRIM, the Hamiltonian of the diamond lattice system is written as

$$H(\mathbf{k}) = \begin{pmatrix} h_1(\mathbf{\Gamma}) & 0 & 0 & J'1_2 \\ 0 & h_1^*(\mathbf{\Gamma}) & J'1_2 & 0 \\ 0 & J'1_2 & h_1^*(\mathbf{\Gamma}) & 0 \\ J'1_2 & 0 & 0 & h_1(\mathbf{\Gamma}) \end{pmatrix}, \quad (3.11)$$

where  $J'$  is a coupling constant of the Heisenberg interaction between spins on the same site, as explained in Appendix D. The eigenvectors of the matrix  $h_1(\mathbf{\Gamma})$  are written as:

$$\phi_{\pm}(\mathbf{\Gamma}) = \frac{1}{\sqrt{2}} \begin{pmatrix} 1 \\ \mp \text{sgn}[\gamma(\mathbf{\Gamma})] \end{pmatrix}, \quad (3.12)$$

where the corresponding eigenvalues are  $\epsilon_{\pm}(\mathbf{\Gamma}) = d_0 \pm |d_1(\mathbf{\Gamma})|$ . Here,  $\gamma(\mathbf{k})$  is defined as  $\gamma(\mathbf{k}) = -d_1(\mathbf{k}) - id_2(\mathbf{k})$ . We note that the imaginary part of  $\gamma(\mathbf{k})$ , i.e.,  $d_2(\mathbf{k})$ , vanishes at TRIM. If we write the eigenvector of  $\Sigma_z H(\mathbf{\Gamma})$  as

$$\Phi_{\pm}(\mathbf{\Gamma}) = \begin{pmatrix} \alpha \phi_{\pm}(\mathbf{\Gamma}) \\ 0 \\ 0 \\ \beta \phi_{\pm}(\mathbf{\Gamma}) \end{pmatrix}, \quad (3.13)$$

the eigenvalue equation can be written as follows:

$$\begin{pmatrix} h_1(\mathbf{\Gamma}) & 0 & 0 & J'1_2 \\ 0 & h_1^*(\mathbf{\Gamma}) & J'1_2 & 0 \\ 0 & -J'1_2 & -h_1^*(\mathbf{\Gamma}) & 0 \\ -J'1_2 & 0 & 0 & -h_1(\mathbf{\Gamma}) \end{pmatrix} \begin{pmatrix} \alpha \phi_{\pm}(\mathbf{\Gamma}) \\ 0 \\ 0 \\ \beta \phi_{\pm}(\mathbf{\Gamma}) \end{pmatrix} = E_{\pm}(\mathbf{\Gamma}) \begin{pmatrix} \alpha \phi_{\pm}(\mathbf{\Gamma}) \\ 0 \\ 0 \\ \beta \phi_{\pm}(\mathbf{\Gamma}) \end{pmatrix}. \quad (3.14)$$

This results in the following relation:

$$\begin{pmatrix} \epsilon_{\pm}(\mathbf{\Gamma}) - E_{\pm}(\mathbf{\Gamma}) & J' \\ -J' & -\epsilon_{\pm}(\mathbf{\Gamma}) - E_{\pm}(\mathbf{\Gamma}) \end{pmatrix} \begin{pmatrix} \alpha \\ \beta \end{pmatrix} = \begin{pmatrix} 0 \\ 0 \end{pmatrix}. \quad (3.15)$$

In order for the equation to have a nontrivial solution, the determinant of the matrix on the left-hand side must be zero. Then, we obtain the following equation:

$$E_{\pm}^2(\mathbf{\Gamma}) - \epsilon_{\pm}^2(\mathbf{\Gamma}) + J'^2 = 0. \quad (3.16)$$

Therefore, we obtain the energy eigenvalues in the particle space:

$$E_{\pm}(\mathbf{\Gamma}) = \sqrt{\epsilon_{\pm}^2(\mathbf{\Gamma}) - J'^2}. \quad (3.17)$$

We can see that  $E_+(\mathbf{\Gamma})$  and  $E_-(\mathbf{\Gamma})$  correspond to the energies of the top and bottom bands, respectively. Now we focus on the bottom band. By using  $\theta(\mathbf{\Gamma})$  defined as

$$\tanh(\theta(\mathbf{\Gamma})) := \frac{E_-(\mathbf{\Gamma}) - \epsilon_-(\mathbf{\Gamma})}{J'}, \quad (3.18)$$

the coefficients  $\alpha$  and  $\beta$  of the normalized wave function of the bottom band are written as  $\alpha = \cosh(\theta(\mathbf{\Gamma}))$  and  $\beta = \sinh(\theta(\mathbf{\Gamma}))$ , respectively. Then, the eigenvector of the bottom band  $\Psi_{2,1,+}(\mathbf{\Gamma})$  is given by

$$\Psi_{2,1,+}(\mathbf{\Gamma}) = \begin{pmatrix} \cosh(\theta(\mathbf{\Gamma}))\phi_-(\mathbf{\Gamma}) \\ 0 \\ 0 \\ \sinh(\theta(\mathbf{\Gamma}))\phi_-(\mathbf{\Gamma}) \end{pmatrix}. \quad (3.19)$$

We can see that this is an eigenvector of  $R$  with eigenvalue  $\text{sgn}[\gamma(\mathbf{\Gamma})]$ . Then,  $\delta_{m=(n_1n_2n_3)}$  in Eq. (3.10) can be written as

$$\begin{aligned} \delta_{m=(n_1n_2n_3)} &= \text{sgn}[\gamma(\mathbf{\Gamma}_m)] \\ &= \text{sgn}[J_0 + J_1e^{i\Gamma_m^x} + J_2e^{i\Gamma_m^y} + J_3e^{i\Gamma_m^z}], \end{aligned} \quad (3.20)$$

where  $J_i$  ( $i = 0, \dots, 3$ ) is the coupling constant of the Heisenberg interaction between the spins on the nearest-neighbor sites. The details are shown in the Appendix D. By using this, the strong index for the diamond lattice system is given by

$$\begin{aligned} (-1)^{\nu_0} &= \text{sgn}[(J_0 - J_1 + J_2 + J_3)(J_0 - J_1 - J_2 + J_3)(J_0 - J_1 + J_2 - J_3)(J_0 - J_1 - J_2 - J_3)] \\ &\quad \times \text{sgn}[(J_0 + J_1 + J_2 + J_3)(J_0 + J_1 - J_2 + J_3)(J_0 + J_1 + J_2 - J_3)(J_0 + J_1 - J_2 - J_3)]. \end{aligned} \quad (3.21)$$

The other three indices are written as follows:

$$(-1)^{\nu_x} = \text{sgn}[(J_0 - J_1 + J_2 + J_3)(J_0 - J_1 - J_2 + J_3)(J_0 - J_1 + J_2 - J_3)(J_0 - J_1 - J_2 - J_3)], \quad (3.22)$$

$$(-1)^{\nu_y} = \text{sgn}[(J_0 + J_1 - J_2 + J_3)(J_0 - J_1 - J_2 + J_3)(J_0 + J_1 - J_2 - J_3)(J_0 - J_1 - J_2 - J_3)], \quad (3.23)$$

$$(-1)^{\nu_z} = \text{sgn}[(J_0 + J_1 + J_2 - J_3)(J_0 - J_1 + J_2 - J_3)(J_0 + J_1 - J_2 - J_3)(J_0 - J_1 - J_2 - J_3)]. \quad (3.24)$$

### 3.4 Phase diagram and band structure

We calculate the band structure of magnons of the model (3.1) along with the high symmetry points, as shown in Fig. 3.2(a). In this section, we classify the topological phases of the model, by calculating the topological invariants of the lower band in the particle space. We discuss the correspondence between the topological invariants and the number of the surface Dirac cones in the bulk band gap. By using the simplified formula for the topological invariants in Eqs. (3.21) to (3.24), we construct a phase diagram of the diamond lattice system as shown in Fig. 3.2(b). We can see that three phases: strong topological, weak topological, and trivial phases are all realized in the phase diagram. Figure 3.3 shows the band structure for a slab with (100) face of the system. We can discuss the bulk-boundary correspondence which is the same as that in electronic systems. Even number (2 and 0, respectively) of surface Dirac cones can be seen in weak topological phases (0;111) and (0;100) (Fig. 3.3(a) and (b), respectively). We can also find odd number (1 and 3, respectively) of surface Dirac cones in strong topological phases (1;111) and (1;100) (Fig. 3.3(c) and (d), respectively). Here, we note that the Dirac surface states of magnons which are first realized in this study exhibit interesting properties, such as the magnon spin-momentum locking [189–191], as in the case of those of electrons.

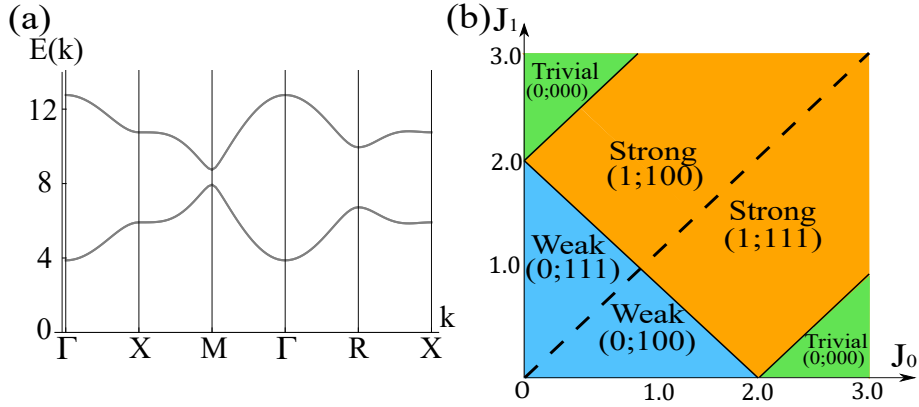


Fig. 3.2: (a) The bulk band structure of magnons in the diamond lattice system (3.1). For practical calculation, we consider the topologically equivalent deformed lattice, which is a cubic one, by taking  $\mathbf{a}_1 = (1, 0, 0)$ ,  $\mathbf{a}_2 = (0, 1, 0)$ , and  $\mathbf{a}_3 = (0, 0, 1)$ . We choose the parameters as  $J_0 = 1.4$ ,  $J_1 = J_2 = J_3 = J' = 1.0$ ,  $J_- = D = \Gamma = 0.3$ ,  $\kappa = 1.5$ . We write the high symmetry points as  $\Gamma = (0, 0, 0)$ ,  $X = (\pi, 0, 0)$ ,  $M = (\pi, 0, \pi)$ , and  $R = (\pi, \pi, \pi)$ . (b) The phase diagram of magnonic analog of 3D topological insulators in the diamond lattice system, which are constructed as a function of  $J_0$  and  $J_1$ . The topological indices for each phase are written as  $(\nu_0^2; \nu_x^2, \nu_y^2, \nu_z^2)$ . We choose the other parameters as  $J_2 = J_3 = J' = 1.0$ ,  $J_- = D = \Gamma = 0.3$ ,  $\kappa = 1.5$ . The phase boundary between two phases with different weak indices is plotted as the dashed line.

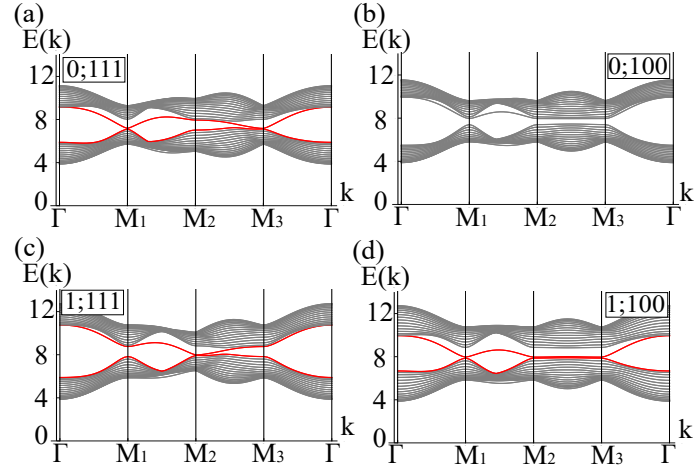


Fig. 3.3: The magnon band structure of the model (3.1) for a slab with (100) face for the four phases  $(\nu_0^2; \nu_x^2, \nu_y^2, \nu_z^2) = (0; 1, 1, 1)$ ,  $(0; 1, 0, 0)$ ,  $(1; 1, 1, 1)$ , and  $(1; 1, 0, 0)$  in Fig. 3.2(b). We show the topological Dirac surface states by red. The high symmetry points are written as  $\Gamma = (0, 0)$ ,  $M_1 = (\pi, 0)$ ,  $M_2 = (\pi, \pi)$ , and  $M_3 = (0, \pi)$ . We choose the coupling constants  $(J_0, J_1)$  to be (a)  $(J_0, J_1) = (0.6, 1.0)$ , (b)  $(J_0, J_1) = (1.0, 0.8)$ , (c)  $(J_0, J_1) = (1.4, 1.0)$ , and (d)  $(J_0, J_1) = (1.0, 1.4)$ , respectively. We take the other parameters to be the same as those in Fig. 3.2(b), i.e.,  $J_2 = J_3 = J' = 1.0$ ,  $J_- = D = \Gamma = 0.3$ ,  $\kappa = 1.5$ .



## Chapter 4

# Dirac surface states in magnonic analogs of topological crystalline insulators

The topological surface states of magnons considered in the previous chapter are unprecedented states in the magnetic systems. However, the realization of them is limited to quite artificial models. In this chapter, we point out that similar surface states of magnons can be realized in much more natural models. They are categorized in the magnonic analogs of topological crystalline insulators discussed in Sec. 1.1.5. In particular, the models which we consider here are the magnonic analogs of antiferromagnetic topological insulators (MAFTI) [38]. The essential point is that the symmetry of the combination of time-reversal ( $\Theta$ ) and a half translation ( $T_{1/2}$ ) allows for the Kramers pairs of magnons. In the following, we refer to the symmetry of the combination operator  $S_{1/2} = \Theta T_{1/2}$  as  $S$ -symmetry.

We also discuss the properties unique to the topological surface states of magnons. The particle with a magnetic moment obtains a vector potential dependent on its magnetic moment when moving in an electric field, which is called Aharonov-Casher (AC) effect [192]. In particular, AC effect is dominant for particles which do not have an electric charge but have a magnetic moment, such as magnons. Together with the spin-momentum locking in the surface states [189–191], the AC effect results in the realization of electric-field-driven current of magnons. We also find out the candidate material for MAFTI. We calculate the magnon band structure of a van der Waals magnet  $\text{CrI}_3$  with the monoclinic stacking and reveal the existence of the Dirac surface states topologically protected by  $S$ -symmetry.

In Secs. 4.1 and 4.2, we propose the model for MAFTI and discuss the induction of magnon current by an electric field, respectively. In Sec. 4.3, we study the model corresponding to a van der Waals magnet  $\text{CrI}_3$  and show the existence of magnon Dirac surface states. The phase diagrams for the models in Sec. 4.1 and  $\text{CrI}_3$  are constructed in Sec. 4.4.

### 4.1 Model

In this section, we propose the first models for MAFTI. It is a stack of honeycomb lattice magnets with intralayer ferromagnetic and interlayer antiferromagnetic interactions. The

system is shown in Fig. 4.1. The spins on the odd and even layers are aligned in  $+z$ - and  $-z$ -directions, respectively. The Hamiltonian is written as follows:

$$\mathcal{H} = - \sum_{\langle ij \rangle, l} \mathbf{S}_{i,l} J_{ij} \mathbf{S}_{j,l} + D \sum_{\langle\langle ij \rangle\rangle, l} \xi_{ij} (\mathbf{S}_{i,l} \times \mathbf{S}_{j,l})_z + J' \sum_{i, (l, l')} \mathbf{S}_{i,l} \cdot \mathbf{S}_{i, l'}. \quad (4.1)$$

Here, a pair of indices  $i$  and  $l$  denote the sites on honeycomb lattice and the layers, respectively. The vector  $\mathbf{S}_{i,l} := (S_{j,l}^x, S_{j,l}^y, S_{j,l}^z)$  is the operator of spins on the site designated by the indices  $i$  and  $l$ . The  $3 \times 3$  diagonal matrix  $J_{ij}$  is defined as  $J_{ij} := J_n = \text{diag}(J_n^x, J_n^y, J_n^z)$ , where  $n = 0, 1, 2$  correspond to the three different bonds in the honeycomb lattice as shown in Fig. 4.1. The second term is the DM interaction between the next-nearest-neighbor spins on the honeycomb layers. The sign convention  $\xi_{ij} = +1 (= -\xi_{ji})$  for  $i \rightarrow j$  is shown by orange arrows in Fig. 4.1. The third term represents antiferromagnetic interlayer couplings.

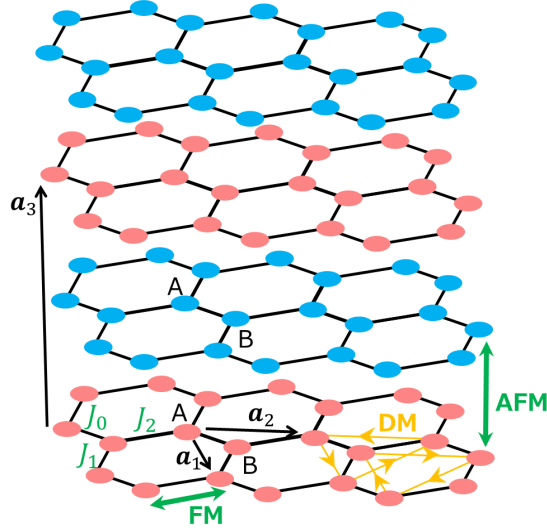


Fig. 4.1: The picture for the first model of MAFTI. Red and blue circles indicate spins aligned upward and downward, respectively. Spins on the same layer are ferromagnetically ordered. The stacked layers have alternating magnetization. The two sublattices of the honeycomb lattice is indicated by A and B. The matrices  $J_n$  ( $n = 0, 1, 2$ ) are the couplings of the Heisenberg interaction with XYZ anisotropy with the three different bonds. The lattice primitive vectors are denoted as  $\mathbf{a}_1$ ,  $\mathbf{a}_2$ , and  $\mathbf{a}_3$ .

Here, we apply Holstein-Primakoff and Fourier transformations and write down the Hamiltonian (4.1) as follows:

$$\mathcal{H} = \frac{1}{2} \sum_{\mathbf{k}} [\mathbf{b}^\dagger(\mathbf{k}) \mathbf{b}(-\mathbf{k})] H(\mathbf{k}) \begin{bmatrix} \mathbf{b}(\mathbf{k}) \\ \mathbf{b}^\dagger(-\mathbf{k}) \end{bmatrix}. \quad (4.2)$$

Here, when we define the annihilation operator of magnons at the sublattice A(B) on the layer with odd (even)  $l$  as  $b(\mathbf{k}, A(B), 1(2))$ , the operator  $\mathbf{b}(\mathbf{k})$  is written as  $\mathbf{b}(\mathbf{k}) =$

$(b(\mathbf{k}, A, 1), b(\mathbf{k}, B, 1), b(\mathbf{k}, A, 2), b(\mathbf{k}, B, 2))^T$ . The explicit expression for the matrix  $H(\mathbf{k})$  is given in Appendix F.

As we can expect from Fig. 4.1, the system is symmetric under the combination of time-reversal, which correspond to reversing the direction of spins, and the translation in the  $z$ -direction by one layer. They are defined as  $\Theta = K$  and  $T_{1/2}(k_z) = 1_2 \otimes \sigma_x \text{diag}(1, e^{ik_z}) \otimes 1_2$ , respectively. The symmetry of the system leads to  $S_{1/2}^{-1}(k_z)H(\mathbf{k})S_{1/2}(k_z) = H(-\mathbf{k})$ , where the operator  $S_{1/2}(k_z)$  is defined as  $S_{1/2}(k_z) = \Theta T_{1/2}(k_z)$ .

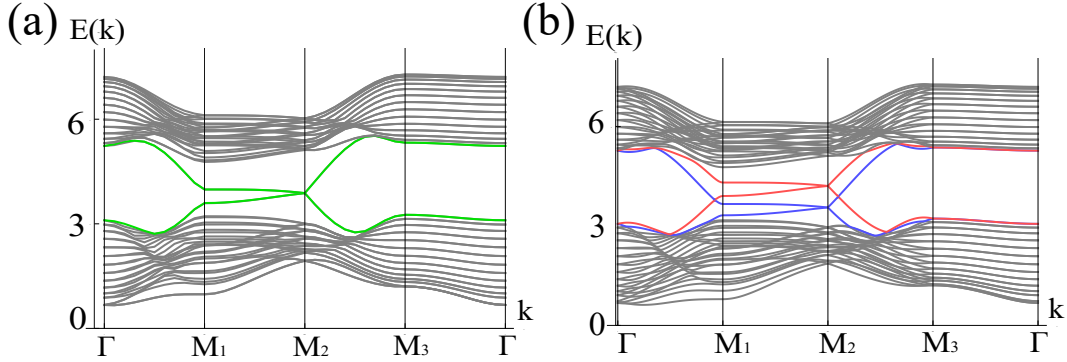


Fig. 4.2: Magnon energy dispersion of a slab with (100) face of the model (4.1) (a) without and (b) with an applied electric field. In (a), Dirac surface states are shown in green. In (b), the ones which shift upward and downward are shown in red and blue, respectively. When calculating the energy dispersions, the parameters are taken to be  $J_1^x = 1.6$ ,  $J_1^y = 0.4$ ,  $J_2^x = 1.0$ ,  $J_2^y = 1.0$ ,  $J_3^x = 0.4$ ,  $J_3^y = 1.6$ ,  $J_1^z = J_2^z = J_3^z = 1.1$ ,  $D = 0.2$ ,  $J' = 0.5$ , and  $S = 1.0$ . We note that for simplicity, the lattice is deformed into a topologically equivalent cubic-shaped lattice. The high symmetry points  $\Gamma$ ,  $M_1$ ,  $M_2$ , and  $M_3$  are defined as  $(k_2, k_3) = (0, 0)$ ,  $(\pi, 0)$ ,  $(\pi, \pi)$ , and  $(0, \pi)$ , respectively.

Since the operator  $S_{1/2}(k_z)$  satisfies  $S_{1/2}(-k_z)S_{1/2}(k_z) = e^{ik_z}$ , Kramers theorem can be applied at time-reversal invariant momenta in the  $k_z = \pi$  plane due to  $S_{1/2}(\pi)^2 = -1$ , which enables topological surface states to appear. The magnon band structure of a slab with (100) face is shown in Fig. 4.2(a). The single Dirac surface states similar to that in strong topological insulators in class AII, which we discussed in Sec. 1.1.4, can be found at  $(k_y, k_z) = (\pi, \pi)$  ( $M_2$  point). By replacing the pseudo-time-reversal operator  $\Theta'$  with  $S_{1/2}(\pi)$  in the definition of  $\nu_{z,\pi}^{n\sigma}$  in Ref. [144], we can define the  $\mathbb{Z}_2$  topological invariant of MAFTI as follows:

$$\nu_{z,\pi}^{n\sigma} := \frac{1}{2\pi} \left[ \oint_{\partial \text{EBZ}_{z,\pi}} d\mathbf{k} \cdot [\mathbf{A}_{n\sigma}(\mathbf{k})]_{k_z=\pi} - \int_{\text{EBZ}_{z,\pi}} dk_x dk_y [\Omega_{n\sigma}^z(\mathbf{k})]_{k_z=\pi} \right] \text{mod } 2. \quad (4.3)$$

Correspondence between the existence of the surface states and this topological invariant can be confirmed. By using this, we construct the phase diagram of the model (4.1) in Sec. 4.4.

## 4.2 Energy current induced by a homogeneous electric field

In this section, we discuss what occurs when we apply an electric field to MAFTI. As seen from Fig. 4.2(b), by applying an electric field, the Dirac dispersions of one and the other surfaces shift upward (red) and downward (blue), respectively. After discussing the mechanism for this in terms of the spin-momentum locking of the magnons [189–191], we show that this results in an energy current.

To understand the phenomena, let us consider the AC effect, in which magnons acquire a geometric phase by moving in an electric field  $\mathbf{E}$  [192]. Due to the AC effect, the hopping term of magnons is modified as

$$b_i^\dagger b_j + h.c. \rightarrow e^{i\phi_{ij}} b_i^\dagger b_j + h.c., \quad (4.4)$$

where  $b_i$  is an annihilation operator of magnons at site  $i$ . The AC phase  $\phi_{ij}$  is written as

$$\phi_{ij} = \frac{1}{c^2} \int_{\mathbf{r}_i}^{\mathbf{r}_j} d\mathbf{r} \cdot (\mathbf{E} \times \boldsymbol{\mu}). \quad (4.5)$$

Here,  $c$  and  $\mathbf{r}_{i(j)}$  are the speed of light in a vacuum and the position of the lattice site  $i(j)$ , respectively. The vector  $\boldsymbol{\mu} := -\sigma g \mu_B \mathbf{e}_z$  is the magnetic moment of magnons from up ( $\sigma = +$ ) or down ( $\sigma = -$ ) spins, where  $g$  is the  $g$ -factor of the spins,  $\mu_B$  is the Bohr magneton, and  $\mathbf{e}_\gamma$  ( $\gamma = x, y, z$ ) is the unit vector in the  $\gamma$ -direction. In the reciprocal space, the AC effect results in the shift of the wave vector as follows:

$$\mathbf{k} \rightarrow \mathbf{k} - \frac{\sigma g \mu_B}{c^2} \mathbf{E} \times \mathbf{e}_z. \quad (4.6)$$

How the vector potential in Eq. (4.6) results in the shift of surface Dirac dispersions as in Fig. 4.2(b) is explained as follows. The effective Hamiltonian for  $(\bar{1}00)$  and  $(100)$  surfaces are written as follows:

$$H_\pm(\bar{\mathbf{k}}) = \pm \begin{pmatrix} \alpha k_y + E_0 & \beta^* k_z \\ \beta k_z & -\alpha k_y + E_0 \end{pmatrix}, \quad (4.7)$$

where  $E_0$  and  $\bar{\mathbf{k}}$  are the energy of the center of the Dirac cone and  $\bar{\mathbf{k}} = (k_y, k_z)$ , respectively. The details of the derivation is shown in Appendix G. Here, the coefficients  $\alpha$  and  $\beta$  are calculated numerically as in Ref. [144]. The magnon state described by the wave function  $\boldsymbol{\psi} = (1, 0)^T$  and  $\boldsymbol{\psi}' = (0, 1)^T$  have the magnetic moment  $\boldsymbol{\mu} = -g \mu_B \mathbf{e}_z$  and  $\boldsymbol{\mu} = +g \mu_B \mathbf{e}_z$ , respectively. The direction of the magnetic moment and the momentum are locked, whose relationships are opposite between magnons described by  $H_+(\bar{\mathbf{k}})$  and  $H_-(\bar{\mathbf{k}})$ . Under a homogeneous electric field applied in the  $x$ -direction  $\mathbf{E} = E_x \mathbf{e}_x$ , due to the Peierls substitution in Eq. (4.6), the Hamiltonian  $H_\pm(\bar{\mathbf{k}})$  is changed as follows:

$$\begin{aligned} H_\pm(\bar{\mathbf{k}}) &\rightarrow \pm \begin{pmatrix} \alpha(k_y + \frac{g\mu_B}{c^2} E_x) + E_0 & \beta^* k_z \\ \beta k_z & -\alpha(k_y - \frac{g\mu_B}{c^2} E_x) + E_0 \end{pmatrix} \\ &= H_\pm(\bar{\mathbf{k}}) \pm \alpha \frac{g\mu_B}{c^2} E_x \hat{1}_2. \end{aligned} \quad (4.8)$$

From the above equation, we can understand the mechanism of the shift of Dirac surface states as in Fig. 4.2(b).

Next, we show that the shift of the Dirac surface states results in the energy current. The energy current operator is introduced as follows [103, 193]:

$$J_x = \sum_i \bar{P}_i \dot{h}_i. \quad (4.9)$$

Here, we write the operator of the position along the  $x$ -direction and the time derivative of the Hamiltonian density at the site  $i$  as  $\bar{P}_i$  and  $\dot{h}_i$ , respectively. By using the set of magnon annihilation and creation operators  $\psi(\bar{\mathbf{k}})$ ,  $J_x$  can be written as follows:

$$J_x = \frac{1}{2} \sum_{\bar{\mathbf{k}}} \psi^\dagger(\bar{\mathbf{k}}) J_x(\bar{\mathbf{k}}) \psi(\bar{\mathbf{k}}), \quad (4.10)$$

where the matrix  $J_x(\bar{\mathbf{k}})$  is given by

$$J_x(\bar{\mathbf{k}}) = -\frac{i}{2} (\bar{P} H(\bar{\mathbf{k}}) \Sigma_z H(\bar{\mathbf{k}}) - H(\bar{\mathbf{k}}) \Sigma_z H(\bar{\mathbf{k}}) \bar{P}). \quad (4.11)$$

Here,  $\bar{P}$  and  $H(\bar{\mathbf{k}})$  are the matrix for the operator of the position in the  $x$ -direction and the Hamiltonian for a slab geometry with open boundary conditions in the  $x$ -direction, respectively. By using  $4N \times 4N$  identity matrix  $1_{4N}$ , we define  $\Sigma_z$  as  $\Sigma_z = \sigma_z \otimes 1_{4N}$ , where  $N$  is the number of the unit cells in the  $x$ -direction parallel to the vector  $\mathbf{a}_1$ . We discuss the details of the energy current operator in Appendix H.

By using the linear response theory, we calculate the energy current induced by an applied electric field. We first consider the AC electric field  $E_x(t) = E_x e^{-i\omega t}$ . When the perturbation Hamiltonian of the first order in the electric field  $E_x$  is written as  $H_E$ , the expectation value of  $J_x$  is written as follows:

$$\langle J_x \rangle = -\frac{i}{\hbar} \int_0^\infty d\tau e^{i\omega\tau} \text{tr} [e^{-iH_0\tau/\hbar} [H_E, \rho_0] e^{iH_0\tau/\hbar} J_x] e^{-i\omega t}. \quad (4.12)$$

Here, the density operator for the unperturbed Hamiltonian  $H_0$  at thermal equilibrium is given as  $\rho_0$ . The details of the expression of  $H_E$  are given in Appendix I. In the following, Planck units are used; i.e., the Planck constant, the Boltzmann constant, and the speed of light are taken to be unity. Here, let us study the response to the DC electric field, and take the limit of  $\omega \rightarrow 0$ . The energy current Eq. (4.12) is written as follows:

$$\begin{aligned} \langle J_x \rangle &= i \sum_{\bar{\mathbf{k}}} \sum_{\alpha\beta\gamma\delta\zeta\eta} \frac{n_B(E_\alpha(\bar{\mathbf{k}})) - n_B(E_\delta(\bar{\mathbf{k}}))}{(E_\alpha(\bar{\mathbf{k}}) - E_\delta(\bar{\mathbf{k}}) + i/\tau_\ell)(E_\alpha(\bar{\mathbf{k}}) - E_\delta(\bar{\mathbf{k}}))} \\ &\quad \times T_{\alpha\beta}^{-1}(\bar{\mathbf{k}}) \left( \hat{J}_x(\bar{\mathbf{k}}) \right)_{\beta\gamma} T_{\gamma\delta}(\bar{\mathbf{k}}) T_{\delta\zeta}^{-1}(\bar{\mathbf{k}}) \left( \hat{H}_E(\bar{\mathbf{k}}) \right)_{\zeta\eta} T_{\eta\alpha}(\bar{\mathbf{k}}). \end{aligned} \quad (4.13)$$

Here, we define  $\hat{J}_x(\bar{\mathbf{k}})$  and  $\hat{H}_E(\bar{\mathbf{k}})$  as  $\hat{J}_x(\bar{\mathbf{k}}) = \Sigma_z J_x(\bar{\mathbf{k}})$  and  $\hat{H}_E(\bar{\mathbf{k}}) = i(\Sigma_z H(\bar{\mathbf{k}}) \Sigma_z H_E(\bar{\mathbf{k}}) - \Sigma_z H_E(\bar{\mathbf{k}}) \Sigma_z H(\bar{\mathbf{k}}))$ , respectively. Here,  $n_B$  is the Bose distribution function. The matrix

$T(\bar{\mathbf{k}})$  is a matrix which diagonalizes the BdG Hamiltonian of magnons. It satisfies the following para-unitarity  $T(\bar{\mathbf{k}})^\dagger \Sigma_z T(\bar{\mathbf{k}}) = \Sigma_z$ . To take account of the finite lifetime of magnons, the phenomenological damping rate  $1/\tau_\ell$  is introduced.

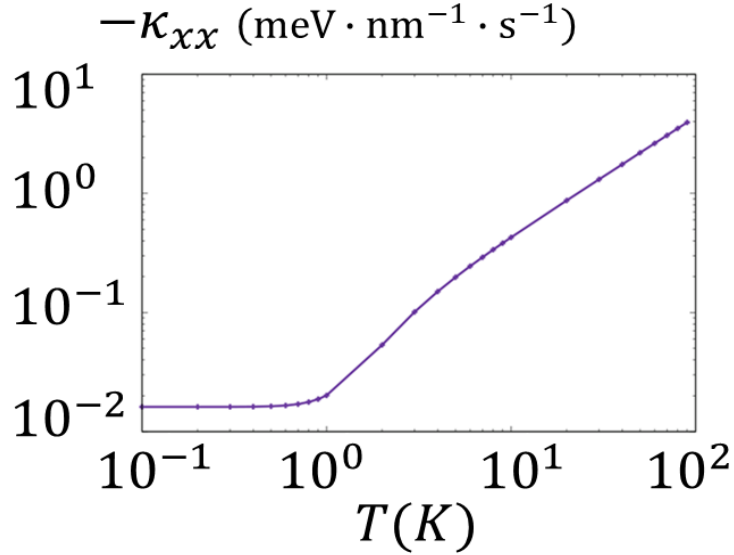


Fig. 4.3: The energy conductivity as a function of temperature. The parameters which are the same as those in Fig. 4.2 are used. The lifetime of magnons and the number of unit cells are taken to be  $1/\tau_\ell = 10^{-2}$  and  $N = 24$ , respectively. The summation in the BZ is calculated on the  $80 \times 80$  grid points.

Figure 4.3 shows the conductivity  $\kappa_{xx} = \text{Re}[\langle J_x \rangle] / (g\mu_B E_x)$  as a function of temperature  $T$ . We can see that the conductivity is a monotonically increasing function of temperature. In the zero-temperature limit,  $\kappa_{xx}$  should become zero as magnons cannot be excited, whereas it appears to be nonzero. This is due to a finite size effect. We have confirmed that the energy of the entire system increases when an electric field is applied. Therefore, the magnon flow can be considered to be driven by the energy injected by the electric field.

Magnons acquire the AC phase by an electric field, as discussed above. On the other hand, electric-field-induced DM interaction due to the superexchange mechanism [194, 195], which is proportional to the strength of the electric field, also adds a phase to magnons via the spin-orbit interaction. The form of the phase is identical to that of the AC phase as in Eq. (4.4), and thus we cannot tell them apart. The spin-orbit interaction itself in a vacuum is quite small. However, the interaction can be drastically enhanced in solids as we observed a variety of phenomena originating from the spin-orbit interaction. Indeed, the AC phase is observed in a single-crystal yttrium iron garnet [196]. It implies that the energy current induction discussed above is in the observable range.

### 4.3 Realization of Dirac surface states of magnons in CrI<sub>3</sub>

In this section, we point out that the van der Waals magnet CrI<sub>3</sub> [146–155] with the monoclinic structure is a candidate material for MAFTI. Electronic configuration  $3d^3$  of CrI<sub>3</sub> forms a honeycomb lattice structure. The magnetic moments are carried by Cr<sup>3+</sup> ions with the spin magnitude  $3/2$ . The honeycomb layers of CrI<sub>3</sub> forming the monoclinic structure are illustrated in Fig. 4.4(a). The Hamiltonian of CrI<sub>3</sub> is given by

$$\mathcal{H} = \sum_l \sum_{\gamma=x,y,z} \sum_{\langle ij \rangle_\gamma} H_{ij,l}^\gamma + D \sum_{\langle\langle ij \rangle\rangle_l} \xi_{ij} (\mathbf{S}_{i,l} \times \mathbf{S}_{j,l})_z + J' \sum_{\langle(i,l),(j,l')\rangle \in \text{mono}} \mathbf{S}_{i,l} \cdot \mathbf{S}_{j,l'} - \kappa \sum_i (S_i^z)^2. \quad (4.14)$$

Here,  $\langle ij \rangle_x$ ,  $\langle ij \rangle_y$ , and  $\langle ij \rangle_z$  are the nearest-neighbor  $x$ -,  $y$ -, and  $z$ -bonds, which are shown by red, green, and blue lines in Fig. 4.4(a), respectively.

The interactions between the sites  $i$  and  $j$  which are connected by the  $x$ -,  $y$ -, and  $z$ -bonds on the  $l$ th layer are written as follows:

$$H_{ij,l}^x = -J \mathbf{S}_{i,l} \cdot \mathbf{S}_{j,l} + K S_{i,l}^x S_{j,l}^x + \Gamma (S_{i,l}^y S_{j,l}^z + S_{i,l}^z S_{j,l}^y), \quad (4.15)$$

$$H_{ij,l}^y = -J \mathbf{S}_{i,l} \cdot \mathbf{S}_{j,l} + K S_{i,l}^y S_{j,l}^y + \Gamma (S_{i,l}^z S_{j,l}^x + S_{i,l}^x S_{j,l}^z), \quad (4.16)$$

$$H_{ij,l}^z = -J \mathbf{S}_{i,l} \cdot \mathbf{S}_{j,l} + K S_{i,l}^z S_{j,l}^z + \Gamma (S_{i,l}^x S_{j,l}^y + S_{i,l}^y S_{j,l}^x). \quad (4.17)$$

Here, the first and second terms in the right-hand sides in Eqs. (4.15) to (4.17) are the ferromagnetic Heisenberg and Kitaev interactions [197], respectively. The third terms are the symmetric off-diagonal intralayer interaction. The second term in Eq. (4.14) represents the DM interaction between the next-nearest-neighbor spins in the same layers. The third term in Eq. (4.14) is the interlayer antiferromagnetic Heisenberg interaction between the nearest-neighbor bonds across the layers in the monoclinic structure. The bonds corresponding to the summation  $\sum_{\langle\langle(i,l),(j,l')\rangle\rangle \in \text{mono}}$  are shown in the black dashed lines in Fig. 4.4(a). The last term is the easy axis anisotropy. In Appendix J, we write the BdG Hamiltonian of magnons obtained by applying the Holstein-Primakoff and Fourier transformations.

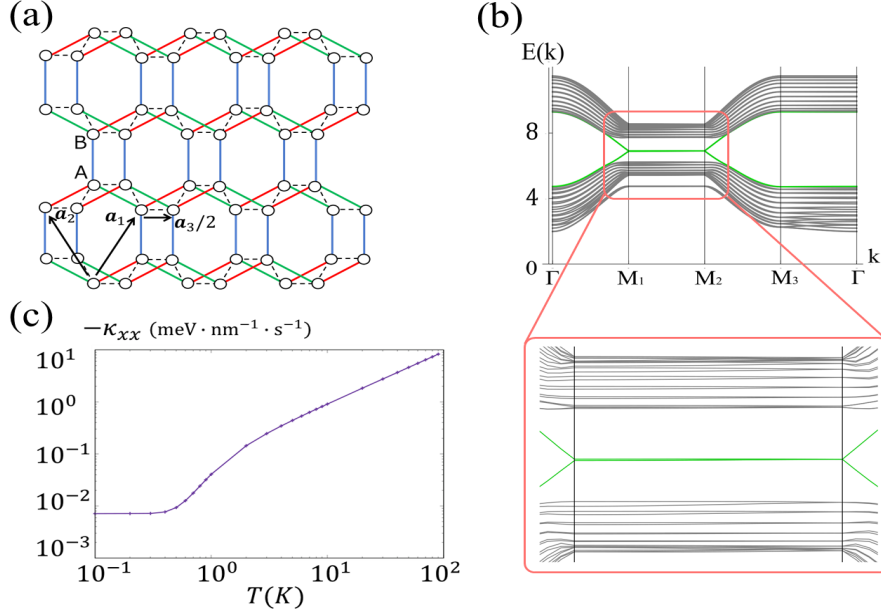


Fig. 4.4: (a) The lattice structure of CrI<sub>3</sub> with the monoclinic stacking. The  $x$ -,  $y$ -, and  $z$ -bonds are shown by the red, green, and blue bonds on the honeycomb lattice, respectively. The interlayer coupling, which is the third term in Eq. (4.14), is represented by the black dashed lines. The spins on the layers with odd (even)  $l$  are aligned in  $+z$ - ( $-z$ -) direction. The vectors  $\mathbf{a}_1$ ,  $\mathbf{a}_2$ , and  $\mathbf{a}_3$  are the lattice primitive vectors. The vector pointing from the sites in the lower layer to the corresponding ones in the upper layer corresponds to  $\mathbf{a}_3/2$ , which are along the horizontal black dashed lines. (b) Energy dispersion of magnons of a slab with (100) face of the model (4.14). We can see the gapless Dirac surface states, which is shown in green, in the band structure. The area encircled by the red frame is shown enlarged. While the gap opening at  $M_1$  point is small, we can see that the band gap closes only at  $M_2$  point, which corresponds to the single Dirac cone. (c) Energy conductivity calculated by using the linear response theory. For (b) and (c), we take the parameters to be  $J = 1.0$ ,  $K = -0.5$ ,  $\Gamma = 0.3$ ,  $D = 0.07$ ,  $J' = 0.1$ ,  $\kappa = 0.4$ , and  $S = 3/2$ . The lifetime  $\tau_\ell$  and the number of unit cells  $N$  are taken to satisfy  $1/\tau_\ell = 10^{-2}$  and  $N = 24$ , respectively. The summation in the BZ is calculated over  $80 \times 80$  grid points in (c).

The energy dispersion of magnons of the model (4.14), which are calculated for a slab with (100) face, is shown in Fig. 4.4(b). Although the gap opening at  $M_1$  is small, we can find the single Dirac cone, which is like the strong topological insulators, with the gap closing at  $M_2$  point. The parameters of the intralayer interactions in CrI<sub>3</sub> are estimated by the density functional theory calculations, which is shown in Fig. 3 in Ref. [155]. The coupling constant of the interlayer interactions is estimated according to the discussion in Ref. [151]. As in the case of the model (4.1), we can discuss the induction of the magnon current by an electric field. By using the linear response theory, the thermal conductivity  $\kappa_{xx}$  is calculated as a function of temperature, which is shown in Fig. 4.4(c). Similar to

the previous case, the energy conductivity monotonically increases with the temperature. The difference in the temperature in which the conductivities begin to increase comes from the difference between the heights of the magnon bands, i.e., the energies required to excite magnons. As seen in the phase diagram in Sec. 4.4, the topological phase which has a single Dirac cone appears in a broad region in the parameters space.

Finally, we note that the monoclinic structure of  $\text{CrI}_3$  is realized at a temperature higher than 200K, in which the magnetic order is no longer exist. However, it has been reported that the monoclinic structure remains unchanged in a thin film of  $\text{CrI}_3$  even when the temperature is lowered below 200K [152]. Therefore, we expect the magnon physics discussed in this section can be realized in a thin film of  $\text{CrI}_3$ , and similar materials.

## 4.4 Phase diagrams

The phase diagrams of models (4.1) and (4.14) are constructed and shown in Fig. 4.5(a) and (b), respectively. The phase diagram of the model (4.1) is shown as a function of  $D$  and  $\alpha$  which is a parameter introduced as  $J_0^x = 1.0 + \alpha$  and  $J_2^x = 1.0 - \alpha$ . That of the model (4.14) is constructed as a function of  $K$  and  $D$ . The ‘‘Strong’’ topological phase in the phase diagram means a topological phase which has a single Dirac cone as in the case of strong topological insulators in class AII, which we discussed in Sec. 1.1.4. In such a case, between the two bulk bands, surface states of magnons cross at only  $M_2$  point and is topologically protected by  $S$ -symmetry. On the other hand, the ‘‘Weak’’ topological phase is similar to the weak topological insulators, which possess an even number of gap closing points in the bulk band gap. The surface states in this case are not robust against disorder. What we call MAFTI is nothing but the magnets with the ‘‘Strong’’ topological phase. When the system has no surface states, it is categorized in the ‘‘Trivial’’ phase. The system is in the ‘‘Gapless’’ phase when the gap between the two bulk bands closes. We note that the ‘‘Gapless’’ phase at the zero DM interaction is a magnonic analog of nodal line semimetals.

Figure 4.5(a) implies that the ‘‘Strong’’ topological phase requires nonzero  $D$  and  $\alpha$ . Thus, for the realization of the single Dirac cone, the first, second, and third terms of the Hamiltonian in Eq. (4.1) are all necessary. The roles of the three interactions for realizing a single Dirac cone are summarized as follows. The DM interaction plays a role in making the magnon bands topologically nontrivial. The XYZ anisotropy, which breaks spin conservation, and bond dependence of the Heisenberg interaction is required for the realization of a single Dirac cone, i.e., the surface states closing the gap only at  $M_2$  point. When the system does not have these interactions, gap closing of surface states the line between  $M_1$  and  $M_2$  points, not a single Dirac cone. It is also noted that without the interlayer interaction, the system would be merely stacked Chern insulators of magnons with alternating Chern numbers. Figure 4.5(b) shows that the ‘‘Strong’’ topological phase in  $\text{CrI}_3$  is realized in a broad region around the parameters estimated by density functional theory calculations [155], which is shown by the black dot.

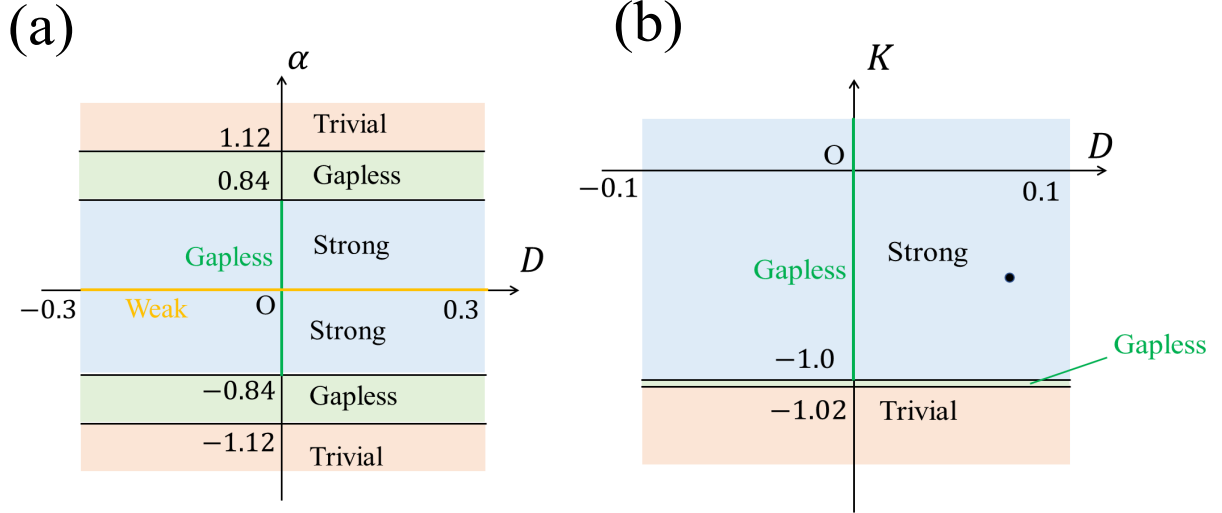


Fig. 4.5: The phase diagrams for (a) the model (4.1) and for (b) the model (4.14). In (a), we set other parameters to be  $J_0^x = 1.0 + \alpha$ ,  $J_1^x = 1.0$ ,  $J_2^x = 1.0 - \alpha$ ,  $J_0^y = J_1^y = J_2^y = 1.0$ ,  $J_0^z = J_1^z = J_2^z = 1.4$ ,  $J' = 0.5$ , and  $S = 1.0$ . In (b), the parameters are taken to be  $J = 1.0$ ,  $\Gamma = 0.3$ ,  $J' = 0.1$ ,  $\kappa = 0.4$ , and  $S = 3/2$ . The black dot shows the parameters estimated by density functional theory calculations in Refs. [151,155], i.e.,  $K = -0.5$  and  $D = 0.07$ .

## Chapter 5

# Nonlinear spin Nernst effect of magnons

In this chapter, we study the nonlinear spin Nernst effect of magnons. The magnon spin Nernst effect is interesting as a means to generate pure spin current in the magnetic insulators. So far, as discussed in Sec. 2.5, the spin Nernst effect of magnons is studied in the linear response regime. Since the linear magnon spin Nernst effect requires DM interaction, it is expected to appear in magnets containing heavy atoms. On the other hand, the generation of pure spin current in materials which do not contain heavy atoms such as organic materials is known to be difficult both in metals and insulators, since the spin-orbit and the DM interaction are negligible in these materials.

In this chapter, by considering the nonlinear topological response of magnons, namely the nonlinear spin Nernst effect of magnons, we discuss the generation of pure spin current in the magnets with negligible DM interaction. We derive the formula for the transverse current of magnons as a second-order response to the temperature gradient. In particular, the spin Nernst current in the nonlinear response regime is revealed to be described by the dipole moment of the product of the energy and the Berry curvature, which we call extended Berry curvature dipole. We note that the case is similar to the nonlinear Hall effect of electrons discussed in Sec. 1.1.6. It implies the possibility to realize spin Nernst effect in the magnets where DM interaction is negligible. We applied the formula to the various Néel antiferromagnets and found that the nonlinear magnon spin Nernst effect is expected to occur in a wide variety of magnets. In addition, we show that in some systems, the direction of nonlinear magnon spin Nernst current can be tuned by the strain.

The derivation of the expression of the nonlinear spin Nernst current of magnons is given in Sec. 5.1. In Sec. 5.2, we study the nonlinear magnon spin Nernst effect in the strained honeycomb lattice antiferromagnet. In Sec. 5.3, by comparing with the spin current as a result of the linear magnon spin Nernst effect observed in MnPS<sub>3</sub> [124], we estimate the order of the nonlinear magnon spin Nernst current. The nonlinear magnon spin Nernst effect in the square and diamond lattice antiferromagnets are studied in Sec. 5.4.

## 5.1 Expression of the nonlinear spin Nernst current of magnons

In this section, we first derive the formula for the magnon spin Nernst current up to the second-order response to the temperature gradient. Here, we assume a steady state where both ends of the system are in contact with heat baths at different temperatures. In such a case, it is known that the distribution of temperature can be written as a linear function of a position [198]. Bearing this in mind, we henceforth assume that the temperature gradient is applied in the  $x$ -direction as  $T(x) = T_0 - x\nabla T$  [199]. We assume that the temperature gradient is applied in the  $x$ -direction as  $T(x) = T_0 - x\nabla T$ , where  $\nabla T$  is a constant. According to Ref. [101], the magnon current perpendicular to the temperature gradient, i.e., in the  $y$ -direction, is written as follows:

$$J_y = -\frac{1}{\hbar V} \sum_{n,\mathbf{k}} \Omega_n(\mathbf{k}) \int_0^\infty d\epsilon \frac{\partial}{\partial x} \rho(E_n(\mathbf{k}) + \epsilon, T(x)). \quad (5.1)$$

The derivation is the same as that of Eq. (B.6) in Appendix B. The distribution function for magnons with the energy  $E$  under the temperature  $T(x)$  is given by  $\rho(E, T(x))$ . Here, the energy eigenvalue and Berry curvature of the  $n$ th band are denoted as  $E_n(\mathbf{k})$  and  $\Omega_n(\mathbf{k})$ , respectively.

The second-order response to the temperature gradient, i.e., the coefficient of  $(\nabla T)^2$  in Eq. (5.1), is obtained by solving the Boltzmann equation. Here, we assume that the density of magnons is sufficiently small so that the nonequilibrium distribution function is not far from the one in the equilibrium. With the relaxation time approximation [200–202], the Boltzmann equation can be written as

$$\begin{aligned} & \frac{\partial}{\partial t} \rho(E_n(\mathbf{k}) + \epsilon, T(x)) + \dot{\mathbf{x}} \cdot \frac{\partial}{\partial \mathbf{x}} \rho(E_n(\mathbf{k}) + \epsilon, T(x)) + \dot{\mathbf{k}} \cdot \frac{\partial}{\partial \mathbf{k}} \rho(E_n(\mathbf{k}) + \epsilon, T(x)) \\ & = -\frac{\rho(E_n(\mathbf{k}) + \epsilon, T(x)) - \rho_0(E_n(\mathbf{k}) + \epsilon, T(x))}{\tau}, \end{aligned} \quad (5.2)$$

where we define the relaxation time and the equilibrium distribution function as  $\tau$  and  $\rho_0(E, T(x)) = [e^{E/T(x)} - 1]^{-1}$ , respectively. Here,  $\dot{\mathbf{x}}$  and  $\dot{\mathbf{k}}$  are the time-derivatives of the position and the wave vector, respectively. The first and third terms on the left-hand side of Eq. (5.2), i.e.,  $(\partial/\partial t)\rho(E_n(\mathbf{k}) + \epsilon, T(x))$  and  $\dot{\mathbf{k}} \cdot (\partial/\partial \mathbf{k})\rho(E_n(\mathbf{k}) + \epsilon, T(x))$ , vanish since we assume the steady-state and the system without external field. In this case, the Boltzmann equation Eq. (5.2) is written as

$$\dot{\mathbf{x}} \frac{\partial}{\partial x} \rho(E_n(\mathbf{k}) + \epsilon, T(x)) = -\frac{\rho(E_n(\mathbf{k}) + \epsilon, T(x)) - \rho_0(E_n(\mathbf{k}) + \epsilon, T(x))}{\tau}. \quad (5.3)$$

Here, we solve this up to the first order of  $\nabla T$  as follows:

$$\begin{aligned} \rho(E_n(\mathbf{k}) + \epsilon, T(x)) &= \rho_0(E_n(\mathbf{k}) + \epsilon, T(x)) - \tau \dot{\mathbf{x}} \frac{\partial}{\partial x} \rho_0(E_n(\mathbf{k}) + \epsilon, T(x)) + O((\nabla T)^2) \\ &= \rho_0(E_n(\mathbf{k}) + \epsilon, T(x)) - \frac{\tau}{\hbar} \frac{\partial E_n(\mathbf{k})}{\partial k_x} \frac{\partial}{\partial x} \rho_0(E_n(\mathbf{k}) + \epsilon, T(x)) + O((\nabla T)^2). \end{aligned} \quad (5.4)$$

Here, the velocity  $\dot{x}$  is written as  $(1/\hbar)(\partial/\partial k_x)E_n(\mathbf{k})$ . We note that the order of the  $x$ -derivative corresponds to that of  $\nabla T$  since the system depends on  $\nabla T$  via  $T(x) = T_0 - x\nabla T$ . Since the  $x$ -derivative in Eq. (5.2) provides another  $\nabla T$ , the first and second term on the final equation are proportional to the first- and second-order of the temperature gradient, i.e.,

$$\begin{aligned} \frac{\partial}{\partial x}\rho(E_n(\mathbf{k}) + \epsilon, T(x)) &= \frac{\partial}{\partial x}\rho_0(E_n(\mathbf{k}) + \epsilon, T(x)) - \frac{\tau}{\hbar} \frac{\partial E_n(\mathbf{k})}{\partial k_x} \frac{\partial^2}{\partial x^2}\rho_0(E_n(\mathbf{k}) + \epsilon, T(x)) + O((\nabla T)^3) \\ &= -\nabla T \frac{\partial}{\partial T_0}\rho_0(E_n(\mathbf{k}) + \epsilon, T_0) + x(\nabla T)^2 \frac{\partial^2}{\partial T_0^2}\rho_0(E_n(\mathbf{k}) + \epsilon, T_0) \\ &\quad - \frac{\tau}{\hbar}(\nabla T)^2 \frac{\partial E_n(\mathbf{k})}{\partial k_x} \frac{\partial^2}{\partial T_0^2}\rho_0(E_n(\mathbf{k}) + \epsilon, T_0) + O((\nabla T)^3). \end{aligned} \quad (5.5)$$

Here, the second term in the final expression:  $x(\nabla T)^2(\partial^2/\partial T_0^2)\rho_0(E_n(\mathbf{k}) + \epsilon, T_0)$ , which is an odd function of  $x$ , vanishes in the whole space. The transverse magnon current up to a second-order of  $\nabla T$  is obtained by substituting Eq. (5.5) to Eq. (5.1) and is written as follows:

$$\begin{aligned} J_y &= \frac{\nabla T}{\hbar V} \sum_{n,\mathbf{k}} \Omega_n(\mathbf{k}) \frac{\partial}{\partial T_0} \int_0^\infty d\epsilon \rho_0(E_n(\mathbf{k}) + \epsilon, T_0) \\ &\quad + \frac{\tau(\nabla T)^2}{\hbar^2 V} \sum_{n,\mathbf{k}} \Omega_n(\mathbf{k}) \frac{\partial E_n(\mathbf{k})}{\partial k_x} \frac{\partial^2}{\partial T_0^2} \int_0^\infty d\epsilon \rho_0(E_n(\mathbf{k}) + \epsilon, T_0) + O((\nabla T)^3). \end{aligned} \quad (5.6)$$

Here, by using the function  $c_1(\rho_0) := (1 + \rho_0)\ln(1 + \rho_0) - \rho_0\ln\rho_0$ , we can write down the following equation:

$$\frac{\partial}{\partial T_0} \int_0^\infty d\epsilon \rho_0(E_n(\mathbf{k}) + \epsilon, T_0) = c_1(\rho_0(E_n(\mathbf{k}), T_0)), \quad (5.7)$$

By using the above function  $c_1(\rho_0)$  and replacing the sum over  $\mathbf{k}$  with the integral over BZ, we can rewrite the second term of the right-hand side of Eq. (5.6) as follows:

$$\begin{aligned} &\sum_{n,\mathbf{k}} \Omega_n(\mathbf{k}) \frac{\partial E_n(\mathbf{k})}{\partial k_x} \frac{\partial^2}{\partial T_0^2} \int_0^\infty d\epsilon \rho_0(E_n(\mathbf{k}) + \epsilon, T_0) \\ &= \sum_{n,\mathbf{k}} \Omega_n(\mathbf{k}) \frac{\partial E_n(\mathbf{k})}{\partial k_x} \frac{\partial}{\partial T_0} c_1(\rho_0(E_n(\mathbf{k}), T_0)) \\ &= \sum_n \int_{\text{BZ}} d^2k \Omega_n(\mathbf{k}) \frac{\partial E_n(\mathbf{k})}{\partial k_x} \left( -\frac{E_n(\mathbf{k})}{T_0} \right) \frac{\partial}{\partial E_n(\mathbf{k})} c_1(\rho_0(E_n(\mathbf{k}), T_0)) \\ &= -\frac{1}{T_0} \sum_n \int_{\text{BZ}} d^2k E_n(\mathbf{k}) \Omega_n(\mathbf{k}) \frac{\partial}{\partial k_x} c_1(\rho_0(E_n(\mathbf{k}), T_0)) \\ &= \frac{1}{T_0} \sum_n \int_{\text{BZ}} d^2k c_1(\rho_0(E_n(\mathbf{k}), T_0)) \frac{\partial}{\partial k_x} (E_n(\mathbf{k}) \Omega_n(\mathbf{k})) \end{aligned} \quad (5.8)$$

Here, the  $T_0$ -derivative acting on the function  $c_1(\rho_0(E_n(\mathbf{k}), T_0))$  can be replaced with  $(-E_n(\mathbf{k})/T_0)\partial/\partial E_n(\mathbf{k})$ , i.e.,

$$\frac{\partial}{\partial T_0} \rightarrow -\frac{E_n(\mathbf{k})}{T_0} \frac{\partial}{\partial E_n(\mathbf{k})}. \quad (5.9)$$

This is because the  $T_0$ -dependence is given in the form of  $\rho_0(E_n(\mathbf{k}), T_0) = [e^{E_n(\mathbf{k})/T_0} - 1]^{-1}$ . The above equation is used in the second equality in Eqs. (5.8). By substituting Eqs. (5.7) and (5.8) to Eq. (5.6), the expression of the magnon current perpendicular to the temperature gradient up to the second-order of  $\nabla T$  is obtained and written as follows:

$$J_y = \frac{\nabla T}{\hbar V} \sum_n \int_{\text{BZ}} d^2k c_1(\rho_0(E_n(\mathbf{k}), T_0)) \Omega_n(\mathbf{k}) + \frac{\tau(\nabla T)^2}{\hbar^2 V T_0} \sum_n \int_{\text{BZ}} d^2k c_1(\rho_0(E_n(\mathbf{k}), T_0)) \frac{\partial}{\partial k_x} (E_n(\mathbf{k}) \Omega_n(\mathbf{k})) + O((\nabla T)^3). \quad (5.10)$$

In the following, we consider the magnons in Néel antiferromagnets, in which the nearest-neighbor spins point in opposite directions, i.e., in the  $+z$  and  $-z$  -directions. Due to the perfect staggered magnetization, the systems have  $\mathcal{PT}$ -symmetry which is given by the following equation:

$$(\mathcal{PT})^{-1} \Sigma_z H(\mathbf{k}) \mathcal{PT} = \Sigma_z H(\mathbf{k}). \quad (5.11)$$

Here,  $\mathcal{P}$  and  $\mathcal{T}$  are parity and time-reversal operators, respectively. As discussed in Sec. 2.5, the magnon eigenstates in the antiferromagnets which conserve  $S^z$  are divided into the ones with magnetic moments upward and downward. Due to  $\mathcal{PT}$ -symmetry, these magnon states with magnetic moment upward and downward have the same energy.

The eigenvectors and Berry curvature of magnons with the up (down) spin dipole moment are given as  $\psi_{n,\uparrow(\downarrow)}(\mathbf{k})$  and  $\Omega_{n,\uparrow(\downarrow)}(\mathbf{k})$ , respectively. The transverse spin current is written as  $J_y^S = \hbar(J_{y,\uparrow} - J_{y,\downarrow})$  since the magnons with the up (down) spin dipole moment carry the spin angular momentum  $+\hbar$  ( $-\hbar$ ). By substituting Eq. (5.10), magnon spin Nernst current  $J_y^S$  can be written as follows:

$$J_y^S = \frac{\nabla T}{V} \sum_n \int_{\text{BZ}} d^2k c_1(\rho_0(E_n(\mathbf{k}), T_0)) (\Omega_{n,\uparrow}(\mathbf{k}) - \Omega_{n,\downarrow}(\mathbf{k})) + \frac{\tau(\nabla T)^2}{\hbar V T_0} \sum_n \int_{\text{BZ}} d^2k c_1(\rho_0(E_n(\mathbf{k}), T_0)) \frac{\partial}{\partial k_x} [E_n(\mathbf{k}) (\Omega_{n,\uparrow}(\mathbf{k}) - \Omega_{n,\downarrow}(\mathbf{k}))] + O((\nabla T)^3), \quad (5.12)$$

As seen in the above equation, the second-order spin Nernst current is written in terms of not Berry curvature dipole itself, i.e.,  $D_{n,\uparrow(\downarrow)}^x(\mathbf{k}) := (\partial/\partial k_x)(\Omega_{n,\uparrow(\downarrow)}(\mathbf{k}))$ , but the Berry-curvature-dipole-like quantity:  $\bar{D}_{n,\uparrow(\downarrow)}^x(\mathbf{k}) := (\partial/\partial k_x)[E_n(\mathbf{k})(\Omega_{n,\uparrow}(\mathbf{k}) - \Omega_{n,\downarrow}(\mathbf{k}))]$ . In the

following, we call the latter extended Berry curvature dipole. Since the  $\mathcal{PT}$ -symmetry ensures that the signs of Berry curvature of magnons with up and down spin dipole moments are opposite, i.e.,  $\Omega_{n,\uparrow}(\mathbf{k}) = -\Omega_{n,\downarrow}(\mathbf{k})$ , thermal Hall current of magnons defined in Ref. [101] is zero in both linear and nonlinear response regime. Since the nonzero values of the integral of the Berry curvature require the complex hopping terms due to DM interaction or noncollinear spin configuration, the linear spin Nernst effect is absent as well. Thus, the first term in the right-hand side of Eq. (5.12) is zero in such a case. On the other hand, the nonlinear spin Nernst effect of magnons is expected even without negligible DM interaction, since extended Berry curvature dipole can appear when the lattice breaks the inversion and rotational symmetries, as discussed in the following.

## 5.2 Honeycomb lattice antiferromagnet with strain

The nonlinear spin Nernst effect of magnons described in the second term in the right-hand side of Eq. (5.12), is expected to occur in a wide variety of magnets, since the extended Berry curvature dipole appears even without DM interaction. The first example we consider is a honeycomb lattice antiferromagnet with strain. The honeycomb lattice antiferromagnets extended along the  $x$ - and  $y$ -directions are shown in Fig. 5.1(a) and (b), respectively. The Hamiltonian is given by

$$\mathcal{H} = J_1 \sum_{\langle ij \rangle_1} \mathbf{S}_i \cdot \mathbf{S}_j + J_2 \sum_{\langle ij \rangle_2} \mathbf{S}_i \cdot \mathbf{S}_j - \kappa \sum_i (S_i^z)^2. \quad (5.13)$$

The summations about  $\langle ij \rangle_2$  and  $\langle ij \rangle_1$  are taken over the nearest-neighbor vertical bonds and the other ones shown in Fig. 5.1, respectively. Here,  $\mathbf{S}_i = (S_i^x, S_i^y, S_i^z)$  is the operator of the spin at site  $i$ . The remaining term is an easy-axis anisotropy in the  $z$ -direction.

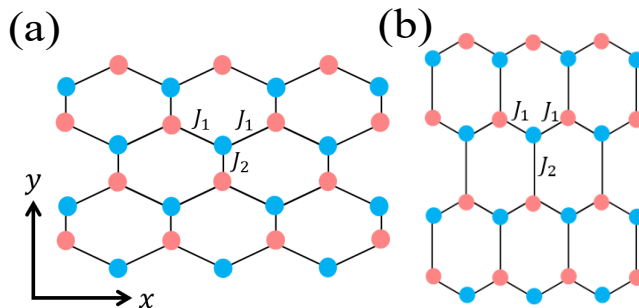


Fig. 5.1: Honeycomb lattice antiferromagnets with the strain. Red and blue circles denote spins pointing in the  $+z$  and  $-z$ -directions, respectively. In (a) and (b), the lattice is extended along the  $x$ - and  $y$ -directions, respectively. The coupling constants satisfy (a)  $J_1 < J_2$  and (b)  $J_1 > J_2$ .

By applying Holstein-Primakoff and Fourier transformations, we can write down the Hamiltonian as follows:

$$\mathcal{H} = \sum_{\mathbf{k}} \psi^\dagger(\mathbf{k}) H(\mathbf{k}) \psi(\mathbf{k}), \quad (5.14)$$

with

$$H(\mathbf{k}) = \begin{pmatrix} d & 0 & 0 & \gamma(\mathbf{k}) \\ 0 & d & \gamma^*(\mathbf{k}) & 0 \\ 0 & \gamma(\mathbf{k}) & d & 0 \\ \gamma^*(\mathbf{k}) & 0 & 0 & d \end{pmatrix}, \quad (5.15)$$

$$\psi^\dagger(\mathbf{k}) = [b_\uparrow^\dagger(\mathbf{k}), b_\downarrow^\dagger(\mathbf{k}), b_\uparrow(-\mathbf{k}), b_\downarrow(-\mathbf{k})], \quad (5.16)$$

where  $d = 2J_1S + J_2S + 2\kappa S$  and  $\gamma(\mathbf{k}) = 2J_1Se^{ik_y/2\sqrt{3}}\cos(k_x/2) + J_2Se^{-ik_y/\sqrt{3}}$ . The operator  $b_{\uparrow(\downarrow)}(\mathbf{k})$  annihilates a magnon with the dipole moment upward (downward), which is the one from spins pointing downward (upward). For this model, the parity and time-reversal operators are written as  $\mathcal{P} = 1_2 \otimes \sigma_x$  and  $\mathcal{T} = K$ , respectively. The  $\mathcal{PT}$ -symmetry in Eq. (5.11) is satisfied in the above Hamiltonian. Owing to the simple and typical model (4.1), we can find the candidate materials of the honeycomb AFMs. For example, the honeycomb AFMs 2-Cl-3,6-F<sub>2</sub>-V [207] and Mn[C<sub>10</sub>H<sub>6</sub>(OH)(COO)]<sub>2</sub>×2H<sub>2</sub>O [209] would be candidates modeled by Eq. (5.13) with  $0.7 < J_2/J_1 < 1.0$  and  $J_2 = 2J_1$ , respectively. We note that the materials possess bond-dependences inherently. Thus, the nonlinear magnon SNE is expected to exhibit even without the strain.

The band structure, Berry curvature, and extended Berry curvature dipole of magnons with up spin dipole moment in the strained honeycomb antiferromagnet are shown in Fig. 5.2. Due to the  $\mathcal{PT}$ -symmetry, those with up and down spin dipole moments are related by the following equations:

$$E_\downarrow(\mathbf{k}) = E_\uparrow(\mathbf{k}), \quad (5.17)$$

$$\Omega_\downarrow(\mathbf{k}) = -\Omega_\uparrow(\mathbf{k}), \quad (5.18)$$

$$\bar{D}_\downarrow^x(\mathbf{k}) = -\bar{D}_\uparrow^x(\mathbf{k}). \quad (5.19)$$

As seen in Figs. 5.2(a)-(d), Berry curvature and band structure are antisymmetric and symmetric about  $\mathbf{k} \rightarrow -\mathbf{k}$ . Thus, the linear spin Nernst effect is expected to be absent, which is reasonable since the DM interaction is not included in the model.

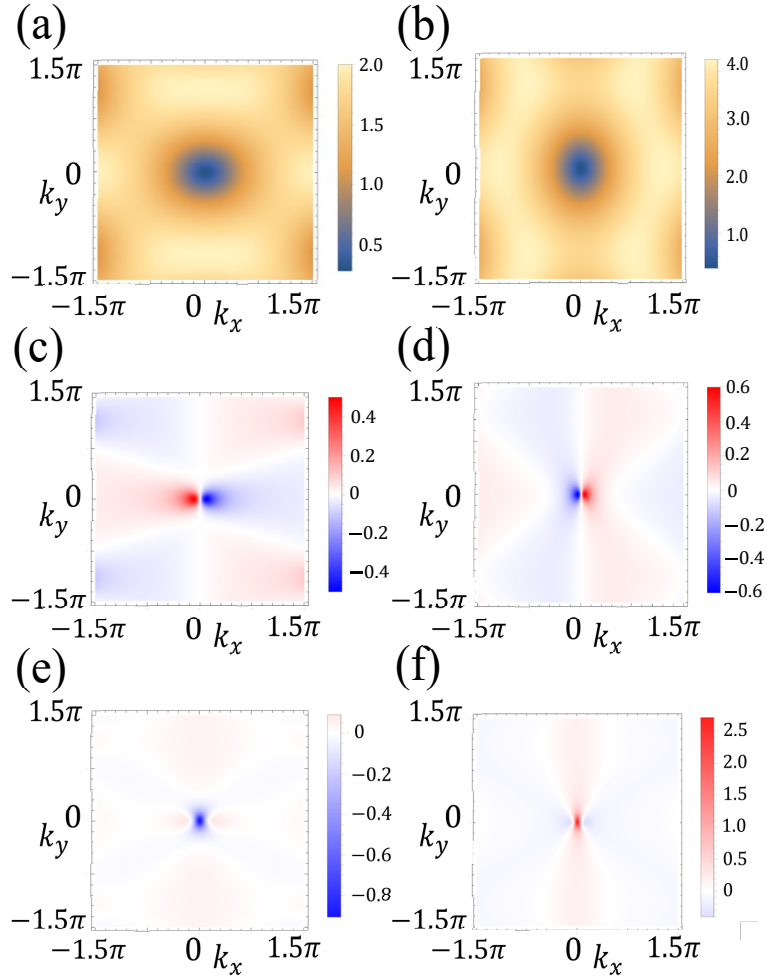


Fig. 5.2: (a), (b) Band structure  $E_{\uparrow}(\mathbf{k})$ , (c), (d) Berry curvature  $\Omega_{\uparrow}(\mathbf{k})$ , and (e), (f) extended Berry curvature dipole  $\bar{D}_{\uparrow}^x(\mathbf{k})$  of magnons with the up spin dipole moment in the strained honeycomb lattice antiferromagnet, whose Hamiltonian is given by Eq. (5.13). The parameters in (a), (c), and (e) are chosen to be  $J_1S = 0.5$ ,  $J_2S = 1.0$ , and  $\kappa S = 0.01$ , which is the case described in Fig. 5.1(a). In (b), (d), and (f), we take the parameters to be  $J_1S = 1.5$ ,  $J_2S = 1.0$ , and  $\kappa S = 0.01$ , corresponding to Fig. 5.1(b).

The coefficient of the nonlinear spin Nernst effect of magnons in Eq. (5.12) is shown in Fig. 5.3. It is zero in the case of  $J_1 = 0$  and  $J_1 = J_2$  (corresponding to the system with the three-fold rotational symmetry restored). The signs of the coefficients are opposite between the cases of  $J_1 < J_2$  and  $J_1 > J_2$ , which means that the direction of the spin Nernst current can be controlled by tuning the strain. Here, in which directions the transverse current is driven can be understood intuitively in terms of the balance of the coupling constants of the nearest-neighbor bonds; i.e., the transverse magnon current tends to flow in the direction of the stronger nearest-neighbor bonds corresponding eventually to the  $+y/-y$ -direction in total.

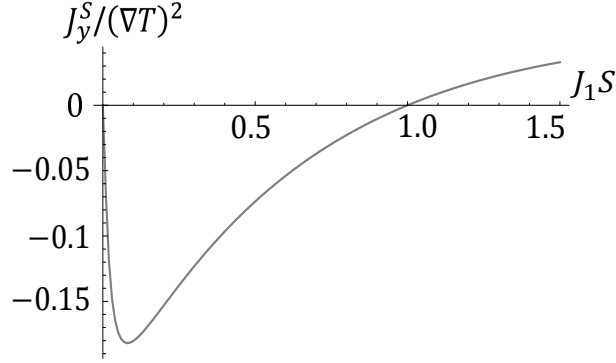


Fig. 5.3: Coefficient of the nonlinear spin Nernst effect of magnons as a function of the coupling constant  $J_1$ . We choose the other parameters to be  $J_2 S = 1.0$ , and  $\kappa S = 0.01$ , and  $T_0 = 0.1$ . The factor  $\tau/(\hbar VT_0)$  is taken to be unity.

### 5.3 Order estimation of the nonlinear spin Nernst effect

Here, let us discuss the order of the nonlinear magnon spin Nernst effect, by comparing it to the linear one observed in the honeycomb antiferromagnet MnPS<sub>3</sub> [124] with the DM interaction. We here consider the following Hamiltonian for the antiferromagnet MnPS<sub>3</sub>:

$$\mathcal{H} = J_1 \sum_{\langle ij \rangle_1} \mathbf{S}_i \cdot \mathbf{S}_j + J_2 \sum_{\langle ij \rangle_2} \mathbf{S}_i \cdot \mathbf{S}_j + D \sum_{\langle\langle ij \rangle\rangle} \xi_{ij} (\mathbf{S}_i \times \mathbf{S}_j)_z - \kappa \sum_i (S_i^z)^2, \quad (5.20)$$

where the third term is the DM interaction between the second nearest-neighbor spins. The sign convention of the DM interaction  $\xi_{ij}$  is shown in Fig. 5.4. Other terms are the same as those in the model (5.13). By applying Holstein-Primakoff and Fourier transformations, we obtain the magnon Hamiltonian for model (5.20), which is written as in the same form as in Eq. (5.16) with the additional term  $\Delta(\mathbf{k})$  derived from the DM interaction, i.e.,

$$H(\mathbf{k}) = \begin{pmatrix} d - \Delta(\mathbf{k}) & 0 & 0 & \gamma(\mathbf{k}) \\ 0 & d + \Delta(\mathbf{k}) & \gamma^*(\mathbf{k}) & 0 \\ 0 & \gamma(\mathbf{k}) & d + \Delta(\mathbf{k}) & 0 \\ \gamma^*(\mathbf{k}) & 0 & 0 & d - \Delta(\mathbf{k}) \end{pmatrix}, \quad (5.21)$$

$$\Delta(\mathbf{k}) = 2DS \left[ \sin \left( -\frac{1}{2}k_x + \frac{\sqrt{3}}{2}k_y \right) - \sin \left( \frac{1}{2}k_x + \frac{\sqrt{3}}{2}k_y \right) + \sin(k_x) \right]. \quad (5.22)$$

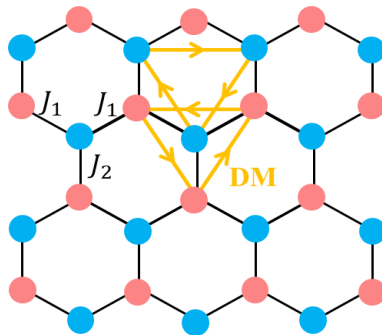


Fig. 5.4: Honeycomb lattice corresponding to the antiferromagnet  $\text{MnPS}_3$ . The sign convention  $\xi_{ij} = +1$  ( $= -\xi_{ji}$ ) for  $i \rightarrow j$  is indicated by the orange arrows.

The experiment [124] shows a good agreement with the theoretical study [120], in which the parameters of  $\text{MnPS}_3$  are considered as  $J_1 = J_2 = 1.54$  meV,  $D = 0.36$  meV,  $\kappa S = 0.0086$  meV, and  $S = 5/2$  [203]. To estimate the order of linear spin Nernst current, we ignore the second and the third nearest-neighbor Heisenberg interactions taken into account in Ref. [120], whose coupling constants are less than one-fourth of the nearest-neighbor ones. Since the antiferromagnet  $\text{MnPS}_3$  possesses the nonnegligible DM interaction, the spin current observed in  $\text{MnPS}_3$  [124] is mainly attributed to the linear spin Nernst effect, which is described by the first term in Eq. (5.12). Here, we write the part of the integral in this term as follows:

$$I_1 := \sum_n \int_{\text{BZ}} d^2k c_1(\rho_0(E_n(\mathbf{k}), T_0)) (\Omega_{n,\uparrow}(\mathbf{k}) - \Omega_{n,\downarrow}(\mathbf{k})). \quad (5.23)$$

Figure 5.5(a) shows the numerical result of  $I_1$  as a function of temperature  $T_0$  in model (5.20). From the figure, the order of the spin current at  $T_0 = 20$  K can be written as follows:

$$J_{\text{L}}^S = \frac{\nabla T}{V} \times I_1 \sim \frac{\nabla T}{V} \times 10^{-1}. \quad (5.24)$$

Next, we estimate the order of nonlinear spin Nernst effect in model (5.20) where the DM interaction is set to zero, which is equivalent to model (5.13). We here assume that the coupling constant  $J_1$  in Eq. (5.13) is changed as  $J_1 = 1.54 \rightarrow 2.0$  meV. In such a case, i.e., for  $D = 0$  and  $J_1 \neq J_2$ , the model does not exhibit the linear magnon spin Nernst effect, but the nonlinear one, which is described by the second term in Eq. (5.12). Here, we write the part of the integral of this term with the prefactor  $1/T_0$  as  $I_2$ , i.e.,

$$I_2 := \frac{1}{T_0} \sum_n \int_{\text{BZ}} d^2k c_1(\rho_0(E_n(\mathbf{k}), T_0)) \frac{\partial}{\partial k_x} [E_n(\mathbf{k}) (\Omega_{n,\uparrow}(\mathbf{k}) - \Omega_{n,\downarrow}(\mathbf{k}))]. \quad (5.25)$$

The numerical result of  $I_2$  as a function of  $T_0$  is shown in Fig. 5.5(b). From this figure, we can evaluate the nonlinear spin current at  $T_0 = 20$  K as

$$J_{\text{NL}}^S = \frac{\tau(\nabla T)^2}{\hbar V} \times I_2 \sim \frac{\tau(\nabla T)^2}{\hbar V} \times (10^{-1} \text{ meV} \cdot \text{nm} \cdot \text{K}^{-1}). \quad (5.26)$$

Since the linear spin Nernst current in Eq. (5.24) was observed with the electric voltage  $V_L \sim 1 \mu\text{V}$  through the inverse spin Hall effect at  $T_0 = 20 \text{ K}$  (see Fig. 2.6 and Fig. 3(c) in Ref. [124]), we can estimate the voltage  $V_{\text{NL}}$  by the nonlinear spin Nernst current in Eq. (5.26) in the following by taking their ratio:

$$\begin{aligned} V_{\text{NL}} &\sim V_L \times \frac{J_{\text{NL}}^S}{J_L^S} \\ &\sim 10^{-1} \mu\text{V} \times \frac{(\tau(\nabla T)^2/\hbar V) \times (10^{-1} \text{ meV} \cdot \text{ nm} \cdot \text{ K}^{-1})}{(\nabla T/V) \times 10^0} \\ &\sim 10^{n+6} \mu\text{V}. \end{aligned} \quad (5.27)$$

Here, we assume that the lifetime of magnons and the applied temperature gradient are  $\tau \sim 10^n \text{ s}$  and  $\nabla T \sim 10^{-6} \text{ K} \cdot \text{ nm}^{-1}$ , respectively. From Ref. [204], we expect that  $V_{\text{NL}} \sim 10^{-3} \mu\text{V}$  is detectable, where the magnon lifetime is  $\tau \sim 1 \text{ ns}$ . In model (5.13), the velocity of magnons is estimated as  $v = (\partial/\hbar\partial k_i)E_{\uparrow}(\mathbf{k}) \sim 10^{12} \text{ nm} \cdot \text{ s}^{-1}$ . Then, the corresponding mean free path for  $\tau \sim 1 \text{ ns}$  is  $l \sim 1 \mu\text{m}$ , which is achievable in magnets.

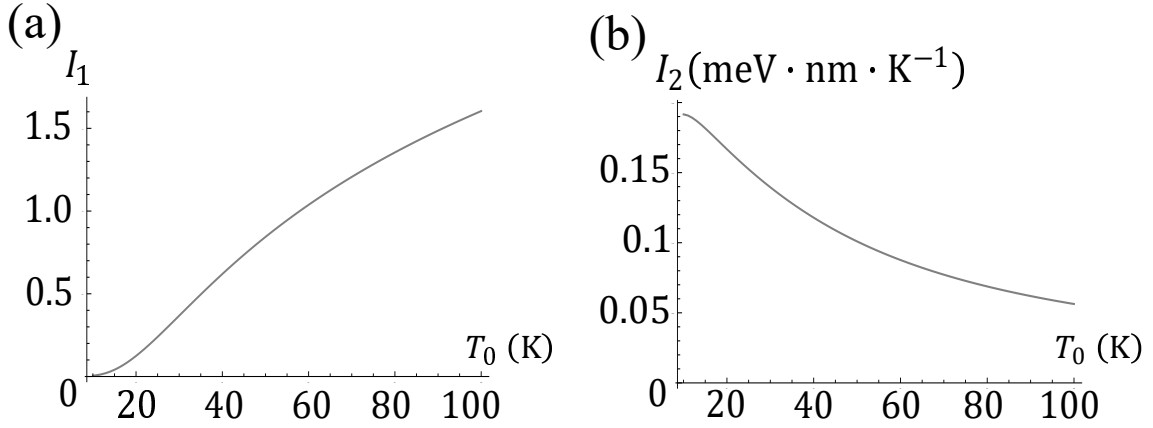


Fig. 5.5: Numerical results of (a)  $I_1$  and (b)  $I_2$  defined as Eqs. (5.23) and (5.25), respectively. The parameters  $J_1$  and  $D$  are chosen to be (a)  $J_1 = 1.54 \text{ meV}$  and  $D = 0.36 \text{ meV}$ , and (b)  $J_1 = 2.0 \text{ meV}$  and  $D = 0$ , respectively. In both (a) and (b), the other parameters  $J_2$ ,  $\kappa$ , and  $S$  are taken as  $J_2 = 1.54 \text{ meV}$ ,  $\kappa S = 0.0086 \text{ meV}$ , and  $S = 5/2$ , respectively. We note that  $I_1$  is dimensionless. In particular, at the temperature  $T_0 = 20 \text{ K}$ , the orders of them are  $I_1 \sim 10^{-1}$  and  $I_2 \sim 10^{-1} \text{ meV} \cdot \text{ nm} \cdot \text{ K}^{-1}$ , respectively.

## 5.4 Nonlinear spin Nernst effect of magnons in various antiferromagnets

Next, we discuss the nonlinear magnon spin Nernst effect in several other Néel antiferromagnets. We consider square lattice antiferromagnets with bond dependences and diamond lattice antiferromagnet under pressure, which are shown in Fig. 5.6. The Hamiltonians of the corresponding models have the same form as Eq. (5.13). The nearest-neighbor bonds  $\langle ij \rangle_1$  and  $\langle ij \rangle_2$ , whose coupling constants are  $J_1$  and  $J_2$ , are shown Fig. 5.6.

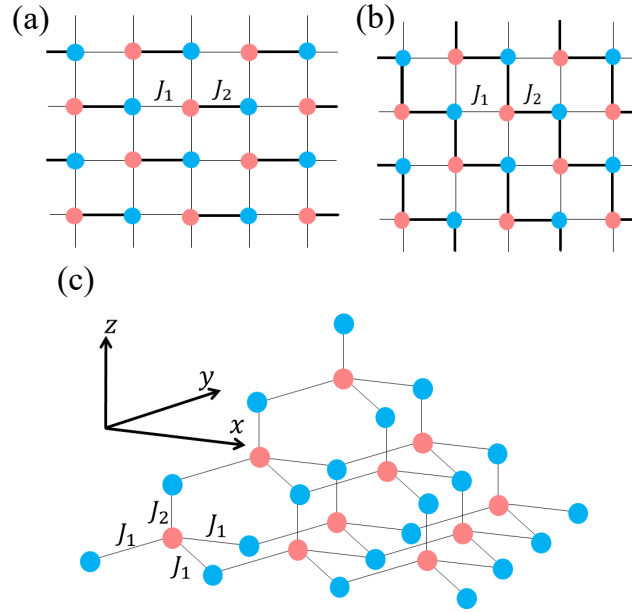


Fig. 5.6: The spin configuration and the lattice structure of the square lattice antiferromagnets with (a) staggered- and (b) zigzag-bond dependences. The bonds corresponding to the coupling constant  $J_1$  and  $J_2$ , i.e.,  $\langle ij \rangle_1$  and  $\langle ij \rangle_2$  in Eq. (5.13), are shown by the thin and thick lines, respectively. (c) The spin configuration and the lattice structure of the diamond lattice antiferromagnet, which is compressed in the  $z$ -direction due to the pressure. The vertical and the other three nearest-neighbor bonds correspond to  $\langle ij \rangle_2$  and  $\langle ij \rangle_1$  in Eq. (5.13), whose coupling constants are  $J_2$  and  $J_1$ , respectively.

By applying Holstein-Primakoff and Fourier transformations to Eq. (5.13), we can obtain the Hamiltonian for magnons, which are in the same form as Eq. (5.16) in these three cases. The Hamiltonian for these models are obtained by replacing  $d$  and  $\gamma(\mathbf{k})$  in Eq. (5.16) as in the following. Those of the square lattice antiferromagnets with staggered-bond dependence [see Fig. 5.6(a)] are given by

$$d = 3J_1S + J_2S + 2\kappa S, \quad (5.28)$$

$$\gamma(\mathbf{k}) = J_1S e^{ik_x/\sqrt{2}} + J_1S e^{ik_y/\sqrt{2}} + J_2S e^{-ik_x/\sqrt{2}} + J_1S e^{-ik_y/\sqrt{2}}. \quad (5.29)$$

In the case of the square lattice antiferromagnets with zigzag-bond dependence [see Fig. 5.6(b)], they can be written as follows:

$$d = 2J_1S + 2J_2S + 2\kappa S, \quad (5.30)$$

$$\gamma(\mathbf{k}) = J_1S e^{ik_x/\sqrt{2}} + J_1S e^{ik_y/\sqrt{2}} + J_2S e^{-ik_x/\sqrt{2}} + J_2S e^{-ik_y/\sqrt{2}}. \quad (5.31)$$

For the diamond lattice antiferromagnet [see Fig. 5.6(c)], they are given by

$$d = 3J_1S + J_2S + 2\kappa S, \quad (5.32)$$

$$\gamma(\mathbf{k}) = J_1S e^{i\mathbf{k}\cdot\mathbf{a}_0} + J_1S e^{i\mathbf{k}\cdot\mathbf{a}_1} + J_1S e^{i\mathbf{k}\cdot\mathbf{a}_2} + J_2S e^{i\mathbf{k}\cdot\mathbf{a}_3}, \quad (5.33)$$

where  $\mathbf{a}_0 = \left(0, \frac{1}{\sqrt{3}}, -\frac{1}{2\sqrt{6}}\right)$ ,  $\mathbf{a}_1 = \left(-\frac{1}{2}, -\frac{1}{2\sqrt{3}}, -\frac{1}{2\sqrt{6}}\right)$ ,  $\mathbf{a}_2 = \left(\frac{1}{2}, -\frac{1}{2\sqrt{3}}, -\frac{1}{2\sqrt{6}}\right)$ , and  $\mathbf{a}_3 = \left(0, 0, \frac{3}{4}\sqrt{\frac{2}{3}}\right)$ . The  $\mathcal{PT}$ -symmetry in Eq. (5.11) is present in these models.

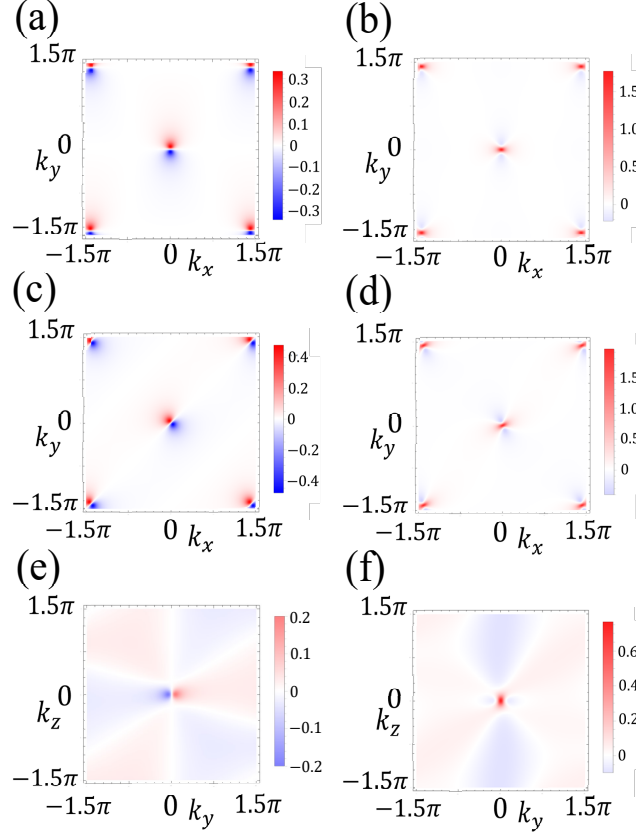


Fig. 5.7: (a),(c) Berry curvature  $\Omega_{\uparrow}(\mathbf{k})$  and (b),(d) extended Berry curvature dipole  $\bar{D}_{\uparrow}^y(\mathbf{k}) = \partial_{k_y}[E(\mathbf{k})\Omega_{\uparrow}(\mathbf{k})]$  of magnons with the up spin dipole moment in the square lattice antiferromagnets. (a) and (b) ((c) and (d)) are results for the staggered-bond (zigzag-bond) dependence in Fig. 5.6(a) (Fig. 5.6(b)), which is described by the Hamiltonian in Eqs. (5.16), (5.28), and (5.29) (Eqs. (5.16), (5.30), and (5.31)). Figures (e) and (f) show the  $x$ -component of Berry curvature  $\Omega_{\uparrow}^x(0, k_y, k_z)$  and extended Berry curvature dipole  $\bar{D}_{\uparrow}^{xy}(0, k_y, k_z)$  of magnons in the diamond lattice antiferromagnet under pressure with the Hamiltonian in Eqs. (5.16), (5.32), and (5.33), respectively. The parameters in these systems are chosen to be  $J_1S = 1.0$ ,  $J_2S = 1.2$ , and  $\kappa S = 0.01$ .

Berry curvature and extended Berry curvature dipole of magnons are calculated in these systems and shown in Fig. 5.7. In Figs. 5.7(e) and (f), the  $x$ -component of Berry curvature and extended Berry curvature dipole for the diamond lattice system defined as  $\Omega_{\uparrow}^x(\mathbf{k}) = 2\text{Im}[(\partial_{k_y}\psi_{\uparrow}(\mathbf{k}))^{\dagger}\Sigma_z(\partial_{k_z}\psi_{\uparrow}(\mathbf{k}))]$  and  $\bar{D}_{\uparrow}^{xy}(\mathbf{k}) = \partial_{k_y}[E(\mathbf{k})\Omega_{\uparrow}^x(\mathbf{k})]$  are plotted in the  $k_x = 0$  plane, respectively. The  $\mathcal{PT}$ -symmetry leads to the following equations, which relate the energy eigenvalue, Berry curvature, and extended Berry curvature dipole of up

and down spin dipole moment:

$$E_{\downarrow}(\mathbf{k}) = E_{\uparrow}(\mathbf{k}), \quad (5.34)$$

$$\Omega_{\downarrow}(\mathbf{k}) = -\Omega_{\uparrow}(\mathbf{k}), \quad (5.35)$$

$$\Omega_{\downarrow}^x(\mathbf{k}) = -\Omega_{\uparrow}^x(\mathbf{k}), \quad (5.36)$$

$$\bar{D}_{\downarrow}^x(\mathbf{k}) = -\bar{D}_{\uparrow}^x(\mathbf{k}), \quad (5.37)$$

$$\bar{D}_{\downarrow}^{xy}(\mathbf{k}) = -\bar{D}_{\uparrow}^{xy}(\mathbf{k}). \quad (5.38)$$

As in the case of the honeycomb lattice antiferromagnet in Sec. 5.2, the Berry curvatures in Figs. 5.7(a), (c), and (e) are antisymmetric, and the linear spin Nernst current is confirmed to be zero in these cases. In addition, nonzero extended Berry curvature dipoles in Figs. 5.7(b), (d), and (f) imply the existence of nonlinear spin Nernst current. In all cases, breaking the inversion and rotational symmetries by introducing bond dependence, i.e.,  $J_1 \neq J_2$ , is important for the nonzero extended Berry curvature dipoles.

The quasi-two-dimensional antiferromagnet  $\text{Cu(en)}(\text{H}_2\text{O})_2\text{SO}_4$  is a candidate material of the square lattice antiferromagnet with zigzag bond dependence, in which the coupling constants are estimated as  $J_1 = 10J_2 \sim 0.30$  meV [212]. We can also find candidate materials of the diamond lattice antiferromagnets exhibiting Néel order, such as  $\text{CoRh}_2\text{O}_4$  [213],  $\text{MnAl}_2\text{O}_4$  [214], and  $(\text{ET})\text{Ag}_4(\text{CN})_5$  [215]. In particular,  $(\text{ET})\text{Ag}_4(\text{CN})_5$  is a molecular compound, and can be distorted by applying pressure without difficulty. Thus, the pressure-tunable spin current is expected in the AFM.

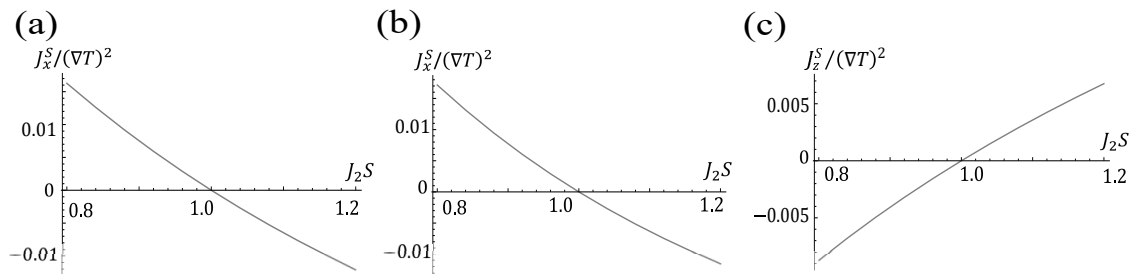


Fig. 5.8: Nonlinear spin Nernst coefficient contributed by magnons which are calculated in the square lattice antiferromagnet with the (a) staggered-, (b) zigzag-bond dependences, and (c) the diamond lattice antiferromagnet under pressure. The temperature is dependent on the position  $y$  and written as  $T(y) = T_0 - y\nabla T$ . As in the case of the honeycomb lattice antiferromagnets, the direction of the spin current in the diamond lattice antiferromagnet can be tuned externally by the applied pressure. For (a), (b), and (c), the parameters are set to be  $J_1 S = 1.0$ ,  $\kappa S = 0.01$ ,  $T_0 = 0.1$  and the factor  $\tau/(\hbar VT_0)$  is taken to be unity.

We calculate the coefficients of the nonlinear spin Nernst effect of magnons in these models as a function of  $J_2$ , which are shown in Fig. 5.8. As seen from the calculation of extended Berry curvature dipole in Fig. 5.7, we can expect the nonlinear spin Nernst

current of magnons in these cases. Since the diamond lattice is 3D, the following formula, which is obtained by generalizing Eq. (5.12), is used:

$$\begin{aligned}
J_z^S &= \frac{\nabla T}{V} \sum_n \int_{\text{BZ}} d^3k c_1(\rho_0(E_n(\mathbf{k}), T_0)) (\Omega_{n,\uparrow}^x(\mathbf{k}) - \Omega_{n,\downarrow}^x(\mathbf{k})) \\
&+ \frac{\tau(\nabla T)^2}{\hbar V T_0} \sum_n \int_{\text{BZ}} d^3k c_1(\rho_0(E_n(\mathbf{k}), T_0)) \frac{\partial}{\partial k_y} (E_n(\mathbf{k}) (\Omega_{n,\uparrow}^x(\mathbf{k}) - \Omega_{n,\downarrow}^x(\mathbf{k}))) \\
&+ O((\nabla T)^3). \tag{5.39}
\end{aligned}$$

Assuming that the pressure applied to the diamond lattice antiferromagnets change the length of bonds  $\langle ij \rangle_1$  and  $\langle ij \rangle_2$ , Since the large-and-small relationship between  $J_1$  and  $J_2$  in the diamond lattice can be changed by the direction of the pressure. Thus, the spin current in the diamond lattice antiferromagnet is pressure-tunable, which is similar to the case of the honeycomb lattice antiferromagnet.

## Chapter 6

# Summary and future prospects

In this thesis, we have investigated the surface states of magnons, which appear due to the nontrivial band topology, and the transport phenomena associated with Berry curvature. In Chap. 3, by considering the fermion-like pseudo-time-reversal symmetry, we have proposed a topological magnon system with magnon surface states, which can be regarded as a magnonic analog of a three-dimensional topological insulator. These surface states are protected by pseudo-time-reversal symmetry and have a linear Dirac dispersion. The relation between the number of surface states and the topological invariant characterizing the system has been discussed. However, the model proposed there has been realized in a very artificial setup. In Chap. 4, we have focused on the fact that the Kramers degeneracy in magnon bands occurs under the symmetry of the combination of time-reversal and half-translation. We have proposed models with magnon Dirac surface states protected by this symmetry. These surface states are similar to those proposed in Chap. 3, and shows many novel properties such as spin-momentum locking. Unlike that of Chap. 3, the models proposed here are realized in a natural setup, and we have found that the van der Waals magnet  $\text{CrI}_3$  is a candidate material. We have calculated the band structure of magnons in  $\text{CrI}_3$  at the parameters estimated by density functional theory calculations and shown that these surface states are realized. By using the linear response theory, we have discussed the induction of the magnon current caused by the spin-momentum locking of the magnon surface states and the Aharonov-Casher effect in an electric field. In Chap. 5, we have proposed the nonlinear spin Nernst effect for magnons. By considering the second-order response to a temperature gradient, we have found that the magnon current perpendicular to the temperature gradient can be described by a dipole moment of the product of the energy and the Berry curvature. This nonlinear spin Nernst effect is expected to occur in many antiferromagnets without the Dzyaloshinskii-Moriya interaction.

To summarize, the main results of our studies are as follows.

- The first model of a magnon system with surface states like those of three-dimensional topological insulators of electrons has been constructed.
- By considering the counterparts of topological crystalline insulators of electrons, we have realized similar surface states in natural setups.

- We have calculated the magnon band structure of  $\text{CrI}_3$  and confirmed the existence of surface states.
- The characteristic electric field response due to the surface states has been proposed.
- We have developed a theory of the nonlinear spin Nernst effect of magnons.

The future prospects are as follows. The magnon surface states proposed in this study are the counterparts of those observed in three-dimensional topological insulators, which are known to exhibit many interesting properties in electronic systems. It is possible to study various phenomena similar to those investigated in electronic systems as well as those unique to magnon systems. For example, since the surface state is spin-polarized, the Edelstein effect is expected. By the current resolution of inelastic neutron scattering, the surface states of magnons are difficult to be measured. Therefore, the existence of the proposed surface states should be proved by measuring related transport phenomena. Thus we hope that future experiments will enable us to observe phenomena such as the induction of the magnon current by an electric field proposed in this thesis and the Edelstein effect. Another future direction is to explore the magnon surface states, which are protected by symmetries other than the pseudo-time-reversal symmetry and the symmetry of the combination of time-reversal and half translation. For example, in electronic systems, surface states protected by a combination of time-reversal and  $C_4$  rotation have been investigated [32], and similar ones can be considered for magnon systems. Depending on which symmetry the surface state is protected by, properties such as dispersion relations will change, resulting in many novel phenomena in magnon systems. The nonlinear spin Nernst effect of magnons is expected to be measured by converting it into an electric current using the inverse spin Hall effect in Pt. Fortunately, we can consider many candidate materials which exhibit the nonlinear spin Nernst effect of magnons, e.g., antiferromagnets on a honeycomb lattice [205–211], square lattice with zigzag bond dependence [212], and diamond lattice [213–215]. Those with large bond dependence and long magnon lifetime should be targets for the measurement. In particular, we expect to find purely nonlinear contributions in magnets which only contain light atoms, since the Dzyaloshinskii-Moriya interaction is typically very small even if the inversion symmetry is broken. We here emphasize that our proposal for the nonlinear magnon spin Nernst effect provides one of a few possible ways to generate the spin current in materials without heavy atoms, such as organic materials [216, 217] where the Dzyaloshinskii-Moriya interaction is negligible. We expect that our results will lead to new ways of the manipulation of magnons and spin currents, which can be first enabled by their topological properties, and will stimulate the field of spintronics.

# Appendix

## Appendix A : Proof of the statements in Sec. 2.2

In this part, we prove the three statements (i)-(iii) in Sec. 2.2.

*Proof of (i).*

By using the eigenvalues  $\lambda_n(\mathbf{k})$  ( $n = 1, \dots, 2\mathcal{N}$ ) and the unitary matrix  $U(\mathbf{k})$ , the Hamiltonian matrix  $H(\mathbf{k})$  can be written as

$$H(\mathbf{k}) = U^\dagger(\mathbf{k}) \text{diag}(\lambda_1(\mathbf{k}), \dots, \lambda_{2\mathcal{N}}(\mathbf{k})) U(\mathbf{k}). \quad (\text{A.1})$$

In the following, we assume that the eigenvalues are positive definite. The above equation can be written as  $H(\mathbf{k}) = Q^\dagger(\mathbf{k})Q(\mathbf{k})$ , where,  $Q(\mathbf{k})$  is a regular matrix given by  $Q(\mathbf{k}) = \text{diag}(\sqrt{\lambda_1(\mathbf{k})}, \dots, \sqrt{\lambda_{2\mathcal{N}}(\mathbf{k})}) U(\mathbf{k})$ . The eigenvalues of  $\Sigma_z H(\mathbf{k})$  is the same as a matrix  $\Omega(\mathbf{k}) = Q(\mathbf{k}) \Sigma_z Q^\dagger(\mathbf{k})$  since they are similar to each other. We note that the matrix  $\Omega(\mathbf{k})$  is Hermitian and its determinant is nonzero, i.e.,

$$\text{Det}(\Omega(\mathbf{k})) = \text{Det}(\Sigma_z) \text{Det}(H(\mathbf{k})) = (-1)^{\mathcal{N}} \text{Det}(Q(\mathbf{k})Q^\dagger(\mathbf{k})) \neq 0. \quad (\text{A.2})$$

Thus, we can show that as those of  $\Omega(\mathbf{k})$ , the eigenvalues of  $\Sigma_z H(\mathbf{k})$  is real and nonzero.  $\square$

*Proof of (ii).* Let us take the complex conjugate of the eigen equation  $\Sigma_z H(\mathbf{k})\psi(\mathbf{k}) = E(\mathbf{k})\psi(\mathbf{k})$  and reverse the direction of the wave vector, i.e.,

$$\Sigma_z H^*(-\mathbf{k})\psi^*(-\mathbf{k}) = E(-\mathbf{k})\psi^*(-\mathbf{k}). \quad (\text{A.3})$$

By multiplying the above equation from the left by  $\Sigma_x$  and by using the anti-commutation relation  $\{\Sigma_z, \Sigma_x\} = 0$  and  $\Sigma_x^2 = 1_{2\mathcal{N}}$ , we obtain the following equation:

$$-\Sigma_z \Sigma_x H^*(-\mathbf{k}) \Sigma_x \Sigma_x \psi^*(-\mathbf{k}) = E(-\mathbf{k}) \Sigma_x \psi^*(-\mathbf{k}). \quad (\text{A.4})$$

Since the BdG Hamiltonian satisfies  $\Sigma_x H(\mathbf{k}) \Sigma_x = H^*(-\mathbf{k})$ , we can write the above equation as follows:

$$\Sigma_z H(\mathbf{k}) \Sigma_x \psi^*(-\mathbf{k}) = -E(-\mathbf{k}) \Sigma_x \psi^*(-\mathbf{k}). \quad (\text{A.5})$$

$\square$

In the following, the eigenvalues and the eigenvectors of  $\Sigma_z H(\mathbf{k})$  are arranged as follows:

$$(E_1(\mathbf{k}), \dots, E_{\mathcal{N}}(\mathbf{k}), -E_1(-\mathbf{k}), \dots, -E_{\mathcal{N}}(-\mathbf{k})), \quad (\text{A.6})$$

$$(\boldsymbol{\psi}_1(\mathbf{k}), \dots, \boldsymbol{\psi}_{\mathcal{N}}(\mathbf{k}), \Sigma_x \boldsymbol{\psi}_1^*(-\mathbf{k}), \dots, \Sigma_x \boldsymbol{\psi}_{\mathcal{N}}^*(-\mathbf{k})). \quad (\text{A.7})$$

We denote the eigenvectors as

$$\boldsymbol{\psi}_{n+}(\mathbf{k}) = \boldsymbol{\psi}_n(\mathbf{k}), \quad (\text{A.8})$$

$$\boldsymbol{\psi}_{n-}(\mathbf{k}) = \Sigma_x \boldsymbol{\psi}_n^*(-\mathbf{k}). \quad (\text{A.9})$$

It should be noted that the matrix in Eq. (A.7) is nothing but the para-unitary matrix  $T(\mathbf{k})$  in Eq. (2.21).

*Proof of (iii).*

Since the eigenvalues of  $\Omega(\mathbf{k}) = Q(\mathbf{k})\Sigma_z Q^\dagger(\mathbf{k})$  is  $\pm E_n(\mathbf{k})$  ( $E_n(\mathbf{k}) > 0; n = 1, \dots, \mathcal{N}$ ), the eigen equation of  $\Omega(\mathbf{k})$  can be written as follows:

$$\Omega(\mathbf{k})\boldsymbol{\phi}_{n\sigma}(\mathbf{k}) = \sigma E_n(\mathbf{k})\boldsymbol{\phi}_{n\sigma}(\mathbf{k}), \quad (\text{A.10})$$

where  $\boldsymbol{\phi}_{n\sigma}(\mathbf{k})$  is the eigenvectors. We can choose the orthogonal set of the eigenvectors, i.e.,

$$\langle \boldsymbol{\phi}_{m\rho}(\mathbf{k}), \boldsymbol{\phi}_{n\sigma}(\mathbf{k}) \rangle = \boldsymbol{\phi}_{m\rho}^\dagger(\mathbf{k})\boldsymbol{\phi}_{n\sigma}(\mathbf{k}) = \delta_{nm}\delta_{\sigma\rho}. \quad (\text{A.11})$$

We can see that the vector defined as  $\boldsymbol{\psi}_{n\sigma}(\mathbf{k}) := \sqrt{E_n(\mathbf{k})}Q^{-1}(\mathbf{k})\boldsymbol{\phi}_{n\sigma}(\mathbf{k})$  satisfies the following equation:

$$\Sigma_z H(\mathbf{k})\boldsymbol{\psi}_{n\sigma}(\mathbf{k}) = \sigma E_n(\mathbf{k})\boldsymbol{\psi}_{n\sigma}(\mathbf{k}), \quad (\text{A.12})$$

which implies that  $\boldsymbol{\psi}_{n\sigma}(\mathbf{k})$  is an eigenvector of  $\Sigma_z H(\mathbf{k})$  with eigenvalue  $\sigma E_n(\mathbf{k})$ . By using the equation:

$$\begin{aligned} [Q^{-1}(\mathbf{k})]^{-1}\Sigma_z Q^{-1}(\mathbf{k})\boldsymbol{\phi}_{n\sigma}(\mathbf{k}) &= \Omega^{-1}(\mathbf{k})\boldsymbol{\phi}_{n\sigma}(\mathbf{k}) \\ &= (\sigma E_n(\mathbf{k}))^{-1}\boldsymbol{\phi}_{n\sigma}(\mathbf{k}), \end{aligned} \quad (\text{A.13})$$

we can see that the following para-unitarity relation is satisfied by  $\boldsymbol{\psi}_{n\sigma}(\mathbf{k})$ , i.e.,

$$\begin{aligned} \langle \langle \boldsymbol{\psi}_{m\rho}(\mathbf{k}), \boldsymbol{\psi}_{n\sigma}(\mathbf{k}) \rangle \rangle &= \boldsymbol{\psi}_{m\rho}^\dagger(\mathbf{k})\Sigma_z \boldsymbol{\psi}_{n\sigma}(\mathbf{k}) \\ &= \sqrt{E_n(\mathbf{k})E_m(\mathbf{k})}\boldsymbol{\phi}_{m\rho}^\dagger(\mathbf{k})[Q^{-1}(\mathbf{k})]^{-1}\Sigma_z Q^{-1}(\mathbf{k})\boldsymbol{\phi}_{n\sigma}(\mathbf{k}) \\ &= \sigma \sqrt{\frac{E_n(\mathbf{k})}{E_m(\mathbf{k})}}\boldsymbol{\phi}_{m\rho}^\dagger(\mathbf{k})\boldsymbol{\phi}_{n\sigma}(\mathbf{k}) \\ &= \sigma \delta_{nm}\delta_{\sigma\rho}. \end{aligned} \quad (\text{A.14})$$

□

## Appendix B : Derivation of magnon thermal Hall current

Here, we derive the expression of the magnon thermal Hall current (2.26). As in the case of electrons, the semiclassical equation of motion of magnons are written as follows:

$$\dot{\mathbf{r}} = \frac{1}{\hbar} \frac{\partial \epsilon(\mathbf{k})}{\partial \mathbf{k}} - \dot{\mathbf{k}} \times \boldsymbol{\Omega}_n(\mathbf{k}), \quad (\text{B.1})$$

$$\hbar \dot{\mathbf{k}} = -\nabla U(\mathbf{r}). \quad (\text{B.2})$$

Thus, the velocity can be written as  $\dot{\mathbf{r}} = (1/\hbar)\nabla U(\mathbf{r}) \times \boldsymbol{\Omega}_n(\mathbf{k})$ . Let us consider the current in the  $x$ -direction in a temperature gradient applied in the  $y$ -direction. The magnon current at the position  $y$  is given by

$$\begin{aligned} J_x(y) &= \frac{1}{V} \sum_{n,\mathbf{k}} \rho(\epsilon_{n,\mathbf{k}} + U(\mathbf{r}), T(y)) \dot{x} \\ &= \frac{1}{\hbar V} \sum_{n,\mathbf{k}} \rho(\epsilon_{n,\mathbf{k}} + U(\mathbf{r}), T(y)) \frac{\partial}{\partial y} U(\mathbf{r}) \Omega_n^z(\mathbf{k}). \end{aligned} \quad (\text{B.3})$$

Here, we write the width of the system in the  $y$ -direction as  $\omega$ , where the center is taken to be  $y = 0$ . When  $b_1$  and  $b_2$  are set to be  $b_1 < -\omega/2$  and  $\omega/2 < b_2$ , respectively, the potential energy of magnons satisfies  $U(y = b_1) = U(y = b_2) = \infty$ . Therefore, the magnon current in the  $x$ -direction in the whole space is written as follows:

$$J_x = \frac{1}{\omega} \int_{b_1}^{b_2} dy J_x(y). \quad (\text{B.4})$$

Here, we divide the systems into the two regions as  $b_1 \leq y \leq a$  and  $a \leq y \leq b_2$ , where the position  $y = a$  is set to be in the systems, i.e.,  $U(y = a) = 0$ . In the first region  $b_1 \leq y \leq a$ , we can roughly take the temperature as  $T(y) \neq T(-\omega/2)$ . The integral in this region is calculated as follows:

$$\begin{aligned} \frac{1}{\omega} \int_{b_1}^a dy J_x(y) &= \frac{1}{\omega} \frac{1}{\hbar V} \sum_{n,\mathbf{k}} \int_{b_1}^a dy \frac{\partial U(\mathbf{r})}{\partial y} \rho(\epsilon_{n,\mathbf{k}} + U(\mathbf{r}), T(y)) \Omega_n^z(\mathbf{k}) \\ &= \frac{1}{\omega} \frac{1}{\hbar V} \sum_{n,\mathbf{k}} \int_{-\infty}^0 dU \rho(\epsilon_{n,\mathbf{k}} + U, T(-\omega/2)) \Omega_n^z(\mathbf{k}) \\ &= -\frac{1}{\omega} \frac{1}{\hbar V} \sum_{n,\mathbf{k}} \int_{\epsilon_{n,\mathbf{k}}}^{\infty} d\epsilon \rho(\epsilon, T(-\omega/2)) \Omega_n^z(\mathbf{k}). \end{aligned} \quad (\text{B.5})$$

By calculating the integral in the second region  $a \leq y \leq b_2$ , the magnon current (B.4) can be written as

$$\begin{aligned} J_x &= \frac{1}{\omega} \frac{1}{\hbar V} \sum_{n, \mathbf{k}} \int_{\epsilon_{n, \mathbf{k}}}^{\infty} d\epsilon (\rho(\epsilon, T(\omega/2)) - \rho(\epsilon, T(-\omega/2))) \Omega_n^z(\mathbf{k}). \\ &= \frac{1}{\hbar V} \sum_{n, \mathbf{k}} \int_{\epsilon_{n, \mathbf{k}}}^{\infty} d\epsilon \left( \frac{\partial}{\partial x} \rho(\epsilon, T(x)) \right) \Omega_n^z(\mathbf{k}). \end{aligned} \quad (\text{B.6})$$

The magnon current is often interested in terms of the transport properties of the spin magnetic moment and the energy. For example, magnons from spins upward are considered to have a magnetic moment  $-\hbar$ . Thus, the spin and energy currents conveyed by the magnons, in this case, are written as follows:

$$J_x^S = -\frac{1}{V} \sum_{n, \mathbf{k}} \int_{\epsilon_{n, \mathbf{k}}}^{\infty} d\epsilon \frac{\partial \rho(\epsilon, T(y))}{\partial y} \Omega_n^z(\mathbf{k}), \quad (\text{B.7})$$

$$J_x^E = \frac{1}{\hbar V} \sum_{n, \mathbf{k}} \int_{\epsilon_{n, \mathbf{k}}}^{\infty} d\epsilon \epsilon \frac{\partial \rho(\epsilon, T(y))}{\partial y} \Omega_n^z(\mathbf{k}). \quad (\text{B.8})$$

In particular, the energy current (B.8) is rewritten as

$$J_x^E = -\frac{1}{T} \frac{\partial T}{\partial y} \frac{1}{\hbar V} \sum_{n, \mathbf{k}} \int_{\epsilon_{n, \mathbf{k}}}^{\infty} d\epsilon \epsilon^2 \frac{\partial \rho(\epsilon, T)}{\partial \epsilon} \Omega_n^z(\mathbf{k}). \quad (\text{B.9})$$

By using the function  $c_q(\rho)$  defined as

$$c_q(\rho) = \int_{\epsilon_{n, \mathbf{k}}}^{\infty} d\epsilon (\beta \epsilon)^q \left( -\frac{\partial \rho(\epsilon, T)}{\partial \epsilon} \right) = \int_0^\rho dt (\log(1 + 1/t))^q, \quad (\text{B.10})$$

we finally obtain the formula for the thermal Hall current of magnons Eq. (2.26), i.e.,

$$\kappa^{xy} = -\frac{k_B^2 T}{\hbar V} \sum_{n, \mathbf{k}} c_2(\rho_n) \Omega_n(\mathbf{k}). \quad (\text{B.11})$$

## Appendix C : Kramers pairs of bosons described by Bogoliubov-de Gennes Hamiltonians

In the main text, we mentioned that the Kramers theorem can be applied when the systems are symmetric under an anti-unitary operator which squares to  $-1$ . However, the proof of the Kramers theorem is a bit different from the case of electrons due to the peculiar mathematical properties of magnons described by the BdG Hamiltonian. In this part, we give the details of the proof of the Kramers theorem in such a case. We here show that under certain symmetry, the eigenvalues of the matrix  $\Sigma_z H(\mathbf{\Lambda})$  degenerate at TRIM:  $\mathbf{k} = \mathbf{\Lambda}$ .

By using a para-unitary matrix  $P$  and the complex conjugation  $K$ , we define an anti-unitary operator  $O = PK$  which satisfies

$$O^2 = -1. \quad (\text{C.1})$$

We assume that the system is symmetric under this operator and satisfies

$$\Sigma_z H(\mathbf{\Lambda}) O - O \Sigma_z H(\mathbf{\Lambda}) = 0, \quad (\text{C.2})$$

Here, we write the eigenvector of  $\Sigma_z H(\mathbf{\Lambda})$  with the eigenvalue  $E(\mathbf{\Lambda})$  as  $\boldsymbol{\psi}(\mathbf{\Lambda})$ , i.e.,

$$\Sigma_z H(\mathbf{\Lambda}) \boldsymbol{\psi}(\mathbf{\Lambda}) = E(\mathbf{\Lambda}) \boldsymbol{\psi}(\mathbf{\Lambda}). \quad (\text{C.3})$$

Multiplying both sides of Eq. (C.3) from the left by  $O$ , we obtain

$$\Sigma_z H(\mathbf{\Lambda}) O \boldsymbol{\psi}(\mathbf{\Lambda}) = E(\mathbf{\Lambda}) O \boldsymbol{\psi}(\mathbf{\Lambda}). \quad (\text{C.4})$$

Here, we used the commutation relations Eq. (C.2). Thus, the two vectors  $\boldsymbol{\psi}(\mathbf{\Lambda})$  and  $O \boldsymbol{\psi}(\mathbf{\Lambda})$  are both the eigenvectors of  $\Sigma_z H(\mathbf{\Lambda})$  with the same eigenvalue  $E(\mathbf{\Lambda})$ .

Next, we show that these vectors are orthogonal to each other. The inner product of these vectors can be deformed as the following:

$$\begin{aligned} \langle\langle \boldsymbol{\psi}(\mathbf{\Lambda}), O \boldsymbol{\psi}(\mathbf{\Lambda}) \rangle\rangle &= - \langle\langle O^2 \boldsymbol{\psi}(\mathbf{\Lambda}), O \boldsymbol{\psi}(\mathbf{\Lambda}) \rangle\rangle \\ &= - (O^2 \boldsymbol{\psi}(\mathbf{\Lambda}))_i^* (\Sigma_z P)_{ij} \psi_j^*(\mathbf{\Lambda}) \\ &= - \psi_j^*(\mathbf{\Lambda}) (P^T \Sigma_z)_{ji} (K O^2 \boldsymbol{\psi}(\mathbf{\Lambda}))_i \\ &= - \langle\langle \boldsymbol{\psi}(\mathbf{\Lambda}), \Sigma_z P^T \Sigma_z K O^2 \boldsymbol{\psi}(\mathbf{\Lambda}) \rangle\rangle. \\ &= - \langle\langle \boldsymbol{\psi}(\mathbf{\Lambda}), (\Sigma_z P^T \Sigma_z K P K) O \boldsymbol{\psi}(\mathbf{\Lambda}) \rangle\rangle \\ &= - \langle\langle \boldsymbol{\psi}(\mathbf{\Lambda}), O \boldsymbol{\psi}(\mathbf{\Lambda}) \rangle\rangle. \end{aligned} \quad (\text{C.5})$$

Thus, we confirmed that vectors  $\boldsymbol{\psi}(\mathbf{\Lambda})$  and  $O \boldsymbol{\psi}(\mathbf{\Lambda})$  are orthogonal to each other, i.e.,  $\langle\langle \boldsymbol{\psi}(\mathbf{\Lambda}), O \boldsymbol{\psi}(\mathbf{\Lambda}) \rangle\rangle = 0$ . Here, in the final equality in Eq. (C.5), we used the following equation:

$$\Sigma_z P^T \Sigma_z K P K = (\Sigma_z P^\dagger \Sigma_z P)^* = \Sigma_z^2 = 1_{2\mathcal{N}}, \quad (\text{C.6})$$

which is derived from the para-unitarity of  $P$ .

## Appendix D : Details of the interactions in the Hamiltonian (3.1)

In Sec. 3.1, we proposed the first model of magnonic analog of 3D topological insulators. In this part, we give an explicit expression of the interactions in the Hamiltonian (3.1).

They are given by the following equations:

$$\begin{aligned}
H_{\text{DM}} = & \sum_{\mathbf{R}, s=u, d} D_1^z (S_s^x(\mathbf{R}, A) S_s^y(\mathbf{R} + \mathbf{a}_1, A) - S_s^y(\mathbf{R}, A) S_s^x(\mathbf{R} + \mathbf{a}_1, A)) \\
& + D_2^z (S_s^x(\mathbf{R}, A) S_s^y(\mathbf{R} + \mathbf{a}_2, A) - S_s^y(\mathbf{R}, A) S_s^x(\mathbf{R} + \mathbf{a}_2, A)) \\
& + D_3^z (S_s^x(\mathbf{R}, A) S_s^y(\mathbf{R} + \mathbf{a}_3, A) - S_s^y(\mathbf{R}, A) S_s^x(\mathbf{R} + \mathbf{a}_3, A)) \\
& + D_{21}^z (S_s^x(\mathbf{R}, A) S_s^y(\mathbf{R} + \mathbf{a}_{21}, A) - S_s^y(\mathbf{R}, A) S_s^x(\mathbf{R} + \mathbf{a}_{21}, A)) \\
& + D_{31}^z (S_s^x(\mathbf{R}, A) S_s^y(\mathbf{R} + \mathbf{a}_{31}, A) - S_s^y(\mathbf{R}, A) S_s^x(\mathbf{R} + \mathbf{a}_{31}, A)) \\
& + D_{32}^z (S_s^x(\mathbf{R}, A) S_s^y(\mathbf{R} + \mathbf{a}_{32}, A) - S_s^y(\mathbf{R}, A) S_s^x(\mathbf{R} + \mathbf{a}_{32}, A)) \\
& - (A \leftrightarrow B), \tag{D.1}
\end{aligned}$$

$$H_{J'} = J' \sum_i \mathbf{S}_{i,u} \cdot \mathbf{S}_{i,d}, \tag{D.2}$$

$$\begin{aligned}
H_J = & - \sum_{\mathbf{R}, s=u, d} J_0 \mathbf{S}_s(\mathbf{R}, A) \cdot \mathbf{S}_s(\mathbf{R}, B) + J_1 \mathbf{S}_s(\mathbf{R}, A) \cdot \mathbf{S}_s(\mathbf{R} + \mathbf{a}_1, B) \\
& + J_2 \mathbf{S}_s(\mathbf{R}, A) \cdot \mathbf{S}_s(\mathbf{R} + \mathbf{a}_2, B) + J_3 \mathbf{S}_s(\mathbf{R}, A) \cdot \mathbf{S}_s(\mathbf{R} + \mathbf{a}_3, B), \tag{D.3}
\end{aligned}$$

$$\begin{aligned}
H_{\text{XY}} = & J_- \sum_{\mathbf{R}} \bar{D}_1^y (S_u^x(\mathbf{R}, A) S_d^x(\mathbf{R} + \mathbf{a}_1, A) - S_u^y(\mathbf{R}, A) S_d^y(\mathbf{R} + \mathbf{a}_1, A)) \\
& + \bar{D}_2^y (S_u^x(\mathbf{R}, A) S_d^x(\mathbf{R} + \mathbf{a}_2, A) - S_u^y(\mathbf{R}, A) S_d^y(\mathbf{R} + \mathbf{a}_2, A)) \\
& + \bar{D}_3^y (S_u^x(\mathbf{R}, A) S_d^x(\mathbf{R} + \mathbf{a}_3, A) - S_u^y(\mathbf{R}, A) S_d^y(\mathbf{R} + \mathbf{a}_3, A)) \\
& + \bar{D}_{21}^y (S_u^x(\mathbf{R}, A) S_d^x(\mathbf{R} + \mathbf{a}_{21}, A) - S_u^y(\mathbf{R}, A) S_d^y(\mathbf{R} + \mathbf{a}_{21}, A)) \\
& + \bar{D}_{31}^y (S_u^x(\mathbf{R}, A) S_d^x(\mathbf{R} + \mathbf{a}_{31}, A) - S_u^y(\mathbf{R}, A) S_d^y(\mathbf{R} + \mathbf{a}_{31}, A)) \\
& + \bar{D}_{32}^y (S_u^x(\mathbf{R}, A) S_d^x(\mathbf{R} + \mathbf{a}_{32}, A) - S_u^y(\mathbf{R}, A) S_d^y(\mathbf{R} + \mathbf{a}_{32}, A)) \\
& - (u \leftrightarrow d) \\
& - (A \leftrightarrow B), \tag{D.4}
\end{aligned}$$

$$\begin{aligned}
H_{\Gamma} = & \Gamma \sum_{\mathbf{R}} \bar{D}_1^x (S_u^x(\mathbf{R}, A) S_d^y(\mathbf{R} + \mathbf{a}_1, A) + S_u^y(\mathbf{R}, A) S_d^x(\mathbf{R} + \mathbf{a}_1, A)) \\
& + \bar{D}_2^x (S_u^x(\mathbf{R}, A) S_d^y(\mathbf{R} + \mathbf{a}_2, A) + S_u^y(\mathbf{R}, A) S_d^x(\mathbf{R} + \mathbf{a}_2, A)) \\
& + \bar{D}_3^x (S_u^x(\mathbf{R}, A) S_d^y(\mathbf{R} + \mathbf{a}_3, A) + S_u^y(\mathbf{R}, A) S_d^x(\mathbf{R} + \mathbf{a}_3, A)) \\
& + \bar{D}_{21}^x (S_u^x(\mathbf{R}, A) S_d^y(\mathbf{R} + \mathbf{a}_{21}, A) + S_u^y(\mathbf{R}, A) S_d^x(\mathbf{R} + \mathbf{a}_{21}, A)) \\
& + \bar{D}_{31}^x (S_u^x(\mathbf{R}, A) S_d^y(\mathbf{R} + \mathbf{a}_{31}, A) + S_u^y(\mathbf{R}, A) S_d^x(\mathbf{R} + \mathbf{a}_{31}, A)) \\
& + \bar{D}_{32}^x (S_u^x(\mathbf{R}, A) S_d^y(\mathbf{R} + \mathbf{a}_{32}, A) + S_u^y(\mathbf{R}, A) S_d^x(\mathbf{R} + \mathbf{a}_{32}, A)) \\
& - (u \leftrightarrow d) \\
& - (A \leftrightarrow B), \tag{D.5}
\end{aligned}$$

$$H_{\kappa} = -\kappa \sum_{i, s=u, d} (S_{i,s}^z)^2. \tag{D.6}$$

Here, we write the operators of up and down spins localized at the site  $i$  as  $\mathbf{S}_{i,u}$  and  $\mathbf{S}_{i,d}$ , respectively. In the case that the site  $i$  is on  $X$  ( $X = A, B$ ) sublattice in the unit cell

labeled by the lattice vector  $\mathbf{R}$ , we write another expression of  $\mathbf{S}_{i,s}$  ( $s = u, d$ ) as  $\mathbf{S}_s(\mathbf{R}, X)$  ( $s = u, d$ ). Here,  $\mathbf{a}_{ij}$  is given by  $\mathbf{a}_{ij} = \mathbf{a}_i - \mathbf{a}_j$ . We consider the two nearest-neighbor bond vectors traversed between sites  $(\mathbf{R}, A)$  and  $(\mathbf{R} + \mathbf{a}_i, A)$  ( $(\mathbf{R}, A)$  and  $(\mathbf{R} + \mathbf{a}_{ij}, A)$ ) [218], which is detailed in Fig. D1. By using them, the DM vector  $\mathbf{D}_i$  ( $\mathbf{D}_{ij}$ ) is given by  $\mathbf{D}_i = D(\mathbf{d}_i^1(\mathbf{R}) \times \mathbf{d}_i^2(\mathbf{R})) / |\mathbf{d}_i^1(\mathbf{R}) \times \mathbf{d}_i^2(\mathbf{R})|$  ( $\mathbf{D}_{ij} = D(\mathbf{d}_{ij}^1(\mathbf{R}) \times \mathbf{d}_{ij}^2(\mathbf{R})) / |\mathbf{d}_{ij}^1(\mathbf{R}) \times \mathbf{d}_{ij}^2(\mathbf{R})|$ ). We define the vectors  $\bar{\mathbf{D}}_i$  and  $\bar{\mathbf{D}}_{ij}$  as  $\bar{\mathbf{D}}_i = \mathbf{D}_i / D$  and  $\bar{\mathbf{D}}_{ij} = \mathbf{D}_{ij} / D$ , respectively.

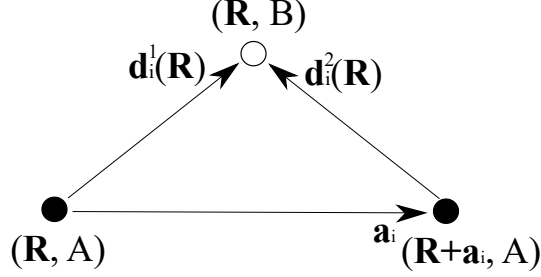


Fig. D1: Two nearest-neighbor bond vectors  $\mathbf{d}_i^1(\mathbf{R})$  and  $\mathbf{d}_i^2(\mathbf{R})$ . The site  $(\mathbf{R}, B)$  is the common nearest-neighbor site between two next nearest sites  $(\mathbf{R}, A)$  and  $(\mathbf{R} + \mathbf{a}_i, A)$ . The vectors  $\mathbf{d}_i^1(\mathbf{R})$  and  $\mathbf{d}_i^2(\mathbf{R})$  point to the site  $(\mathbf{R}, B)$  from  $(\mathbf{R}, A)$  and  $(\mathbf{R} + \mathbf{a}_i, A)$ , respectively.

By applying the Holstein-Primakoff and Fourier transformation, we can obtain the Hamiltonian which is written in the form as Eq. (2.40) with  $N = 2$ . The matrix  $H(\mathbf{k})$  is given by

$$H(\mathbf{k}) = \begin{pmatrix} h(\mathbf{k}) & \Delta^\dagger(\mathbf{k}) \\ \Delta(\mathbf{k}) & h^*(-\mathbf{k}) \end{pmatrix}. \quad (\text{D.7})$$

Here,  $4 \times 4$  matrices  $h(\mathbf{k})$  and  $\Delta(\mathbf{k})$  are written as follows:

$$h(\mathbf{k}) = d_0 1_4 + \sum_{a=1}^5 d_a(\mathbf{k}) \Gamma^a, \quad (\text{D.8})$$

$$\Delta(\mathbf{k}) = J' \sigma_x \otimes 1_2, \quad (\text{D.9})$$

where  $\Gamma^{(1,2,3,4,5)}$  as given by

$$\Gamma^{(1,2,3,4,5)} = (1_2 \otimes \sigma_x, 1_2 \otimes \sigma_y, \sigma_x \otimes \sigma_z, \sigma_y \otimes \sigma_z, \sigma_z \otimes \sigma_z). \quad (\text{D.10})$$

We note that these  $\Gamma$  matrices satisfy the standard anticommutation relations:  $\{\Gamma^{(i)}, \Gamma^{(j)}\} =$

$2\delta_{ij}1_4$ . Here,  $d_i$  ( $i = 0, 1, \dots, 5$ ) in Eq. (F.2) are written as

$$d_0 = J_0 + J_1 + J_2 + J_3 + J' + 2\kappa, \quad (\text{D.11})$$

$$d_1(\mathbf{k}) = -J_0 - J_1 \cos(k_1) - J_2 \cos(k_2) - J_3 \cos(k_3), \quad (\text{D.12})$$

$$d_2(\mathbf{k}) = -J_1 \sin(k_1) - J_2 \sin(k_2) - J_3 \sin(k_3), \quad (\text{D.13})$$

$$d_3(\mathbf{k}) = -\sqrt{2}\Gamma[\sin(k_2) - \sin(k_3) - \sin(k_{21}) + \sin(k_{31})], \quad (\text{D.14})$$

$$d_4(\mathbf{k}) = -\sqrt{2}J_-[\sin(k_3) - \sin(k_1) - \sin(k_{32}) + \sin(k_{12})], \quad (\text{D.15})$$

$$d_5(\mathbf{k}) = -\sqrt{2}D[\sin(k_1) - \sin(k_2) - \sin(k_{13}) + \sin(k_{23})]. \quad (\text{D.16})$$

Here,  $k_i$  and  $k_{ij}$  are defined as  $k_i = \mathbf{k} \cdot \mathbf{a}_i$  and  $k_{ij} = k_i - k_j$ , respectively. We write the three lattice prime vectors of the diamond lattice as  $\mathbf{a}_i$  ( $i = 1, 2, 3$ ). We can see that the pseudo-time-reversal symmetry (C.2) is satisfied by the Hamiltonian (D.7).

## Appendix E : The analytical expressions of energy eigenvalues

In this part, we show that in the case of  $\Gamma = 0$ , the energy spectrum of the Hamiltonian of the diamond lattice system (3.1) can be obtained analytically. By using the unitary matrix  $U(\mathbf{k})$  (details of  $U(\mathbf{k})$  are shown later),  $\Sigma_z H(\mathbf{k})$  can be written as follows:

$$U^\dagger(\mathbf{k})\Sigma_z H(\mathbf{k})U(\mathbf{k}) = \begin{pmatrix} 0 & Q_1(\mathbf{k}) \\ Q_2(\mathbf{k}) & 0 \end{pmatrix}, \quad (\text{E.1})$$

where  $Q_n(\mathbf{k})$  ( $n = 1, 2$ ) are defined by

$$Q_n(\mathbf{k}) = \begin{pmatrix} -d_0 & 0 & \lambda_{n,+}(\mathbf{k}) & 0 \\ 0 & -d_0 & 0 & \lambda_{n,-}(\mathbf{k}) \\ \lambda_{n,+}^*(\mathbf{k}) & 0 & -d_0 & 0 \\ 0 & \lambda_{n,-}^*(\mathbf{k}) & 0 & -d_0 \end{pmatrix}. \quad (\text{E.2})$$

Here  $\lambda_{n,\pm}(\mathbf{k})$  is written as

$$\lambda_{n,\pm}(\mathbf{k}) = -id_4(\mathbf{k}) + (-1)^n J' \pm \sqrt{d_5^2(\mathbf{k}) + |\gamma(\mathbf{k})|^2}. \quad (\text{E.3})$$

We note that the matrix  $U^\dagger(\mathbf{k})(\Sigma_z H(\mathbf{k}))^2 U(\mathbf{k})$ , whose eigenvalues are equal to the square of the ones of  $\Sigma_z H(\mathbf{k})$ , is the block diagonal:

$$\begin{aligned} U^\dagger(\mathbf{k})(\Sigma_z H(\mathbf{k}))^2 U(\mathbf{k}) &= (U^\dagger(\mathbf{k})\Sigma_z H(\mathbf{k})U(\mathbf{k}))^2 \\ &= \begin{pmatrix} Q_1(\mathbf{k})Q_2(\mathbf{k}) & 0 \\ 0 & Q_2(\mathbf{k})Q_1(\mathbf{k}) \end{pmatrix}. \end{aligned} \quad (\text{E.4})$$

The matrices  $Q_1(\mathbf{k})Q_2(\mathbf{k})$  and  $Q_2(\mathbf{k})Q_1(\mathbf{k})$  have the same eigenvalues, which correspond to the double eigenvalue  $E^2(\mathbf{k})$  of  $(\Sigma_z H(\mathbf{k}))^2$ . Here, we write the pair of eigenvalues of  $\Sigma_z H(\mathbf{k})$  as  $\pm E(\mathbf{k})$ . Therefore,  $E^2(\mathbf{k})$  can be obtained as the eigenvalues of  $Q_1(\mathbf{k})Q_2(\mathbf{k})$ :

$$Q_1(\mathbf{k})Q_2(\mathbf{k}) = \begin{pmatrix} q_1(\mathbf{k}) & q_2(\mathbf{k}) \\ q_2^*(\mathbf{k}) & q_1^*(\mathbf{k}) \end{pmatrix}, \quad (\text{E.5})$$

where the matrices  $q_1(\mathbf{k})$  and  $q_2(\mathbf{k})$  are given by

$$q_1(\mathbf{k}) = \begin{pmatrix} d_0^2 + \lambda_{1,+}(\mathbf{k})\lambda_{2,+}^*(\mathbf{k}) & 0 \\ 0 & d_0^2 + \lambda_{1,-}(\mathbf{k})\lambda_{2,-}^*(\mathbf{k}) \end{pmatrix}. \quad (\text{E.6})$$

$$q_2(\mathbf{k}) = \begin{pmatrix} -d_0(\lambda_{1,+}(\mathbf{k}) + \lambda_{2,+}(\mathbf{k})) & 0 \\ 0 & -d_0(\lambda_{1,-}(\mathbf{k}) + \lambda_{2,-}(\mathbf{k})) \end{pmatrix}. \quad (\text{E.7})$$

Since this matrix can be divided into two parts, the eigenvalues are calculated from the following equation:

$$\begin{vmatrix} d_0^2 + \lambda_{1,\pm}(\mathbf{k})\lambda_{2,\pm}^*(\mathbf{k}) - E^2(\mathbf{k}) & -d_0(\lambda_{1,\pm}(\mathbf{k}) + \lambda_{2,\pm}(\mathbf{k})) \\ -d_0(\lambda_{1,\pm}^*(\mathbf{k}) + \lambda_{2,\pm}^*(\mathbf{k})) & d_0^2 + \lambda_{1,\pm}^*(\mathbf{k})\lambda_{2,\pm}(\mathbf{k}) - E^2(\mathbf{k}) \end{vmatrix} = 0. \quad (\text{E.8})$$

Then, one has

$$E^2(\mathbf{k}) = d_0^2 + \text{Re}[\lambda_{1,\rho}(\mathbf{k})\lambda_{2,\rho}^*(\mathbf{k})] + \rho' \sqrt{(d_0^2 + \text{Re}[\lambda_{1,\rho}(\mathbf{k})\lambda_{2,\rho}^*(\mathbf{k})])^2 + d_0^2|\lambda_{1,\rho}(\mathbf{k}) + \lambda_{2,\rho}(\mathbf{k})|^2}, \quad (\text{E.9})$$

where  $\rho, \rho' = \pm$ . Finally, the eigenvalues of  $\Sigma_z H(\mathbf{k})$  are written as follows:

$$\begin{aligned} & E_{\rho_1, \rho_2, \rho_3}(\mathbf{k}) \\ &= \rho_1 \sqrt{d_0^2 + \text{Re}[\lambda_{1,\rho_1}(\mathbf{k})\lambda_{2,\rho_1}^*(\mathbf{k})] + \rho_3 \sqrt{(d_0^2 + \text{Re}[\lambda_{1,\rho_2}(\mathbf{k})\lambda_{2,\rho_2}^*(\mathbf{k})])^2 + d_0^2|\lambda_{1,\rho_2}(\mathbf{k}) + \lambda_{2,\rho_2}(\mathbf{k})|^2}}, \end{aligned} \quad (\text{E.10})$$

where  $\rho_1, \rho_2, \rho_3 = \pm$ . We note that due to the pseudo-time-reversal and inversion symmetry, these eigenvalues are doubly degenerate and satisfy  $E_{\rho_1, +, \rho_3}(\mathbf{k}) = E_{\rho_1, -, \rho_3}(\mathbf{k})$ .

In the following, we show how to construct the matrix  $U(\mathbf{k})$ . This is written as the product of three unitary matrices  $U_1, U_2$ , and  $U_3(\mathbf{k})$ , i.e.,  $U(\mathbf{k}) = U_1 U_2 U_3(\mathbf{k})$ . The first matrix  $U_1$  is the one which diagonalizes  $C := \sigma_y \otimes \sigma_y \otimes 1_2$ . Since  $C$  anticommutes with  $\Sigma_z H(\mathbf{k})$ ,  $U_1$  makes  $\Sigma_z H(\mathbf{k})$  off-diagonal:

$$U_1^\dagger \Sigma_z H(\mathbf{k}) U_1 = \begin{pmatrix} 0 & R_1(\mathbf{k}) \\ R_2(\mathbf{k}) & 0 \end{pmatrix}, \quad (\text{E.11})$$

where

$$R_1(\mathbf{k}) = \begin{pmatrix} -d_0 + d_5(\mathbf{k}) + J' & \gamma(\mathbf{k}) & id_4(\mathbf{k}) & 0 \\ -\gamma^*(\mathbf{k}) & -d_0 - d_5(\mathbf{k}) + J' & 0 & -id_4(\mathbf{k}) \\ -id_4(\mathbf{k}) & 0 & -d_0 - d_5(\mathbf{k}) - J' & \gamma(\mathbf{k}) \\ 0 & id_4(\mathbf{k}) & -\gamma^*(\mathbf{k}) & -d_0 + d_5(\mathbf{k}) - J' \end{pmatrix}, \quad (\text{E.12})$$

$$R_2(\mathbf{k}) = \begin{pmatrix} -d_0 + d_5(\mathbf{k}) - J' & \gamma(\mathbf{k}) & id_4(\mathbf{k}) & 0 \\ -\gamma^*(\mathbf{k}) & -d_0 - d_5(\mathbf{k}) - J' & 0 & -id_4(\mathbf{k}) \\ -id_4(\mathbf{k}) & 0 & -d_0 - d_5(\mathbf{k}) + J' & \gamma(\mathbf{k}) \\ 0 & id_4(\mathbf{k}) & -\gamma^*(\mathbf{k}) & -d_0 + d_5(\mathbf{k}) + J' \end{pmatrix}. \quad (\text{E.13})$$

The second matrix is given by  $U_2 = 1_2 \otimes u$ . Here  $u$  is a  $4 \times 4$  matrix and diagonalizes  $c := \sigma_x \otimes \sigma_z$  which anticommutes with  $d_0 1_4 + R_{1,2}(\mathbf{k})$ . By the unitary transformation using  $u$ ,  $d_0 1_4 + R_{1,2}(\mathbf{k})$  becomes off-diagonal:

$$u^\dagger(d_0 1_4 + R_1(\mathbf{k}))u = \begin{pmatrix} 0 & r_{11}(\mathbf{k}) \\ r_{12}(\mathbf{k}) & 0 \end{pmatrix}, \quad (\text{E.14})$$

$$u^\dagger(d_0 1_4 + R_2(\mathbf{k}))u = \begin{pmatrix} 0 & r_{21}(\mathbf{k}) \\ r_{22}(\mathbf{k}) & 0 \end{pmatrix}, \quad (\text{E.15})$$

where

$$r_{11}(\mathbf{k}) = r_{12}^\dagger(\mathbf{k}) = \begin{pmatrix} d_5(\mathbf{k}) - id_4(\mathbf{k}) - J' & \gamma^*(\mathbf{k}) \\ \gamma(\mathbf{k}) & -d_5(\mathbf{k}) - id_4(\mathbf{k}) - J' \end{pmatrix}, \quad (\text{E.16})$$

$$r_{21}(\mathbf{k}) = r_{22}^\dagger(\mathbf{k}) = \begin{pmatrix} d_5(\mathbf{k}) - id_4(\mathbf{k}) + J' & \gamma^*(\mathbf{k}) \\ \gamma(\mathbf{k}) & -d_5(\mathbf{k}) - id_4(\mathbf{k}) + J' \end{pmatrix}. \quad (\text{E.17})$$

Since  $r_{ij}(\mathbf{k})$  ( $i, j = 1, 2$ ) commute with each other, they are diagonalized by the same unitary matrix  $v(\mathbf{k})$  as follows:

$$v^\dagger(\mathbf{k})r_{n1}(\mathbf{k})v(\mathbf{k}) = \begin{pmatrix} \lambda_{n,+}(\mathbf{k}) & 0 \\ 0 & \lambda_{n,-}(\mathbf{k}) \end{pmatrix}, \quad (\text{E.18})$$

$$v^\dagger(\mathbf{k})r_{n2}(\mathbf{k})v(\mathbf{k}) = \begin{pmatrix} \lambda_{n,+}^*(\mathbf{k}) & 0 \\ 0 & \lambda_{n,-}^*(\mathbf{k}) \end{pmatrix} \quad (n = 1, 2). \quad (\text{E.19})$$

By using  $v(\mathbf{k})$ , the third matrix  $U_3(\mathbf{k})$  is defined as  $U_3(\mathbf{k}) = 1_4 \otimes v(\mathbf{k})$ . Now we can construct the matrix  $U(\mathbf{k})$  and obtain the unitary-transformed Hamiltonian Eq. (E.1).

## Appendix F : Explicit expression of Hamiltonian matrix in Eq. (4.2)

In this part, we give the detailed expression of the matrix  $H(\mathbf{k})$  in the Hamiltonian (4.2), which is proposed as a model for MAFTI. The general form of the Hamiltonian for noninteracting bosons are written as follows:

$$H(\mathbf{k}) = \begin{pmatrix} h(\mathbf{k}) & \Delta^\dagger(\mathbf{k}) \\ \Delta(\mathbf{k}) & h^*(-\mathbf{k}) \end{pmatrix}. \quad (\text{F.1})$$

In the case of model (4.2),  $h(\mathbf{k})$  and  $\Delta(\mathbf{k})$  are  $4 \times 4$  matrices and given by

$$h(\mathbf{k}) = \begin{pmatrix} d + p(\mathbf{k}) & -\gamma_+(\mathbf{k}) & 0 & 0 \\ -\gamma_+^*(\mathbf{k}) & d - p(\mathbf{k}) & 0 & 0 \\ 0 & 0 & d - p(\mathbf{k}) & -\gamma_+(\mathbf{k}) \\ 0 & 0 & -\gamma_+^*(\mathbf{k}) & d + p(\mathbf{k}) \end{pmatrix}, \quad (\text{F.2})$$

$$\Delta(\mathbf{k}) = \begin{pmatrix} 0 & -\gamma_-(\mathbf{k}) & \gamma_z^*(k_3) & 0 \\ -\gamma_-^*(\mathbf{k}) & 0 & 0 & \gamma_z^*(k_3) \\ \gamma_z(k_3) & 0 & 0 & -\gamma_-(\mathbf{k}) \\ 0 & \gamma_z(k_3) & -\gamma_-^*(\mathbf{k}) & 0 \end{pmatrix}, \quad (\text{F.3})$$

where

$$d = J_0^z S + J_1^z S + J_2^z S + 2J' S, \quad (\text{F.4})$$

$$p(\mathbf{k}) = 2DS [\sin(k_1) - \sin(k_2) - \sin(k_1 - k_2)], \quad (\text{F.5})$$

$$\gamma_{\pm}(\mathbf{k}) = J_0^{\pm} S + J_1^{\pm} S e^{ik_1} + J_2^{\pm} S e^{ik_2}, \quad (\text{F.6})$$

$$\gamma_z(k_3) = J' S (1 + e^{ik_3}). \quad (\text{F.7})$$

Here  $S$ ,  $k_i$ , and  $J_i^{\pm}$  are the spin magnitude,  $k_i = \mathbf{k} \cdot \mathbf{a}_i$ , and  $J_n^{\pm} = (J_n^x \pm J_n^y)/2$ , respectively.

## Appendix G : The derivation of the effective Hamiltonian for the surface

In this part, we derive the effective Hamiltonian of the surface of the system. Let us consider the projection onto the subspace of two (particle) bands above and below the Dirac point we focus on. We define the set of the wave functions of these bands as

$$|\Psi(\bar{\mathbf{k}})\rangle = [|\Psi_1(\bar{\mathbf{k}})\rangle, S_{1/2}(k_z) |\Psi_1(\bar{\mathbf{k}})\rangle, |\Psi_2(\bar{\mathbf{k}})\rangle, S_{1/2}(k_z) |\Psi_2(\bar{\mathbf{k}})\rangle], \quad (\text{G.1})$$

where  $|\Psi_{1(2)}(\bar{\mathbf{k}})\rangle$  is the eigenvectors of the lower (higher) band. Since we consider up to first order of  $k_z - \pi$ , the operator  $S_{1/2}(k_z)$  can be replaced with  $S_{1/2}(\pi)$ . The Hamiltonian projected onto this subspace is a  $4 \times 4$  matrix and written as

$$H_1(\bar{\mathbf{k}}) = \langle \Psi(\bar{\mathbf{k}}) | H(\bar{\mathbf{k}}) | \Psi(\bar{\mathbf{k}}) \rangle. \quad (\text{G.2})$$

Expanding the Hamiltonian  $H_1(\bar{\mathbf{k}})$  to the second order in  $k_x$  and the first order in  $(k_y - \pi)$  and  $(k_z - \pi)$ , we denote the terms depending on  $(k_y - \pi)$  or  $(k_z - \pi)$  as  $H_{yz}(\bar{\mathbf{k}})$ . The other terms are denoted by  $H_x(k_x)$ . We write the energy of the center of the Dirac cone as  $E_0$ . The state  $\psi(x)$  which is localized on the (100) surface is obtained as the eigenvector of the Hamiltonian  $H_x(-i\partial_x)$  with the eigenvalue  $E_0$ :

$$H_x(-i\partial_x)\psi(x) = E_0\psi(x). \quad (\text{G.3})$$

Here we take  $\psi(x)$  as

$$\psi(x) = \psi_0 e^{\lambda x}. \quad (\text{G.4})$$

The parameter  $\lambda$  is obtained by solving

$$\text{Det}(H_x(-i\lambda) - E_0 1_4) = 0. \quad (\text{G.5})$$

This is an eighth order equation in  $\lambda$  and has eight solutions. Four of them are positive and the other are negative. The negative solutions correspond to states localized on the ( $\bar{1}00$ ) surface. Here we focus on the positive solutions corresponding to states localized on the (100) surface. Due to the S-symmetry, each two of the eight solutions are the same. Thus, we write two positive solutions as  $\lambda_1$  and  $\lambda_2$  and define the corresponding two constant

vectors as  $\boldsymbol{\psi}_1$  and  $\boldsymbol{\psi}_2$ . The combined operator in the subspace of first and second bands is defined as  $S_{1/2}(k_z) = \Theta T_{1/2}(k_z)$ , where  $\Theta = K$  and  $T_{1/2}(k_z) = \sigma_x \text{diag}(1, e^{ik_z}) \otimes \mathbf{1}_2$ , respectively. The vectors  $S_{1/2}(\pi)\boldsymbol{\psi}_1$  and  $S_{1/2}(\pi)\boldsymbol{\psi}_2$  are also the solutions with  $\lambda_1$  and  $\lambda_2$ , respectively. Then the wave function which satisfies Eq. (G.3) is generally written as

$$\boldsymbol{\psi}(z) = (\alpha_1 \boldsymbol{\psi}_1 + \beta_1 S_{1/2}(\pi)\boldsymbol{\psi}_1) e^{\lambda_1 x} + (\alpha_2 \boldsymbol{\psi}_2 + \beta_2 S_{1/2}(\pi)\boldsymbol{\psi}_2) e^{\lambda_2 x}. \quad (\text{G.6})$$

Since  $\lambda_{1,2} > 0$ , this satisfies the condition  $\boldsymbol{\psi}(-\infty) = 0$ . Using the other boundary condition that the wave function vanishes on the surface  $x = 0$ , i.e.  $\boldsymbol{\psi}(0) = 0$ , we obtain four simultaneous equations for the coefficient  $\alpha_1, \beta_1, \alpha_2$  and  $\beta_2$ :

$$(\boldsymbol{\psi}_1, S_{1/2}(\pi)\boldsymbol{\psi}_1, \boldsymbol{\psi}_2, S_{1/2}(\pi)\boldsymbol{\psi}_2) \begin{pmatrix} \alpha_1 \\ \beta_1 \\ \alpha_2 \\ \beta_2 \end{pmatrix} = 0. \quad (\text{G.7})$$

Since the determinant of the matrix  $(\boldsymbol{\psi}_1, S_{1/2}(\pi)\boldsymbol{\psi}_1, \boldsymbol{\psi}_2, S_{1/2}(\pi)\boldsymbol{\psi}_2)$  is zero, the above equation has a nontrivial solution. The overall factor of the four coefficients  $\alpha_1, \beta_1, \alpha_2$  and  $\beta_2$  is determined by the normalization condition:

$$\int_{-\infty}^0 dx |\boldsymbol{\psi}(x)|^2 = 1. \quad (\text{G.8})$$

From the coefficients obtained, we have the effective surface Hamiltonian

$$H_{\text{eff}}(\bar{\mathbf{k}}) = \begin{pmatrix} \langle \boldsymbol{\psi} | H_{yz}(\bar{\mathbf{k}}) | \boldsymbol{\psi} \rangle + E_0 & \langle \boldsymbol{\psi} | H_{yz}(\bar{\mathbf{k}}) | S_{1/2}(\pi)\boldsymbol{\psi} \rangle \\ \langle S_{1/2}(\pi)\boldsymbol{\psi} | H_{yz}(\bar{\mathbf{k}}) | \boldsymbol{\psi} \rangle & \langle S_{1/2}(\pi)\boldsymbol{\psi} | H_{yz}(\bar{\mathbf{k}}) | S_{1/2}(\pi)\boldsymbol{\psi} \rangle + E_0 \end{pmatrix}, \quad (\text{G.9})$$

where the matrix element  $\langle \boldsymbol{\psi} | H_{yz}(\bar{\mathbf{k}}) | \boldsymbol{\psi} \rangle$  is defined as

$$\langle \boldsymbol{\psi} | H_{yz}(\bar{\mathbf{k}}) | \boldsymbol{\psi} \rangle = \int_{-\infty}^0 dx \boldsymbol{\psi}^\dagger(x) H_{yz}(\bar{\mathbf{k}}) \boldsymbol{\psi}(x). \quad (\text{G.10})$$

The other three matrix elements are defined similarly.

## Appendix H : Expression of energy current

In this part, the explicit expression of the energy current operator  $J_x$  in Eq. (4.9) is discussed. Here, the open (periodic) boundary conditions in the direction(s) along  $\mathbf{a}_1$  ( $\mathbf{a}_2$  and  $\mathbf{a}_3$ ), are considered. When we apply the Holstein-Primakoff transformation and Fourier transformation along with the  $\mathbf{a}_2$  and  $\mathbf{a}_3$  directions, the Hamiltonian (4.1) is written as follows:

$$H = \frac{1}{2} \sum_{\bar{\mathbf{k}}} \boldsymbol{\psi}^\dagger(\bar{\mathbf{k}}) H(\bar{\mathbf{k}}) \boldsymbol{\psi}(\bar{\mathbf{k}}). \quad (\text{H.1})$$

The operator  $\psi(\bar{\mathbf{k}})$  is defined by Eqs. (I.4) and (I.8). We define the position operator in the  $x$ -direction as follows:

$$P = \frac{1}{2} \sum_{\bar{\mathbf{k}}} \psi^\dagger(\bar{\mathbf{k}}) \bar{P} \psi(\bar{\mathbf{k}}). \quad (\text{H.2})$$

Here,  $\bar{P}$  is an  $8N \times 8N$  diagonal matrix whose components are given by

$$\begin{aligned} \bar{P}_{4n+1,4n+1} &= \bar{P}_{4n+3,4n+3} = \bar{P}_{4(n+N)+1,4(n+N)+1} = \bar{P}_{4(n+N)+3,4(n+N)+3} \\ &= \frac{\sqrt{3}}{2}(n-1) - \frac{1}{2} \left( \frac{\sqrt{3}}{2}(N-1) + \frac{1}{2\sqrt{3}} \right), \end{aligned} \quad (\text{H.3})$$

$$\begin{aligned} \bar{P}_{4n+2,4n+2} &= \bar{P}_{4n+4,4n+4} = \bar{P}_{4(n+N)+2,4(n+N)+2} = \bar{P}_{4(n+N)+4,4(n+N)+4} \\ &= \frac{\sqrt{3}}{2}(n-1) - \frac{1}{2} \left( \frac{\sqrt{3}}{2}(N-1) - \frac{1}{2\sqrt{3}} \right). \end{aligned} \quad (\text{H.4})$$

We also define the Hamiltonian density at site  $i$  and its time derivative as follows:

$$h_i = \frac{1}{2} \sum_{\bar{\mathbf{k}}} \sum_j \psi_i^\dagger(\bar{\mathbf{k}}) H_{ij}(\bar{\mathbf{k}}) \psi_j(\bar{\mathbf{k}}). \quad (\text{H.5})$$

$$\dot{h}_i = i[H, h_i], \quad (\text{H.6})$$

The energy current operator  $J_x$  in Eq. (4.9) is defined by using these  $\bar{P}$  and  $\dot{h}_i$ . We can rewrite the energy current operator  $J_x$  as follows:

$$J_x = -\frac{i}{4} \sum_{\bar{\mathbf{k}}} \psi^\dagger(\bar{\mathbf{k}}) \left( \bar{P} H(\bar{\mathbf{k}}) \Sigma_z H(\bar{\mathbf{k}}) - H(\bar{\mathbf{k}}) \Sigma_z H(\bar{\mathbf{k}}) \bar{P} \right) \psi(\bar{\mathbf{k}}), \quad (\text{H.7})$$

where  $\Sigma_z = \sigma_z \otimes 1_{4N}$ . Thus, a matrix  $J_x(\bar{\mathbf{k}})$  is defined as

$$J_x(\bar{\mathbf{k}}) = -\frac{i}{2} \left( \bar{P} H(\bar{\mathbf{k}}) \Sigma_z H(\bar{\mathbf{k}}) - H(\bar{\mathbf{k}}) \Sigma_z H(\bar{\mathbf{k}}) \bar{P} \right). \quad (\text{H.8})$$

## Appendix I : Expression of perturbation term due to an electric field

In this part, we explain the details of the perturbation Hamiltonian  $H_E$ , which is introduced to evaluate the energy current using the linear response theory in the Sec. 4.2 and 4.3. Here, same boundary conditions as in Appendix G, i.e., the open (periodic) boundary conditions in the direction(s) along  $\mathbf{a}_1$  ( $\mathbf{a}_2$  and  $\mathbf{a}_3$ ), are considered. We write the magnon BdG Hamiltonian in an applied electric field as follows:

$$H = \sum_{ij} \left( h_{ij}(E_x) b_i^\dagger b_j + \Delta_{ij}(E_x) b_i b_j \right) + h.c.. \quad (\text{I.1})$$

When an AC electric field has a frequency  $\omega$  as  $\mathbf{E} = E_x e^{-i\omega t} \mathbf{e}_x$ , the first-order perturbation Hamiltonian can be expressed as  $H_E(t) = H_E e^{-i\omega t}$ , where  $H_E$  is given by

$$H_E = \sum_{ij} \left( E_x \left[ \frac{\partial}{\partial E_x} h_{ij}(E_x) \right]_{E_x=0} b_i^\dagger b_j + E_x \left[ \frac{\partial}{\partial E_x} \Delta_{ij}(E_x) \right]_{E_x=0} b_i b_j \right) + h.c.. \quad (\text{I.2})$$

We take the open (periodic) boundary conditions in the direction(s) along  $\mathbf{a}_1$  ( $\mathbf{a}_2$  and  $\mathbf{a}_3$ ). The Hamiltonian after applying the Holstein-Primakoff transformation and Fourier transformation along the  $\mathbf{a}_2$  and  $\mathbf{a}_3$  directions is written as follows:

$$H_E = \frac{1}{2} \sum_{\bar{\mathbf{k}}} \psi^\dagger(\bar{\mathbf{k}}) H_E(\bar{\mathbf{k}}) \psi(\bar{\mathbf{k}}), \quad (\text{I.3})$$

where  $\psi(\bar{\mathbf{k}})$  is given by

$$\psi(\bar{\mathbf{k}}) = (\mathbf{b}(\bar{\mathbf{k}}), \mathbf{b}^\dagger(-\bar{\mathbf{k}}))^T. \quad (\text{I.4})$$

When the number of unit cells in the  $x$ -direction is  $N$ , the operator  $\mathbf{b}(\bar{\mathbf{k}})$ , the number of components of the operator  $\mathbf{b}(\bar{\mathbf{k}})$  is  $4N$ . By using  $b_j(\bar{\mathbf{k}}, A(B), 1(2))$ , which is the annihilation operator of magnons at the sublattice  $A(B)$  in the  $j$ th unit cell on the layer with odd (even)  $l$ , they are written as follows:

$$b_{4n+1}(\bar{\mathbf{k}}) = b_n(\bar{\mathbf{k}}, A, 1), \quad (\text{I.5})$$

$$b_{4n+2}(\bar{\mathbf{k}}) = b_n(\bar{\mathbf{k}}, B, 1), \quad (\text{I.6})$$

$$b_{4n+3}(\bar{\mathbf{k}}) = b_n(\bar{\mathbf{k}}, A, 2), \quad (\text{I.7})$$

$$b_{4n+4}(\bar{\mathbf{k}}) = b_n(\bar{\mathbf{k}}, B, 2). \quad (\text{I.8})$$

The matrix  $H_E(\bar{\mathbf{k}})$  in Eq. (I.3) is given by

$$H_E(\bar{\mathbf{k}}) = \begin{pmatrix} h_E(\bar{\mathbf{k}}) & \Delta_E^\dagger(\bar{\mathbf{k}}) \\ \Delta_E(\bar{\mathbf{k}}) & h_E^*(-\bar{\mathbf{k}}) \end{pmatrix}. \quad (\text{I.9})$$

Here, the matrices  $h_E(\bar{\mathbf{k}})$  and  $\Delta_E(\bar{\mathbf{k}})$  are written as follows:

$$h_E(\bar{\mathbf{k}}) = \begin{pmatrix} h_{E1}(\bar{\mathbf{k}}) & h_{E2}(\bar{\mathbf{k}}) & 0 & 0 \\ h_{E2}^\dagger(\bar{\mathbf{k}}) & \ddots & \ddots & 0 \\ 0 & \ddots & \ddots & h_{E2}(\bar{\mathbf{k}}) \\ 0 & 0 & h_{E2}^\dagger(\bar{\mathbf{k}}) & h_{E1}(\bar{\mathbf{k}}) \end{pmatrix}, \quad (\text{I.10})$$

$$\Delta_E(\bar{\mathbf{k}}) = \begin{pmatrix} \Delta_{E1}(\bar{\mathbf{k}}) & \Delta_{E2}(\bar{\mathbf{k}}) & 0 & 0 \\ \Delta_{E2}(-\bar{\mathbf{k}}) & \ddots & \ddots & 0 \\ 0 & \ddots & \ddots & \Delta_{E2}(\bar{\mathbf{k}}) \\ 0 & 0 & \Delta_{E2}(-\bar{\mathbf{k}}) & \Delta_{E1}(\bar{\mathbf{k}}) \end{pmatrix}. \quad (\text{I.11})$$

Here, the matrices  $h_{E1}(\bar{\mathbf{k}})$ ,  $h_{E2}(\bar{\mathbf{k}})$ ,  $\Delta_{E1}(\bar{\mathbf{k}})$ , and  $\Delta_{E2}(\bar{\mathbf{k}})$  for the model (4.1) are given by

$$h_{E1}(\bar{\mathbf{k}}) = S \begin{pmatrix} 2D \cos(k_2) & iJ_2^+ e^{ik_2} & 0 & 0 \\ -iJ_2^+ e^{-ik_2} & -2D \cos(k_2) & 0 & 0 \\ 0 & 0 & -2D \cos(k_2) & -iJ_2^+ e^{ik_2} \\ 0 & 0 & iJ_2^+ e^{-ik_2} & 2D \cos(k_2) \end{pmatrix}, \quad (\text{I.12})$$

$$h_{E2}(\bar{\mathbf{k}}) = S \begin{pmatrix} -D(1 + e^{-ik_2}) & \frac{i}{2}J_1^+ & 0 & 0 \\ 0 & D(1 + e^{-ik_2}) & 0 & 0 \\ 0 & 0 & -D(1 + e^{-ik_2}) & -\frac{i}{2}J_1^+ \\ 0 & 0 & 0 & D(1 + e^{-ik_2}) \end{pmatrix}. \quad (\text{I.13})$$

$$\Delta_{E1}(\bar{\mathbf{k}}) = 0, \quad (\text{I.14})$$

$$\Delta_{E2}(\bar{\mathbf{k}}) = 0. \quad (\text{I.15})$$

In the case of the model (4.14) for CrI<sub>3</sub>, these matrices are given by

$$h_{E1}(\bar{\mathbf{k}}) = S \begin{pmatrix} 2D \cos(k_2) & iJ e^{ik_2} & 0 & 0 \\ -iJ e^{-ik_2} & -2D \cos(k_2) & 0 & 0 \\ 0 & 0 & -2D \cos(k_2) & -iJ e^{ik_2} \\ 0 & 0 & iJ e^{-ik_2} & 2D \cos(k_2) \end{pmatrix}, \quad (\text{I.16})$$

$$h_{E2}(\bar{\mathbf{k}}) = S \begin{pmatrix} -D(1 + e^{-ik_2}) & \frac{i}{2}J + \frac{i}{4}K & 0 & 0 \\ 0 & D(1 + e^{-ik_2}) & 0 & 0 \\ 0 & 0 & -D(1 + e^{-ik_2}) & -\frac{i}{2}J - \frac{i}{4}K \\ 0 & 0 & 0 & D(1 + e^{-ik_2}) \end{pmatrix}, \quad (\text{I.17})$$

$$\Delta_{E1}(\bar{\mathbf{k}}) = S \begin{pmatrix} 0 & 0 & \frac{i}{6}J'(-1 + e^{-ik_3}) & -\frac{i}{3}J' e^{-ik_2} \\ 0 & 0 & \frac{i}{6}J' e^{i(k_2 - k_3)} & \frac{i}{6}J'(-1 + e^{-ik_3}) \\ \frac{i}{6}J'(-1 + e^{ik_3}) & \frac{i}{6}J' e^{i(-k_2 + k_3)} & 0 & 0 \\ -\frac{i}{3}J' e^{ik_2} & \frac{i}{6}J'(-1 + e^{ik_3}) & 0 & 0 \end{pmatrix}, \quad (\text{I.18})$$

$$\Delta_{E2}(\bar{\mathbf{k}}) = S \begin{pmatrix} 0 & 0 & 0 & 0 \\ 0 & 0 & \frac{i}{3}J' & 0 \\ 0 & 0 & 0 & 0 \\ -\frac{i}{6}J' e^{ik_3} & 0 & 0 & 0 \end{pmatrix}. \quad (\text{I.19})$$

## Appendix J : Magnon Hamiltonian of CrI<sub>3</sub>

In Sec. 4.3, we discuss the realization of MAFTI in a van der Waals magnet CrI<sub>3</sub> with the spin Hamiltonian Eq. (4.14). The Hamiltonian of magnons is the same form as Eq. (F.1). In this part, we give an explicit expression for the Hamiltonian. In the case of CrI<sub>3</sub> [155],

the matrices  $h(\mathbf{k})$  and  $\Delta(\mathbf{k})$  in Eq. (F.1) are given by

$$h(\mathbf{k}) = \begin{pmatrix} d + p(\mathbf{k}) & \gamma^*(\mathbf{k}) & 0 & 0 \\ \gamma(\mathbf{k}) & d - p(\mathbf{k}) & 0 & 0 \\ 0 & 0 & d - p(\mathbf{k}) & \gamma^*(\mathbf{k}) \\ 0 & 0 & \gamma(\mathbf{k}) & d + p(\mathbf{k}) \end{pmatrix}, \quad (\text{J.1})$$

$$\Delta(\mathbf{k}) = \begin{pmatrix} 0 & \gamma_{K\Gamma}(-\mathbf{k}) & \gamma_3(-\mathbf{k}) & \gamma_{21}(-\mathbf{k}) \\ \gamma_{K\Gamma}(\mathbf{k}) & 0 & \gamma_{12}(-\mathbf{k}) & \gamma_3(-\mathbf{k}) \\ \gamma_3(\mathbf{k}) & \gamma_{12}(\mathbf{k}) & 0 & \gamma_{K\Gamma}^*(\mathbf{k}) \\ \gamma_{21}(\mathbf{k}) & \gamma_3(\mathbf{k}) & \gamma_{K\Gamma}^*(-\mathbf{k}) & 0 \end{pmatrix}, \quad (\text{J.2})$$

where

$$d = 3JS + 4J'S - KS, \quad (\text{J.3})$$

$$p(\mathbf{k}) = 2DS [\sin(k_1) - \sin(k_2) - \sin(k_1 - k_2)], \quad (\text{J.4})$$

$$\gamma(\mathbf{k}) = -JS (1 + e^{-ik_1} + e^{-ik_2}) + \frac{KS}{2} (1 - e^{-ik_1}), \quad (\text{J.5})$$

$$\gamma_{K\Gamma}(\mathbf{k}) = \frac{KS}{2} (1 + e^{-ik_1}) - i\Gamma S e^{-ik_2}, \quad (\text{J.6})$$

$$\gamma_3(\mathbf{k}) = J'S (1 + e^{ik_3}), \quad (\text{J.7})$$

$$\gamma_{21}(\mathbf{k}) = J'S (e^{ik_2} + e^{i(k_1+k_3)}), \quad (\text{J.8})$$

$$\gamma_{12}(\mathbf{k}) = J'S (e^{-ik_1} + e^{i(-k_2+k_3)}). \quad (\text{J.9})$$

# Bibliography

- [1] D. J. Thouless, M. Kohmoto, M. P. Nightingale, and M. den Nijs, *Phys. Rev. Lett.* **49**, 405 (1982).
- [2] K. v. Klitzing, G. Dorda, and M. Pepper, *Phys. Rev. Lett.* **45**, 494 (1980).
- [3] M. Kohmoto, *Ann. Phys. (N.Y.)* **160**, 343 (1985).
- [4] D. C. Tsui, H. L. Stormer, and A. C. Gossard, *Phys. Rev. Lett.* **48**, 1559 (1982).
- [5] R. B. Laughlin, *Phys. Rev. Lett.* **50**, 1395 (1983).
- [6] Y. Hatsugai, *Phys. Rev. Lett.* **71**, 3697 (1993).
- [7] Y. Hatsugai, *Phys. Rev. B* **48**, 11851 (1993).
- [8] F. D. Haldane, *Phys. Rev. Lett.* **61**, 2015 (1988).
- [9] C. L. Kane and E. J. Mele, *Phys. Rev. Lett.* **95**, 226801 (2005).
- [10] C. L. Kane and E. J. Mele, *Phys. Rev. Lett.* **95**, 146802 (2005).
- [11] B. A. Bernevig, T. L. Hughes, and S.-C. Zhang, *Science* **314**, 1757 (2006).
- [12] M. König, S. Wiedmann, C. Brüne, A. Roth, H. Buhmann, L. W. Molenkamp, X.-L. Qi, and S.-C. Zhang, *Science* **318**, 766 (2007).
- [13] L. Fu and C. L. Kane, *Phys. Rev. B* **74**, 195312 (2006).
- [14] L. Sheng, D. N. Sheng, C. S. Ting, and F. D. M. Haldane *Phys. Rev. Lett.* **95** 136602 (2005).
- [15] D. N. Sheng, Z. Y. Weng, L. Sheng, and F. D. M. Haldane *Phys. Rev. Lett.* **97**, 036808 (2006).
- [16] L. Fu, C. L. Kane, and E. J. Mele, *Phys. Rev. Lett.* **98**, 106803 (2007).
- [17] M. Z. Hasan and C. L. Kane, *Rev. Mod. Phys.* **82**, 3045 (2010).
- [18] X. L. Qi and S. C. Zhang, *Rev. Mod. Phys.* **83**, 1057 (2011).

- [19] T. Fukui and Y. Hatsugai, *J. Phys. Soc. Jpn.* **76**, 053702 (2007).
- [20] J. E. Moore and L. Balents, *Phys. Rev. B* **75**, 121306 (2007).
- [21] R. Roy, *Phys. Rev. B* **79**, 195322 (2009).
- [22] H.-M. Guo and M. Franz, *Phys. Rev. Lett.* **103**, 206805 (2009).
- [23] C. Weeks and M. Franz, *Phys. Rev. B* **82**, 085310 (2010).
- [24] D. Hsieh, D. Qian, L. Wray, Y. Xia, Y. S. Hor, R. J. Cava, and M. Z. Hasan, *Nature* **452**, 970 (2008).
- [25] H. Zhang, C.-X. Liu, X.-L. Qi, X. Dai, Z. Fang, and S.-C. Zhang, *Nat. Phys.* **5**, 438 (2009).
- [26] Y. Xia, D. Qian, D. Hsieh, L. Wray, A. Pal, H. Lin, A. Bansil, D. Grauer, Y. S. Hor, R. J. Cava, and M. Z. Hasan, *Nat. Phys.* **5**, 398 (2009).
- [27] C. Jozwiak, Y. L. Chen, A. V. Fedorov, J. G. Analytis, C. R. Rotundu, A. K. Schmid, J. D. Denlinger, Y.-D. Chuang, D.-H. Lee, I. R. Fisher, R. J. Birgeneau, Z.-X. Shen, Z. Hussain, and A. Lanzara *Phys. Rev. B* **84**, 165113 (2011).
- [28] X. L. Qi, T. L. Hughes, and S. C. Zhang, *Phys. Rev. B* **78**, 195424 (2008).
- [29] X. L. Qi, R. Li, J. Zang, and S. C. Zhang, *Science* **323**, 1184 (2009).
- [30] K. Nomura and N. Nagaosa, *Phys. Rev. Lett.* **106**, 166802 (2011).
- [31] T. Morimoto, A. Furusaki, and N. Nagaosa, *Phys. Rev. B* **92**, 245121 (2016).
- [32] L. Fu, *Phys. Rev. Lett.* **106**, 106802 (2011).
- [33] K. Shiozaki and M. Sato, *Phys. Rev. B* **90**, 165114 (2014).
- [34] T. H. Hsieh, H. Lin, J. Liu, W. Duan, A. Bansil and L. Fu, *Nat. Commun.* **3**, 982 (2012).
- [35] Y. Tanaka, Z. Ren, T. Sato, K. Nakayama, S. Souma, T. Takahashi, K. Segawa and Y. Ando, *Nat. Phys.* **8**, 800–803 (2012).
- [36] P. Dziawa, B. J. Kowalski, K. Dybko, R. Buczko, A. Szczerbakow, M. Szot, E. Łusakowska, T. Balasubramanian, B. M. Wojek, M. H. Berntsen, O. Tjernberg and T. Story, *Nat. Mater.* **11**, 1023–1027 (2012).
- [37] S.-Y. Xu, C. Liu, N. Alidoust, M. Neupane, D. Qian, I. Belopolski, J. D. Denlinger, Y. J. Wang, H. Lin, L. A. Wray, G. Landolt, B. Slomski, J. H. Dil, A. Marcinkova, E. Morosan, Q. Gibson, R. Sankar, F. C. Chou, R. J. Cava, A. Bansil, and M. Z. Hasan, *Nat. Commun.* **3**, 1192 (2012).

- [38] R. S. K. Mong, A. M. Essin, and J. E. Moore, *Phys. Rev. B.* **81**, 245209 (2010).
- [39] I. Sodemann and L. Fu, *Phys. Rev. Lett.* **115**, 216806 (2015).
- [40] Z. Z. Du, C. M. Wang, H.-Z. Lu, and X. C. Xie, *Phys. Rev. Lett.* **121**, 266601 (2018).
- [41] R. Battilomo, N. Scopigno, and C. Ortix, *Phys. Rev. Lett.* **123**, 196403 (2019).
- [42] J. Son, K.-H. Kim, Y. H. Ahn, H.-W. Lee, and J. Lee, *Phys. Rev. Lett.* **123**, 036806 (2019).
- [43] J.-S. You, S. Fang, S.-Y. Xu, E. Kaxiras, and T. Low, *Phys. Rev. B* **98**, 121109(R) (2018).
- [44] Y. Zhang, Y. Sun, and B. Yan, *Phys. Rev. B* **97**, 041101(R) (2018).
- [45] S.-Y. Xu, Q. Ma, H. Shen, V. Fatemi, S. Wu, T.-R. Chang, G. Chang, A. M. Mier Valdivia, C.-K. Chan, Q. D. Gibson, J. Zhou, Z. Liu, K. Watanabe, T. Taniguchi, H. Lin, R. J. Cava, L. Fu, N. Gedik, and P. Jarillo-Herrero, *Nat. Phys.* **14**, 900–906 (2018).
- [46] J.-X. Hu, C.-P. Zhang, Y.-M. Xie, and K. T. Law, arXiv:2004.14140.
- [47] C.-P. Zhang, J. Xiao, B. T. Zhou, J.-X. Hu, Y.-M. Xie, B. Yan, and K. T. Law, arXiv:2010.08333.
- [48] D.-F. Shao, S.-H. Zhang, G. Gurung, W. Yang, and E. Y. Tsympal, *Phys. Rev. Lett.* **124**, 067203 (2020).
- [49] C. Zeng, S. Nandy, A. Taraphder, and S. Tewari, *Phys. Rev. B* **100**, 245102(2019).
- [50] X.-Q. Yu, Z.-G. Zhu, J.-S. You, T. Low, and G. Su, *Phys. Rev. B* **99**, 201410(R) (2019).
- [51] C. Zeng, S. Nandy, and S. Tewari, *Phys. Rev. Research* **2**, 032066(R) (2020).
- [52] Z. Z. Du, H.-Z. Lu, and X. C. Xie, arXiv:2105.10940.
- [53] Z. Z. Du, C. M. Wang, H.-P. Sun, H.-Z. Lu, and X. C. Xie, *Nat. Commun.* **12**, 5038 (2021).
- [54] Q. Ma, S.-Y. Xu, H. Shen, D. MacNeill, V. Fatemi, T.-R. Chang, A. M. Mier Valdivia, S. Wu, Z. Du, C.-H. Hsu, S. Fang, Q. D. Gibson, K. Watanabe, T. Taniguchi, R. J. Cava, E. Kaxiras, H.-Z. Lu, H. Lin, L. Fu, N. Gedik, and P. Jarillo-Herrero, *Nature* **565**, 337–342 (2019).
- [55] K. Kang, T. Li, E. Sohn, J. Shan, and K. F. Mak, *Nat. Mater.* **18**, 324–328 (2019).

- [56] A. P. Schnyder, S. Ryu, A. Furusaki, and A. W. W. Ludwig, *Phys. Rev. B* **78**, 195125 (2008).
- [57] A. Kitaev, in *Advances in Theoretical Physics: Landau Memorial Conference*, edited by V. Lebedev and M. Feigel'man, AIP Conf. Proc. Vol. 1134 (AIP, Melville, NY, 2009), p. 22.
- [58] S. Ryu, A. P. Schnyder, A. Furusaki, and A. W. W. Ludwig, *New J. Phys.* **12**, 065010 (2010).
- [59] C.-K. Chiu, H. Yao, and S. Ryu, *Phys. Rev. B* **88**, 075142 (2013).
- [60] T. Morimoto and A. Furusaki, *Phys. Rev. B* **88**, 125129 (2013).
- [61] C. Fang, M. J. Gilbert, and B. A. Bernevig, *Phys. Rev. B* **86**, 115112 (2012).
- [62] A. Alexandradinata, C. Fang, M. J. Gilbert, and B. A. Bernevig, *Phys. Rev. Lett.* **113**, 116403 (2014).
- [63] K. Shiozaki and M. Sato, *Phys. Rev. B* **90**, 165114 (2014).
- [64] C.-X. Liu, R.-X. Zhang, and B. K. VanLeeuwen, *Phys. Rev. B* **90**, 085304 (2014).
- [65] C. Fang and L. Fu, *Phys. Rev. B* **91**, 161105 (2015).
- [66] K. Shiozaki, M. Sato, and K. Gomi, *Phys. Rev. B* **91**, 155120 (2015).
- [67] K. Shiozaki, M. Sato, and K. Gomi, *Phys. Rev. B* **93**, 195413 (2016).
- [68] Z. Wang, A. Alexandradinata, R. J. Cava, and B. A. Bernevig, *Nature* **532**, 189 (2016).
- [69] K. Shiozaki, M. Sato, and K. Gomi, *Phys. Rev. B* **95**, 235425 (2017).
- [70] J. Kruthoff, J. de Boer, J. van Wezel, C. L. Kane, and R.-J. Slager, *Phys. Rev. X* **7**, 041069 (2017).
- [71] H. C. Po, A. Vishwanath, and H. Watanabe, *Nat. Commun.* **8**, 50 (2017).
- [72] B. Bradlyn, L. Elcoro, J. Cano, M. G. Vergniory, Z. Wang, C. Felser, M. I. Aroyo, and B. A. Bernevig, *Nature* **547**, 298 (2017).
- [73] H. Watanabe, H. C. Po, and A. Vishwanath, *Sci. Adv.* **4**, eaat8685 (2018).
- [74] T. Fukui, T. Fujiwara, and Y. Hatsugai, *J. Phys. Soc. Jpn.* **77**, 123705. (2008).
- [75] Z. Wang, X. L. Qi, and S. C. Zhang, *New J. Phys.* **12**, 065007 (2010).
- [76] T. A. Loring and M. B. Hastings, *EPL* **92**, 67004 (2010).

- [77] I. C. Fulga, F. Hassler, and A. R. Akhmerov, Phys. Rev. B **85**, 165409 (2012).
- [78] B. Sbierski and P. W. Brouwer, Phys. Rev. B **89**, 155311 (2014).
- [79] T. A. Loring, Ann. Phys. **356**, 383 (2015).
- [80] H. Katsura and T. Koma, J. Math. Phys. **57**, 021903 (2016).
- [81] Y. Akagi, H. Katsura, and T. Koma, J. Phys. Soc. Jpn. **86**, 123710 (2017).
- [82] H. Katsura and T. Koma, J. Math. Phys. **59**, 031903 (2018).
- [83] L. Fu and C. L. Kane, Phys. Rev. B **76**, 045302 (2007).
- [84] S. Maekawa, S. O. Valenzuela, E. Saitoh, and T. Kimura, *Spin Current*, (Oxford Univ. Press, 2012).
- [85] S. Murakami, New. J. Phys. **9**, 356 (2007).
- [86] V. M. Edelstein, Solid State Commun. **73**, 233 (1990).
- [87] Y. Sun, H. Chang, M. Kabatek, Y.-Y. Song, Z. Wang, M. Jantz, W. Schneider, M. Wu, E. Montoya, B. Kardasz, B. Heinrich, S. G. E. te Velthuis, H. Schultheiss, and A. Hoffmann, Phys. Rev. Lett. **111**, 106601 (2013).
- [88] H. Yu, O. Kelly, V. Cros, R. Bernard, P. Bortolotti, A. Anane, F. Brandl, R. Huber, I. Stasinopoulos, and D. Grundler, Sci. Rep. **4** 6848 (2014) .
- [89] T. Schneider, A. A. Serga, T. Neumann, B. Hillebrands, and M. P. Kostylev Phys. Rev. B **77**, 214411 (2008).
- [90] J. R. Eshbach, Phys. Rev. Lett. **8**, 357 (1962).
- [91] V. V. Kruglyak, S. O. Demokritov, D. Grundler, Journal of Physics D, **43**, 264001 (2010).
- [92] A. A. Serga, A. V. Chumak, and B. Hillebrands, Journal of Physics D, **43**, 264002 (2010).
- [93] M. P. Kostylev, Appl. Phys. Lett. **87**, 153501 (2005).
- [94] T. Schneider, Appl. Phys. Lett. **92**, 022505 (2008).
- [95] K.S. Lee, J. Appl. Phys. **104**, 053909 (2008).
- [96] A. V. Chumak, Nat. Commun. **5**, 4700 (2007).
- [97] S. Fujimoto, Phys. Rev. Lett. **103**, 047203 (2009).
- [98] H. Katsura, N. Nagaosa, and P. A. Lee, Phys. Rev. Lett. **104**, 066403 (2010).

- [99] Y. Onose, T. Ideue, H. Katsura, Y. Shiomi, N. Nagaosa, and Y. Tokura, *Science* **329**, 297 (2010).
- [100] T. Ideue, Y. Onose, H. Katsura, Y. Shiomi, S. Ishiwata, N. Nagaosa, and Y. Tokura, *Phys. Rev. B* **85**, 134411 (2012).
- [101] R. Matsumoto and S. Murakami, *Phys. Rev. B* **84**, 184406 (2011).
- [102] R. Matsumoto and S. Murakami, *Phys. Rev. Lett.* **106**, 197202 (2011).
- [103] R. Matsumoto, R. Shindou, and S. Murakami, *Phys. Rev. B* **89**, 054420 (2014).
- [104] M. Kawano and C. Hotta, *Phys. Rev. B* **99**, 054422 (2019).
- [105] S. K. Kim, K. Nakata, D. Loss, and Y. Tserkovnyak, *Phys. Rev. Lett.* **122**, 057204 (2019).
- [106] S. A. Owerre, *J. Phys. Condens. Matter* **28**, 386001 (2016).
- [107] S. A. Owerre, *J. Appl. Phys.* **120**, 043903 (2016).
- [108] H. Lee, J. H. Han, and P. A. Lee, *Phys. Rev. B* **91**, 125413 (2015).
- [109] B. Xu, T. Ohtsuki, and R. Shindou, *Phys. Rev. B* **94**, 220403(R) (2016).
- [110] A. Mook, J. Henk, and I. Mertig, *Phys. Rev. B* **90**, 024412 (2014).
- [111] R. Seshadri and D. Sen, *Phys. Rev. B* **97**, 134411 (2018).
- [112] R. Chisnell, J. S. Helton, D. E. Freedman, D. K. Singh, R. I. Bewley, D. G. Nocera, and Y. S. Lee, *Phys. Rev. Lett.* **115**, 147201 (2015).
- [113] M. Hirschberger, Robin Chisnell, Young S. Lee, and N. P. Ong, *Phys. Rev. Lett.* **115**, 106603 (2015).
- [114] P. A. McClarty, X.-Y. Dong, M. Gohlke, J. G. Rau, F. Pollmann, R. Moessner, and K. Penc, *Phys. Rev. B* **98**, 060404(R) (2018).
- [115] D. G. Joshi, *Phys. Rev. B* **98**, 060405(R) (2018).
- [116] J. Cookmeyer and J. E. Moore, *Phys. Rev. B* **98**, 060412(R) (2018).
- [117] F. Lu, Y.-M. Lu, arXiv:1807.05232.
- [118] J. H. Han and H. Lee, *J. Phys. Soc. Jpn.* **86**, 011007 (2017).
- [119] S. Murakami and A. Okamoto, *J. Phys. Soc. Jpn.* **86**, 011010 (2017).
- [120] R. Cheng, S. Okamoto, and D. Xiao, *Phys. Rev. Lett.* **117**, 217202 (2016).

- [121] V. A. Zyuzin and A. A. Kovalev, *Phys. Rev. Lett.* **117**, 217203 (2016).
- [122] A. Mook, B. Göbel, J. Henk, and I. Mertig, *Phys. Rev. B* **97**, 140401(R) (2018).
- [123] K. Nakata, J. Klinovaja, and D. Loss, *Phys. Rev. B* **95**, 125429 (2017).
- [124] Y. Shiomi, R. Takashima, and E. Saitoh, *Phys. Rev. B* **96**, 134425 (2017).
- [125] A. Mook, J. Henk, and I. Mertig, *Phys. Rev. Lett.* **117**, 157204 (2016).
- [126] F.-Y. Li, Y.-D. Li, Y.-B. Kim, L. Balents, Y. Yu, and G. Chen, *Nat. Commun.* **7**, 12691 (2016).
- [127] Y. Su, X. S. Wang, and X. R. Wang, *Phys. Rev. B* **95**, 224403 (2017).
- [128] S. A. Owerre, *Phys. Rev. B* **97**, 094412 (2018).
- [129] T. Liu and Z. Shi, *Phys. Rev. B* **99**, 214413 (2019).
- [130] J. Fransson, A. M. Black-Schaffer, and A. V. Balatsky, *Phys. Rev. B* **94**, 075401 (2016).
- [131] S. A. Owerre, *J. Phys. Commun.* **1**, 025007 (2017).
- [132] S. S. Pershoguba, S. Banerjee, J. C. Lashley, J. Park, H. Agren, G. Äeppli, and A. V. Balatsky, *Phys. Rev. X* **8**, 011010 (2018).
- [133] K. Li, C. Li, J. Hu, Y. Li, and C. Fang, *Phys. Rev. Lett.* **119**, 247202 (2017).
- [134] S. Bao, J. Wang, W. Wang, Z. Cai, S. Li, Z. Ma, D. Wang, K. Ran, Z.-Y. Dong, D. L. Abernathy, S.-L. Yu, X. Wan, J.-X. Li, and J. Wen, *Nat. Commun.* **9**, 2591 (2018).
- [135] I. E. Dzyaloshinskii, *Sov. Phys.—JETP.* **10**, 628 (1960).
- [136] T. Moriya, *Phys. Rev. Lett.* **4**, 228 (1960).
- [137] T. Moriya, *Phys. Rev.* **120**, 91 (1960).
- [138] R. Shindou, J. I. Ohe, R. Matsumoto, S. Murakami, and E. Saitoh, *Phys. Rev. B* **87**, 174402 (2013).
- [139] R. Shindou, R. Matsumoto, S. Murakami, and J. I. Ohe, *Phys. Rev. B* **87**, 174427 (2013).
- [140] S. K. Kim, H. Ochoa, R. Zarzuela, and Y. Tserkovnyak, *Phys. Rev. Lett.* **117**, 227201 (2016).
- [141] L. Zhang, J. Ren, J.-S. Wang, and B. Li, *Phys. Rev. B* **87**, 144101 (2013).

- [142] H. Kondo, Y. Akagi, and H. Katsura, *Phys. Rev. B* **99**, 041110(R) (2019).
- [143] A. V. Chumak, V. I. Vasyuchka, and A. A. Serga, *Nat. Phys.* **11**, 453 (2015).
- [144] H. Kondo, Y. Akagi, and H. Katsura, *Phys. Rev. B* **100**, 144401 (2019).
- [145] H. Kondo and Y. Akagi, *Phys. Rev. Lett.* **127**, 177201 (2021).
- [146] M. A. McGuire, H. Dixit, V. R. Cooper, and B. C. Sales, *Chemistry of Materials* **27**, 612-620 (2015).
- [147] B. Huang, G. Clark, E. Navarro-Moratalla, D. R. Klein, R. Cheng, K. L. Seyler, D. Zhong, E. Schmidgall, M. A. McGuire, D. H. Cobden, W. Yao, D. Xiao, P. Jarillo-Herrero, and X. Xu, *Nature* **546**, 270–273(2017).
- [148] B. Huang, G. Clark, D. R. Klein, D. MacNeill, E. Navarro-Moratalla, K. L. Seyler, N. Wilson, M. A. McGuire, D. H. Cobden, D. Xiao, W. Yao, P. Jarillo-Herrero, and X. Xu, *Nat. Nanotech.* **13**, 544–548 (2018).
- [149] L. Chen, J-H. Chung, B. Gao, T. Chen, M. B. Stone, A. I. Kolesnikov, Q. Huang, and P. Dai, *Phys. Rev. X* **8**, 041028 (2018).
- [150] N. Sivadas, S. Okamoto, X. Xu, C. J. Fennie, and D. Xiao, *Nano Lett.* **18**, 7658 (2018).
- [151] D. Soriano, C. Cardoso, and J. Fernandez-Rossier, *Solid State Commun.* **299**, 113662 (2019).
- [152] N. Ubrig, Z. Wang, J. Teyssier, T. Taniguchi, K. Watanabe, E. Giannini, A. F. Morpurgo, and M. Gibertini, *2D Materials* **7**, 015007 (2019).
- [153] A. T. Costa, D. L. R. Santos, N. M. R. Peres, and J. Fernández-Rossier, *2D Mater.* **7**, 045031 (2020).
- [154] D. Soriano, M. I. Katsnelson, and J. Fernández-Rossier, *Nano Lett.* **20**, 6225 (2020).
- [155] Y. O. Kvashnin, A. Bergman, A. I. Lichtenstein, and M. I. Katsnelson, *Phys. Rev. B* **102**, 115162 (2020).
- [156] R. Takashima, Y. Shiomi, and Y. Motome, *Phys. Rev. B* **98**, 020401(R) (2018).
- [157] I. Proskurin, A. S. Ovchinnikov, J. I. Kishine, and R. L. Stamps, *Phys. Rev. B* **98**, 134422 (2018).
- [158] H. Ishizuka and M. Sato, *Phys. Rev. B* **100**, 224411 (2019).
- [159] H. Kondo and Y. Akagi, arXiv:2109.09464.
- [160] M. Onoda, S. Murakami, and N. Nagaosa, *Phys. Rev. Lett.* **93**, 083901 (2004).

- [161] S. Raghu and F. D. M. Haldane, *Phys. Rev. A* **78**, 033834 (2008).
- [162] F. D. M. Haldane and S. Raghu, *Phys. Rev. Lett.* **100**, 013904 (2008).
- [163] Z. Wang, Y. Chong, J. D. Joannopoulos, and M. Soljačić, *Nature*. **461**, 772 (2009).
- [164] P. Ben-Abdallah, *Phys. Rev. Lett.* **116**, 084301 (2016).
- [165] O. Hosten and P. Kwiat, *Science* **319**, 787 (2008).
- [166] L. Lu, L. Fu, J. D. Joannopoulos, and M. Soljačić, *Nat. Photonics* **7**, 294 (2013).
- [167] C. Strohm, G. L. J. A. Rikken, and P. Wyder, *Phys. Rev. Lett.* **95**, 155901 (2005).
- [168] L. Sheng, D. N. Sheng, and C. S. Ting, *Phys. Rev. Lett.* **96**, 155901 (2006).
- [169] Y. Kagan and L. A. Maksimov, *Phys. Rev. Lett.* **100**, 145902 (2008).
- [170] A. V. Inyushkin and A. N. Taldenkov, *JETP Lett.* **86**, 379 (2007).
- [171] K. Sugii, M. Shimosawa, D. Watanabe, Y. Suzuki, M. Halim, M. Kimata, Y. Matsumoto, S. Nakatsuji, and M. Yamashita, *Phys. Rev. Lett.* **118**, 145902 (2017).
- [172] J. -S. Wang and L. Zhang, *Phys. Rev. B* **80**, 012301 (2009).
- [173] L. Zhang, J. Ren, J. -S. Wang, and B. Li, *Phys. Rev. Lett.* **105**, 225901 (2010).
- [174] T. Qin, J. Zhou, and J. Shi, *Phys. Rev. B* **86**, 104305 (2012).
- [175] M. Mori, A. Spencer-Smith, O. P. Sushkov, and S. Maekawa, *Phys. Rev. Lett.* **113**, 265901 (2014).
- [176] R. Süsstrunk and S. D. Huber, *Proc. Natl. Acad. Sci. U.S.A.* **113**, E4767 (2016).
- [177] R. Süsstrunk and S. D. Huber, *Science* **349**, 47 (2015).
- [178] O. Stenull, C. L. Kane, and T. C. Lubensky *Phys. Rev. Lett.* **117**, 068001 (2016).
- [179] M. Mori, A. Spencer-Smith, O. P. Sushkov, and S. Maekawa, *Phys. Rev. Lett.* **113**, 265901 (2014).
- [180] J. Rumhányi, K. Penc, and R. Ganesh, *Nat. Commun.* **6**, 6805 (2015).
- [181] D. G. Joshi and A. P. Schnyder, *Phys. Rev. B* **96**, 220405(R) (2017).
- [182] D. G. Joshi and A. P. Schnyder, *Phys. Rev. B* **100**, 020407(R) (2019).
- [183] K. Nawa, K. Tanaka, N. Kurita, T. J. Sato, H. Sugiyama, H. Uekusa, S. Ohira-Kawamura, K. Nakajima and H. Tanaka. *Nat. Commun.* **10**, 2096 (2019).

- [184] P. A. McClarty, F. Krüger, T. Guidi, S. F. Parker, K. Refson, A. W. Parker, D. Prabhakaran, and R. Coldea, *Nat. Phys.* **13**, 736 (2017).
- [185] T. Holstein and H. Primakoff, *Phys.Rev.* **58**, 1098 (1940).
- [186] J. H. P. Colpa, *Physica A* **93**, 327 (1978).
- [187] V. Gurarie and J. T. Chalker, *Phys. Rev. B* **68**, 134207 (2003).
- [188] H. Kondo, Y. Akagi, and H. Katsura, *Prog. Theor. Exp. Phys.* **2020**, 12A104 (2020).
- [189] N. Okuma, *Phys. Rev. Lett.* **119**, 107205 (2017).
- [190] M. Kawano, Y. Onose, and C. Hotta, *Commun. Phys.* **2**, 27 (2019).
- [191] M. Kawano and C. Hotta, *Phys. Rev. B* **100**, 174402 (2019).
- [192] Y. Aharonov and A. Casher, *Phys. Rev. Lett.* **53**, 319 (1984).
- [193] I. Paul and G. Kotliar, *Phys. Rev. B* **67**, 115131 (2003).
- [194] T. Liu and G. Vignale, *Phys. Rev. Lett.* **106**, 247203 (2011).
- [195] H. Katsura, N. Nagaosa, and A. V. Balatsky, *Phys. Rev. Lett.* **95**, 057205 (2005).
- [196] X. Zhang, T. Liu, M. E. Flatté, and H. X. Tang, *Phys. Rev. Lett.* **113**, 037202 (2014).
- [197] A. Kitaev, *Ann. Phys.* **321**, 2 (2006).
- [198] F. Kreith, M. Bohn, and M. S. Bohn, *Principles of Heat Transfer*. United States: Cengage Learning (2012).
- [199] We can also consider a more general case, i.e.,  $T(x, y) = T_0 - x\nabla_x T - y\nabla_y T$ , where  $T_0$ ,  $\nabla_x T$ , and  $\nabla_y T$  are constant. In such a case, the component of the spin current in the direction perpendicular to  $\nabla\bar{T} \equiv (\nabla_x T, \nabla_y T)$  can be formulated in the same way as Eq. (5.12), while the longitudinal component which corresponds to the nonlinear spin Seebeck effect of magnons can be expressed in the same way as in Ref. [156]. We note that both components of the second-order response are proportional to  $|\nabla\bar{T}|^2 = (\nabla_x T)^2 + (\nabla_y T)^2$ , and there is no current component proportional to  $(\nabla_x T)(\nabla_y T)$ .
- [200] C. Cercignani, *The Boltzmann Equation and Its Applications*. Springer, New York (1988).
- [201] J. Callaway, *Quantum Theory of the Solid State*. Academic Press, London (1974).
- [202] G. D. Mahan, *Many-Particle Physics*, 3rd. Edition (2000).

- [203] A. R. Wildes, B. Roessli, B. Lebech, and K. W. Godfrey, *J. Phys.: Condens. Matter* **10** 6417 (1998).
- [204] D. Hirobe, M. Sato, T. Kawamata, Y. Shiomi, K. Uchida, R. Iguchi, Y. Koike, S. Maekawa, and E. Saitoh, *Nat. Phys.* **13**, 30 (2017).
- [205] C. I. Hiley, M. R. Lees, J. M. Fisher, D. Thompsett, S. Agrestini, R. I. Smith, and R. I. Walton, *Angew. Chem. Int. Ed.* **53**, 4423 (2014).
- [206] Y. S. Ponosov, E.V. Komleva, D.A. Zamyatin, R. I. Walton, and S.V. Streltsov, *Phys. Rev. B* **99**, 085103 (2019).
- [207] T. Okabe, H. Yamaguchi, S. Kittaka, T. Sakakibara, T. Ono, and Y. Hosokoshi, *Phys. Rev. B* **95**, 075120 (2017).
- [208] G. Sala, M. B. Stone, B. K. Rai, A. F. May, P. Laurell, V. O. Garlea, N. P. Butch, M. D. Lumsden, G. Ehlers, G. Pokharel, A. Podlesnyak, D. Mandrus, D. S. Parker, S. Okamoto, G. D. Halasz, and A. D. Christianson, *Nat. Commun.* **12**, 171 (2021).
- [209] I. Spremo, F. Schütz, P. Kopietz, V. Pashchenko, B. Wolf, M. Lang, J. W. Bats, C. Hu, and M. U. Schmidt, *Phys. Rev. B* **72**, 174429 (2005).
- [210] A. A. Tsirlin, O. Janson, and H. Rosner, *Phys. Rev. B* **82**, 144416 (2010).
- [211] M. Yehia, E. Vavilova, A. Möller, T. Taetz, U. Löw, R. Klingeler, V. Kataev, and B. Büchner, *Phys. Rev. B* **81**, 060414(R) (2010).
- [212] L. Lederová, A. Orendáčová, J. Chovan, J. Strečka, T. Verkholyak, R. Tarasenko, D. Legut, R. Sýkora, E. Čížmár, V. Tkáč, M. Orendáč, and A. Feher, *Phys. Rev. B* **95**, 054436 (2017).
- [213] L. Ge, J. Flynn, J. A. M. Paddison, M. B. Stone, S. Calder, M. A. Subramanian, A. P. Ramirez, and M. Mourigal, *Phys. Rev. B* **96**, 064413 (2017).
- [214] A. Krimmel, H. Mutka, M. M. Koza, V. Tsurkan, and A. Loidl, *Phys. Rev. B* **79**, 134406 (2009).
- [215] Y. Shimizu, A. Otsuka, M. Maesato, M Tsuchiizu, A Nakao, H Yamochi, T Hiramatsu, Y Yoshida, and G Saito, *Phys. Rev. B* **99**, 174417 (2019).
- [216] M. Naka, S. Hayami, H. Kusunose, Y. Yanagi, Y. Motome, and H. Seo, *Nat. Commun.* **10**, 4305 (2019).
- [217] M. Naka, S. Hayami, H. Kusunose, Y. Yanagi, Y. Motome, and H. Seo, *Phys. Rev. B* **102**, 075112 (2020).
- [218] F. Keffer, *Phys. Rev.* **126**, 896 (1962).